Supporting Information for

The Electronic Structures of an $[Fe(NNR_2)]^{+/0/-}$ Redox Series: Ligand Non-Innocence and Implications for Catalytic Nitrogen Fixation

Niklas B. Thompson[†], Paul H. Oyala[†], Hai T. Dong[‡], Matthew J. Chalkley[†], Jiyong Zhao[§], E. Ercan Alp[§], Michael Hu[§], Nicolai Lehnert*[‡], and Jonas C. Peters*[†]

[†]Division of Chemistry and Chemical Engineering, California Institute of Technology, Pasadena, California 91125, USA

[‡]Department of Chemistry and Department of Biophysics, University of Michigan, Ann Arbor, Michigan 48109-1055, USA

[§]Advanced Photon Source, Argonne National Laboratory, Argonne, Illinois 60429, USA

TABLE OF CONTENTS

S.1 Experimental Section

S.1.1 Additional Experimental Details

S.1.1.1 ^{57}Fe Mössbauer Spectroscopy

Magnetically-perturbed spectra collected on samples in $S = 1/2$ ground states were simulated using the following spin Hamiltonian,[1]

$$\hat{H}_{SH} = \beta_e \hat{S} \cdot \boldsymbol{g} \cdot \vec{B} + \hat{I} \cdot \boldsymbol{A} \cdot \hat{S} - g_N \beta_N \hat{I} \cdot \vec{B} + \hat{I} \cdot \boldsymbol{Q} \cdot \hat{I} \tag{S.1}$$

where β_e is the Bohr magneton, $\hat{S}$ is the electronic spin operator, $\boldsymbol{g}$ is the electronic g-tensor, $\vec{B}$ is the applied magnetic field, $\hat{I}$ is the nuclear spin operator, $\boldsymbol{A}$ is the hyperfine coupling tensor, g_N and β_N are the nuclear g-factor and magneton, and $\boldsymbol{Q}$ is the electric field gradient tensor. In the presence of even a weak external field, the electronic Zeeman interaction dominates this Hamiltonian, and the nuclear terms can be solved in a basis of the eigenstates of the electronic Zeeman operator.[1,2] In this case, the nuclear terms are separable for every such eigenstate, $|i\rangle$,

$$\hat{H}_{\mathrm{nuc},i} = \hat{I} \cdot \boldsymbol{A} \cdot \langle \hat{S} \rangle_i - g_N \beta_N \hat{I} \cdot \vec{B} + \hat{I} \cdot \boldsymbol{Q} \cdot \hat{I} \tag{S.2}$$

$$= -g_N \beta_N \hat{I} \cdot \left(\frac{-\boldsymbol{A} \langle \hat{S} \rangle_i}{g_N \beta_N} + \vec{B} \right) + \frac{eQV_{zz}}{4I(2I-1)} \left[3\hat{I}_z^2 - I(I+1) + \frac{\eta}{2}(\hat{I}_+^2 + \hat{I}_-^2) \right] \tag{S.3}$$

where eQV_{zz} is the nuclear quadrupole coupling constant, η is the asymmetry parameter, and $\hat{S}$ has been replaced by its expectation value for state $|i\rangle$. Conventionally, $\eta = \frac{V_{yy} - V_{xx}}{V_{zz}}$, where V_{kk} are the principle components of $\boldsymbol{Q}$ with $V_{zz} \geq V_{yy} \geq V_{xx}$. In the limit of slow electronic relaxation, separate Mössbauer spectra are computed for each state $|i\rangle$, and the experimental spectrum is reproduced as their Boltzmann-weighted sum. During simulation, the g-tensor was fixed as determined from EPR studies. All other parameters, including the relative areas of the (sub)spectra, were allowed to refine freely. Note that noise in the data and imperfections in the simulation may cause the total summed area to exceed or fail to reach unity. Also note that $\boldsymbol{A}$ in the model above is expressed in units of the "internal" field about the ^{57}Fe nucleus. This can be converted into the HFC tensor in units of MHz for the nuclear ground state of ^{57}Fe by application of,[1]

$$\boldsymbol{A}(\mathrm{MHZ}) = 1.38152 \times \boldsymbol{A}(\mathrm{T}) \tag{S.4}$$

S.1.1.2 EPR Spectroscopy

Pulse X- and Q-band electron spin-echo detected EPR (ESE-EPR) field-swept spectra were acquired using the 2-pulse "Hahn-echo" sequence ($\pi/2$–τ–π–τ–echo) where τ was held constant. Subsequently, each field swept echo-detected EPR absorption spectrum was modified using a pseudo-modulation function to approximate the effect of field modulation and produce the CW-like 1st derivative spectrum.[3] Spin-spin relaxation times (T_2) were measured at Q-band using the same "Hahn-echo" pulse sequence ($\pi/2$–τ–π–τ–echo) where τ was incremented to produce a time-domain spectrum of the decay of the spin-echo intensity as a function of time.

Pulse Q-band HYSCORE spectra were acquired using the 4-pulse sequence ($\pi/2$–τ–$\pi/2$–T_1–π–T_2–$\pi/2$–τ–echo), where τ is a fixed delay, and T_1 and T_2 are variable delays independently incremented by ΔT_1 and ΔT_2, respectively. The microwave power of the $\pi/2$ pulses were reduced such that the lengths of these pulses were equal to the π pulse to ensure that each pulse provided the same excitation bandwidth. Sixteen step phase cycling was utilized. The time domain spectra were baseline-corrected (third-order polynomial), apodized with a Hamming window function, zero-filled to eight-fold points, and fast Fourier-transformed to yield the frequency domain. Acquisition parameters for all spectra included the following: T = 15 K; microwave frequency = 34.096 GHz ([(P_3^B)Fe($NNMe_2$)]$^-$), 34.04 GHz ([(P_3^B)Fe($NNMe_2$)]$^+$) ; $\pi/2 = \pi = 24$ ns; $\tau = 100$ ns; $T_1 = T_2 = 100$ ns; $\Delta T_1 = \Delta T_2 = 16$ ns; srt = 1 ms.

Pulse X- and Q-band ENDOR spectra were acquired using the Davies pulse sequence (π–T_{RF}–π_{RF}–T_{RF}–$\pi/2$–τ–π–echo), where T_{RF} is the delay between MW pulses and RF pulses, π_{RF} is the length of the RF pulse. The RF frequency was randomly sampled during each pulse sequence.

In general, the ENDOR spectrum for a given nucleus with spin $I = 1/2$ (e.g., ^{1}H) coupled to the $S = 1/2$ electron spin exhibits a doublet at frequencies,

$$\nu_{\pm} = \left| \frac{A}{2} \pm \nu_N \right| \tag{S.5}$$

where ν_N is the nuclear Larmor frequency and A is the hyperfine coupling. For nuclei with $I \geq 1$ (e.g., ^{14}N), an additional splitting of the $\nu_{\pm}$ manifolds is produced by the nuclear quadrupole

interaction (P),

$$\nu_{\pm,m_I} = \left| \nu_N \pm \frac{3P(2m_I - 1)}{2} \right| \tag{S.6}$$

In HYSCORE spectra, these signals manifest as cross-peaks or ridges in the 2-D frequency spectrum which are generally symmetric about the diagonal of a given quadrant. This technique allows hyperfine levels corresponding to the same electron-nuclear submanifold to be differentiated, as well as separating features from hyperfine couplings in the weak-coupling regime ($|A| < 2|\nu_I|$) in the (+, +) quadrant from those in the strong coupling regime ($|A| > 2|\nu_I|$) in the (−, +) quadrant. The (−, −) and (+, −) quadrants of these frequency spectra are symmetric to the (+, +) and (−, +) quadrants, thus typically only two of the quadrants are typically displayed in literature. For systems with appreciable hyperfine anisotropy in frozen solutions or solids, HYSCORE spectra typically do not exhibit sharp cross peaks, but show ridges that represent the sum of cross peaks from selected orientations at the magnetic field position at which the spectrum is collected. The length and curvature of these correlation ridges allow for the separation and estimation of the magnitude of the isotropic and dipolar components of the hyperfine tensor.

For systems exhibiting significant rhombic symmetry in the hyperfine tensor, as is the case for the N_α for $[(P_3{}^B)Fe(NNMe_2)]^{+/-}$, such simple analysis of these correlation ridges is less facile, and even cursory analysis requires spectral simulations. For systems coupled to nuclei with $I = 1$, such as ^{14}N, the double-quantum peaks are often the most intense feature. These cross-peaks are defined by the following equations:

$$\nu_\alpha = \pm 2\sqrt{(\nu_I + A/2)^2 + K^2(3 + \eta^2)} \tag{S.7}$$

$$\nu_\beta = \pm 2\sqrt{(\nu_I - A/2)^2 + K^2(3 + \eta^2)} \tag{S.8}$$

where $K = e^2qQ/4\hbar$. For weakly coupled nuclei ($|A| < 2|\nu_I|$), ν_α and ν_β are both positive, appearing in the (+, +) quadrant, while for strongly coupled nuclei they will show up in the (−, +) quadrant. In the intermediate coupling regime where $|A| \approx |2\nu_I|$, peaks will often appear in both the (+, +) and (−, +) quadrants of the HYSCORE spectrum.

The HFC tensor, $\boldsymbol{A}$, can be decomposed into its isotropic, a_{iso}, and anisotropic, $\boldsymbol{T}$, parts,[4]

$$\boldsymbol{A} = a_{\mathrm{iso}}\mathbf{1} + \boldsymbol{T} \tag{S.9}$$

where the anisotropic HFC tensor, $\boldsymbol{T}$, is the traceless matrix formed by,

$$\boldsymbol{T} = \boldsymbol{A} - \frac{1}{3}\,\mathrm{Tr}\,\boldsymbol{A} \tag{S.10}$$

Thus, $a_{\mathrm{iso}} = \frac{1}{3}\,\mathrm{Tr}\,\boldsymbol{A}$. $\boldsymbol{T}$ can be further decomposed into scalar components: t (in units of energy), describing the magnitude of the anisotropic HFC coupling, and a dimensionless term δ_{HFC} ($0 \leq \delta_{\mathrm{HFC}} \leq 1$), describing the rhombicity of the tensor,

$$\boldsymbol{T} = \begin{pmatrix} 2t & & \\ & -t(1-\delta_{\mathrm{HFC}}) & \\ & & -t(1+\delta_{\mathrm{HFC}}) \end{pmatrix} \tag{S.11}$$

For an isotropic HFC tensor, $t = 0$. For an anisotropic, axially-symmetric tensor, $t \neq 0$ and $\delta_{\mathrm{HFC}} = 0$, while a rhombic tensor has $t \neq 0$ and $\delta_{\mathrm{HFC}} = 1$.

S.1.2 Additional Synthetic Details

S.1.2.1 Synthesis of $(P_3^B)Fe(^{15}N^{15}NMe_2)$

The synthesis of $(P_3^B)Fe(^{15}N^{15}NMe_2)$ followed the reported procedure,[5] but replacing the atmosphere of $^{14}N_2$ gas with $^{15}N_2$ gas.

S.1.2.2 Synthesis of $(P_3^B)Fe(NN(^{13}CH_3)_2)$

The synthesis of $(P_3^B)Fe(NN(^{13}CH_3)_2)$ followed the reported procedure,[5] but replacing MeOTf with $(^{13}CH_3)OTf$.

S.1.2.3 Synthesis of $(P_3^B)^{57}Fe(NNMe_2)$

The synthesis of $(P_3^B)^{57}Fe(NNMe_2)$ followed the reported procedure,[5] but replacing $(P_3^B)Fe(Br)$ as the iron precursor with $(P_3^B)^{57}Fe(Cl)$.

S.1.2.4 Synthesis of $(P_3^B)^{57}Fe(^{15}N^{15}NMe_2)$

The synthesis of $(P_3^B)^{57}Fe(^{15}N^{15}NMe_2)$ followed the reported procedure,[5] but replacing $(P_3^B)Fe(Br)$ as the iron precursor with $(P_3^B)^{57}Fe(Cl)$, and replacing the atmosphere of $^{14}N_2$ gas with $^{15}N_2$ gas.

S.1.2.5 Synthesis of $[(P_3^B)Fe(NNMe_2)][BAr^F{}_4]$ Isotopologues

The synthesis of isotopologues of $[(P_3^B)Fe(NNMe_2)][BAr^F{}_4]$ including ^{57}Fe, ^{15}N, and ^{13}C were prepared as described above, but using the corresponding isotopologue of $(P_3^B)Fe(NNMe_2)$ as the starting material.

S.1.2.6 Crystallization of $[K(benzo\text{-}15\text{-}c\text{-}5)_2][(P_3^B)Fe(NNMe_2)]$

To obtain a crystal of $[(P_3^B)Fe(NNMe_2)]^-$ suitable for X-ray diffraction, a 5 mM 2-MeTHF solution of $(P_3^B)Fe(NNMe_2)$ was reduced to $[(P_3^B)Fe(NNMe_2)]^-$ as described in the main text, and subsequently filtered into a vial containing 2.1 equiv of solid benzo-15-c-5. The resultant solution was layered with *n*-pentane chilled to −78 °C (2:1 *n*-pentane:2-MeTHF), and this mixture was

placed in a freezer at −35 °C. After ca. 24 hours, a crop of dark crystals formed on the bottom of the vial; this sample was transferred to the X-ray diffractometer on dry ice, where the crystals were quickly removed from their mother liquor and suspended in Paratone N oil. A suitable crystal was selected and mounted on the diffractometer, which was pre-chilled to 100 K under a stream of dry N_2. Under a microscope, the crystals begin to visually decompose as soon as they are removed from their chilled mother liquor, requiring this procedure to be performed in a matter of minutes; multiple attempts were required before a strongly diffracting crystal was obtained. To confirm that the coordination of benzo-15-c-5 to the K^+ counterion of $[(P_3{}^B)Fe(NNMe_2)]^-$ does not affect its spectroscopic properties, we repeated this experiment, but transferred the 2-MeTHF solution containing $[(P_3{}^B)Fe(NNMe_2)]^-$ to a pre-chilled quartz X-band sample tube, which was subsequently frozen and analyzed by CW EPR spectroscopy. The spectra of $[(P_3{}^B)Fe(NNMe_2)]^-$ prepared in this fashion with or without added benzo-15-c-5 are identical (Figure S.6).

S.1.2.7 Synthesis of $[(P_3{}^B)Fe(NNMe_2)]^-$ Isotopologues

The synthesis of isotopologues of $[(P_3{}^B)Fe(NNMe_2)]^-$ including ^{57}Fe, ^{15}N, and ^{13}C were prepared as described above, but using the corresponding isotopologue of $(P_3{}^B)Fe(NNMe_2)$ as the starting material.

S.1.3 Computational Methods

Most calculations were carried out using version 4.0.1.2 of the ORCA package.[6] Based on previous work,[5,7] DFT calculations utilized the TPSS family of meta-GGA exchange-correlation functionals, incorporating either 0% (TPSS),[8] 10% (TPSSh),[9] or 25% (TPSS0) Hartree-Fock exchange,[10,11] in combination with the zeroth order regular approximation (ZORA) to account for relativistic effects.[12] Gas-phase geometry optimizations were carried out using the TPSS functional in combination with the scalar relativistically recontracted versions of the def2-SVP (ZORA-def2-SVP) basis sets on C and H, and the scalar relativistically recontracted versions of the def2-TZVP (ZORA-def2-TZVP) basis sets on Fe, B, P, and N atoms and the C and H atoms of the "$NNMe_2$"

ligand.[13] For all atoms, the general-purpose segmented all-electron relativistically contracted auxiliary Coulomb-fitting basis (SARC/J) was employed, which is a decontraction of the def2/J basis developed by Weigend.[14] Optimizations were followed by a frequency calculation to ensure a true minimum. For the computation of valence electronic structures, single point calculations were carried out on these optimized geometries using the TPSSh or TPSS0 functional in combination with an enlarged basis set, ZORA-def2-TZVPP, on Fe, B, P and the "$NNMe_2$" ligand.[13] These calculations employed a fine integration grid (ORCA Grid5) during geometry optimization, as well as during the final single-point calculation (Grid6). Calculations employing the hybrid meta-GGA functionals TPSSh/TPSS0 were accelerated using the RIJCOSX approximation with a fine auxiliary integration grid (ORCA GridX5).[15]

Broken-symmetry (BS) DFT calculations employed the `FlipSpin` method implemented in ORCA. In this approach, a high-spin solution is converged self-consistently, the spins on a selected group of atoms are "flipped" by exchanging the α and β spin density matrix elements on these centers, and then a solution of the desired multiplicity is converged. The BS character of the resultant solution can be determined following the corresponding orbital transformation of the converged Kohn-Sham orbitals,[16] where pairs of spin-coupled orbitals have spatial overlap less than 1. The degree of orbital overlap can be interpreted as a measure of the strength of the magnetic coupling.[17] In all cases, however, the BS solutions obtained explicitly via this method could also be arrived at by simply performing spin-unrestricted DFT calculations on the state of interest.

For DFT calculations of ^{57}Fe hyperfine interactions, the TPSSh functional was used in combination with the def2-TZVP basis set on all C and H atoms not involving the $NNMe_2$ ligand,[18] the CP(PPP) basis for Fe,[19] and the IGLO-III basis for the B, P, and "$NNMe_2$" atoms.[20] Given the lack of recontracted versions of these latter bases, scalar relativistic effects were ignored. The general purpose def2/J Coulomb fitting basis was employed on atoms using the def2-TZVP basis,[14] while the AutoAux feature of ORCA was used to generate auxiliary bases for the other atoms on-the-fly;[21] all auxiliary bases were fully decontracted. To capture core polarization effects, the radial integration accuracy was increased around the Fe, B, P, and "$NNMe_2$" atoms (`IntAcc 7`).

The calculation of hyperfine interactions employed the `eprnmr` module of ORCA. Calculation of the spin-orbit coupling (SOC) contribution to the Fe HFC constant used the `SOMF(1X)` mean-field SOC operator,[22] which is employed in a coupled-perturbed Kohn-Sham framework.[23,24] A previously-reported calibration was used to convert the computed Fe core electron density to the isomer shift (δ) in units of mm s^{-1}; estimates of the uncertainty in the computed values of δ and ΔE_Q were obtained from this calibration.[5]

DFT calculation of the EPR properties of free *N*,*N*-dimethylhydrazyl radicals used the same methods for geometry optimization described above. To calculate EPR properties, single point calculations were performed on these optimized geometries using the TPSSh functional in combination with the IGLO-III basis set, using the same methods described above for the calculation of ^{57}Fe hyperfine interactions. As shown in Table S.12, this method was found to almost quantitatively reproduce the experimental spectra of the known radicals $[HNNMe_2]^\bullet$ and $[H_2NNMe_2]^{\bullet+}$.[25–27] When calculating the EPR properties of $[NNMe_2]^{\bullet-}$, we considered both the ground-state geometry as well as a theoretical planar geometry more closely matching that of the "$NNMe_2$" ligands of $[(P_3{}^B)Fe(NNMe_2)]^{+/0/-}$ observed crystallographically. The planar structure was obtained using a constrained geometry optimization under approximate C_{2v} symmetry.

Multireference calculations employed the scalar relativistically recontracted versions of Dunning's correlation-consistent basis sets tailored for use with the Douglas-Kroll-Hess (DKH) Hamiltonian to account for relativistic effects. The basis sets were of double-ζ quality on the C and H atoms (cc-pVDZ-DK),[28] and triple-ζ quality on the Fe, B, P, and "$NNMe_2$" atoms, the latter being augmented with additional diffuse functions for greater flexibility (aug-cc-pVTZ-DK).[29] In all calculations, the second order DKH Hamiltonian (DKH2) was used.[30] To accelerate these calculations, the RIJK approximation was used in combination with the aug-cc-pVTZ/JK auxiliary Coulomb/exchange fitting basis for the C, H, B, P, and N atoms;[31] the AutoAux feature was used to generate an auxiliary basis set for Fe,[21] and all auxiliary bases were decontracted. Input orbitals were taken from the quasi-restricted orbitals[32] of a DFT calculation employing the BP86 exchange-correlation functional.[33,34] The active space was chosen following the "standard" rules

for transition metal compounds:[35] for each complex, 10 orbitals were included, corresponding to the 5 Fe 3d orbitals, the π_N and π^*_{NN} orbitals of the "$NNMe_2$" fragment, the B $2p_z$ orbital, and 2 second-shell 3d' orbitals to provide greater flexibility for the strongly-occupied $3d_{xy}/3d_{x^2-y^2}$ orbitals. Using the standard notation CAS(*# electrons, # orbitals*), this leads to a CAS(9,10) active space for $[(P_3{}^B)Fe(NNMe_2)]^+$, a CAS(10,10) active space for $(P_3{}^B)Fe(NNMe_2)$, and a CAS(11,10) active space for $[(P_3{}^B)Fe(NNMe_2)]^-$.

State-averaged CASSCF calculations employed equal weights for all roots. After convergence of the CASSCF reference was achieved, a second-order N-electron perturbation theory (NEVPT2) calculation was performed to account for dynamic correlation effects.[36] For efficiency, NEVPT2 calculations employed the strongly-contracted variant of NEVPT2 parameterized in ORCA (SC-NEVPT2).[37] The calculation of g-tensors and the anisotropic parts of the HFC tensors was performed using the multireference CI (`mrci`) module. CAS-CI calculations were performed using a converged SA-CASSCF reference. The MRCI module computes g-tensors and HFC tensors using a sum-over-states formalism, as described elsewhere.[38] In all cases, the first 10 roots of the same multiplicity as the ground state were considered in these calculations. Localization of the active space orbitals used the algorithm of Foster and Boys.[39] For simplicity, hereafter we will use the notation ${}^{2S+1}\Gamma_{n,m}$ to refer to electronic states of the $[(P_3{}^B)Fe(NNMe_2)]^{+/0/-}$ redox series, where n refers to the overall charge, and m refers to the energetic ordering of the state, with $m = 0$ corresponding to the ground state of the spin manifold S.

Since our QCC-NCA analysis software is written specifically for Gaussian 09,[40] a reoptimization of the ground-state geometries of $[(P_3{}^B)Fe(NNMe_2)]^{+/0/-}$ was necessary for simulation of NRVS data. Using the optimized structures from ORCA, reoptimization of these molecules was carried out using the TPSS functional with a combination of def2-TZVP (on all non C, H atoms and the complete "$NNMe_2$" units) and def2-SVP (on the remaining C, H atoms) basis sets. The structures obtained in this way are essentially identical to those calculated with ORCA. The subsequent frequency calculations show no imaginary frequencies, indicating that true energy minima were obtained. The force constants were transformed to internal coordinates and extracted using a

modified version of the program Redong,[41] and modified NCA programs[42] based on QCPE 576[43] were used for the subsequent fitting of the experimental data. The data were fitted by adjusting a minimal set of force constants (in the spirit of the QCC-NCA approach) to reproduce the vibrations of the Fe–$NNMe_2$ units in the $[(P_3{}^B)Fe(NNMe_2)]^{+/0/-}$ complexes (see main text).

S.2 XRD Refinement Details

S.2.1 Refinement details for $[(P_3{}^B)Fe(NNMe_2)][BAr^F{}_4]$

The crystal structure of $[(P_3{}^B)Fe(NNMe_2)][BAr^F{}_4]$ suffers from positional disorder of one $-CF_3$ substituent of the $[BAr^F{}_4]^-$ counterion due to rotation, resulting in prolate thermal ellipsoid for one F atom. Attempts to model this positional disorder did not significantly improve the refinement.

S.2.2 Refinement details for [K(benzo-15-c-5][$(P_3{}^B)Fe(NNMe_2)$]

Over prolonged data collection, the crystal of [K(benzo-15-c-5][$(P_3{}^B)Fe(NNMe_2)$] appeared to suffer some decomposition, as R_{int} began to diverge for later runs. This resulted in a lack of complete high-angle data (dataset 91% complete to $\theta = 61.165°$), and a number of disagreeable reflections. Omitting the disagreeable reflections did not significantly affect refinement, and they were thus included in the final model. There was no indication of twinning, merohedral or otherwise (e.g., using the `TwinRotMat` subroutine of PLATON[44]).

During refinement, these issues appear to be manifest only in the presence of four disordered co-crystallized solvent molecules (2-MeTHF). Two of these solvent molecules suffer from two-part positional disorder; each part was located in the difference map and refined anisotropically. The remaining two solvent molecules are also disordered (as judged by the size of their thermal ellipsoids), but a clear multi-part positional disorder could not be identified. During refinement, the bond distances/angles of these disordered solvent molecules were constrained to be similar using SAME/SADI restraints, and a rigid-bond restraint (DELU) was applied individually to each. Despite these disordered solvent molecules, both $[(P_3{}^B)Fe(NNMe_2)]^-$ and its counterion refined without issue. The presence of the solvent molecules lowers the average C–C bond precision to 0.02 Å, which can be alleviated by using the `SQUEEZE` procedure implemented in PLATON to

remove the electron density associated with these molecules; however, as this does not significantly alter the ESDs of the atoms of interest, we report the complete dataset, solvent molecules included.

S.3 Estimation of $a_{iso}(^1H)$ for triplet $(P_3{}^B)Fe(NNMe_2)$ from VT NMR Data

For an orbitally-nondegenerate electronic state where the isotropic paramagnetic NMR shift is dominated by the Fermi contact term, the Bloembergen-McConnell formula gives,[45–47]

$$\delta_{\text{iso}}(\text{ppm}) = 10^6 \cdot \frac{g_{\text{iso}}\beta_e S(S+1)}{3g_N\beta_N k_B T} \cdot a_{\text{iso}}(\text{J}) \tag{S.12}$$

where g_{iso} is the isotropic electronic g-factor, k_B is the Boltzmann constant, and a_{iso}(J) is the isotropic hyperfine coupling constant, in J. Noting that $a_{\text{iso}}(\text{J}) = 10^6 \cdot h a_{\text{iso}}(\text{MHz})$, we have,

$$\delta_{\text{iso}}(\text{ppm}) = \frac{C}{T} \tag{S.13}$$

$$C = 10^{12} \cdot \frac{h g_{\text{iso}}\beta_e S(S+1)}{3g_N\beta_N k_B T} \cdot a_{\text{iso}}(\text{MHz}) \tag{S.14}$$

In other words, the isotropic hyperfine coupling constant (in MHz) can be estimated from the apparent Curie factor (C) using,

$$a_{\text{iso}}(\text{MHz}) = 10^{-12} \cdot \frac{3C g_N\beta_N k_B}{h g_{\text{iso}}\beta_e S(S+1)} \tag{S.15}$$

$$\approx 10^{-12} \cdot \frac{3C g_N\beta_N k_B}{h g_e\beta_e S(S+1)} \tag{S.16}$$

where the approximation $g_{\text{iso}} \approx g_e$ is justified given the initial assumption that the Fermi contact term dominates the paramagnetic shift. Using the previously-published value for the Curie factor for the N-CH_3 protons of $(P_3{}^B)Fe(NNMe_2)$ (-1.27×10^6 K^{-1}),[5] one would thus estimate $a_{\text{iso}} \approx -120$ MHz. However, we note that the previous simulation of the VT NMR data of $(P_3{}^B)Fe(NNMe_2)$ produced a Curie constant for these protons with relatively high uncertainty. An examination of the data revealed that this is due to the small absolute entropic contribution to the energy difference between the ground and excited states. Performing a global, simultaneous, least-squares fit of each ^{1}H nucleus to the magnetization function described in our previous work,[5] but approximating $\Delta G \approx \Delta H \approx \Delta E$, produces fits with much smaller relative errors (See Figure S.35 and Table S.3). Using the above definition of the Curie factor, we estimate $a_{\text{iso}} \approx -48 \pm 1$ MHz. We note that this

value is much larger than that measured for known *N,N*-dimethylhydrazyl radicals (Table S.12), likely reflecting the fact that ignoring the pseudocontact contribution to the isotropic shift is a poor approximation. This is consistent with the significant ligand-centered spin density calculated for the triplet excited state of $(P_3{}^B)Fe(NNMe_2)$.

S.4 Excited State Energetics of $[(P_3{}^B)Fe(NNMe_2)]^+$ from VT Magnetic Susceptibility

In order to determine if $[(P_3{}^B)Fe(NNMe_2)]^+$, like its reduced congener $(P_3{}^B)Fe(NNMe_2)$, possesses a low-lying excited state, we recorded its solution magnetic moment as a function of temperature (Figure S.2). Note that before calculating magnetic moments, the raw susceptibility data were corrected for the density changes of the solvent (d_8-THF); the correction used the known temperature dependence of density reported for THF,[48] and assumed a constant shift of 0.1 g mL^{-1} to account for the density difference of THF versus d_8-THF. Increasing the temperature from 183 to 323 K, we observed a concomitant increase in the observed magnetic moment of ca. 1 β_e, consistent with thermal population of a state with $S > 1/2$. To model this behavior, we assume that each pure paramagnetic state obeys a Curie law, so that $\chi_M = C/T$, and hence $\mu_{\text{eff}} = 2.828 \cdot (\chi_M T)^{1/2}$ is temperature-independent. Then we can write,[49]

$$\mu_{\text{obs}} = \mu_1 \cdot \gamma_1 + \mu_2 \cdot \gamma_2 \tag{S.17}$$

$$= \mu_1 \cdot (1 - \gamma_2) + \mu_2 \cdot \gamma_2 \tag{S.18}$$

$$= \mu_1 + (\mu_2 - \mu_1) \cdot \gamma_2 \tag{S.19}$$

$$= \mu_1 + (\mu_2 - \mu_1) \cdot \frac{g_2}{g_2 + g_1 \exp\left(\frac{1}{RT}(\Delta H - T\Delta S)\right)} \tag{S.20}$$

where μ_i is the magnetic moment of state i and g_i is the electronic degeneracy of state i. We have used this equation to fit the variable temperature magnetic data of $[(P_3{}^B)Fe(NNMe_2)]^+$ assuming $g_2 = 4$ and $\mu_2 = 3.87$ (i.e., a quartet excited state) and $g_2 = 6$ and $\mu_2 = 5.92$ (i.e., a sextet excited state). The final fits are of equal quality, and have final fitting parameters that are identical, within error, except for ΔS (Figure S.36 and Table S.4). Given the limited thermal stability over which magnetization data could be reliably collected, an unambiguous distinction between these

two models cannot be made experimentally. However, DFT calculations indicate that the sextet state state of $[(P_3{}^B)Fe(NNMe_2)]^+$ is significantly higher in energy than the quartet state (Tables S.10 and S.11), and on this basis we assign the excited state multiplicity as $S = 3/2$, and estimate the adiabatic doublet–quartet gap to be $\Delta H \approx 4.8 \pm 0.4$ kcal mol^{-1}.

S.5 Fitting of UV-vis Data

Using an idealized Gaussian line shape, an absorption band can be written,[50]

$$\epsilon(\bar{\nu}) = \epsilon_0 \exp\left(-\frac{4\log 2(\bar{\nu}-\bar{\nu}_0)^2}{\sigma_{1/2}^2}\right) \tag{S.21}$$

where ϵ_0 is the molar extinction coefficient at the absorption maximum, $\bar{\nu}_0$ is the energy at the absorption maximum, and $\sigma_{1/2}$ is the peak FWHM. The oscillator strength is given by,[50]

$$f = 4.33 \cdot 10^{-9} \int \epsilon(\bar{\nu}) d\bar{\nu} = 4.33 \cdot 10^{-9} \cdot \epsilon_0 \sigma_{1/2} \left(\frac{\pi}{4\log 2}\right)^{1/2} \tag{S.22}$$

and thus, we can express ϵ_0 in terms of f,

$$\epsilon(\bar{\nu}) = \frac{f}{4.33 \cdot 10^{-9}} \frac{2}{\sigma_{1/2}} \left(\frac{\log 2}{\pi}\right)^{1/2} \exp\left(-\frac{4\log 2(\bar{\nu}-\bar{\nu}_0)^2}{\sigma_{1/2}^2}\right) \tag{S.23}$$

Both experimental and ab initio electronic spectra were simulated using this expression. A minimum number of Gaussians to capture both the resolved features and the rising UV absorption edge were included in the experimental fits. Before fitting, low-temperature data were first corrected for the change in solvent density.[51]

S.6 Mössbauer simulation details

All magnetically-unperturbed components were fit assuming symmetric quadrupole doublets with Lorentzian line shapes. This is the correct model for homogeneous frozen solution spectra in the limit of fast electronic relaxation, which is typical at 80 K. However, spectra of $[(P_3{}^B)Fe(NNMe_2)][BAr^F{}_4]$ displayed a broad, asymmetric signal at 80 K, which sharpened considerably upon application of a 50 mT external magnetic field, indicating that this species is in the limit of slow electronic relaxation at these temperatures. The effects of this are also manifest in the observation of an EPR signature at room temperature (Figure S.4). This is apparently a result of unusually

slow spin-spin relaxation (T_2), as a Mössbauer spectrum collected on a polycrystalline sample of [(P_3^B)Fe(NNMe$_2$)][$BAr^F{}_4$] features an asymmetrically-broadened quadrupole doublet, indicating an intermediate relaxation regime. That these relaxation effects are dominated by a long T_2 was confirmed by direct measurement of the spin-spin relaxation times of [(P_3^B)Fe(NNMe$_2$)][$BAr^F{}_4$] and [(P_3^B)Fe(NAd)][$BAr^F{}_4$], demonstrating that the former has a significantly longer T_2 (Figure S.47 and Table S.8). While both of these complexes possess $S = 1/2$ ground states, the latter displays a symmetric quadrupole doublet in its solid state Mössbauer spectrum at 80 K.[52]

To simulate the spectrum of [(P_3^B)Fe(NNMe$_2$)][$BAr^F{}_4$], we employed the spin Hamiltonian described above to simultaneously fit dilute frozen solution spectra of ^{57}Fe-enriched [(P_3^B)Fe(NNMe$_2$)][$BAr^F{}_4$] with the external field oriented parallel and perpendicular to the applied γ-radiation. The g-tensor components were fixed from EPR spectroscopy, while δ and $|\Delta E_Q|$ were fixed initially based on the apparent values from the polycrystalline sample (note that the sign of ΔE_Q cannot be determined from these low-field simulations). Assuming that the EFG and HFC tensors were coincident with the electronic g-tensor, two equally-good solutions could be obtained that differed in the value of η and the relative orientation of the minor components of the HFC tensor (reduced $\chi^2 = 1.44$ and 1.32). These solutions could be rotated into one another by application of a ca. 90° Euler angle γ about g_{max} (= g_x, all rotations in the z–y–z convention) in either the EFG or HFC frame, indicating that the EFG/HFC tensors are not coincident with the g-tensor. Introduction of a single Euler angle β in the HFC frame produced the final solution to the data; we caution that without data collected at multiple field strengths, the final values of η and the orientation of the HFC frame are under-determined.

The magnetic field-dependence of the spectra of [(P_3^B)Fe(NNMe$_2$)]$^-$ indicate that this species is also in the limit of slow electronic relaxation in dilute frozen solution at 80 K. This behavior was expected based on the isoelectronic complexes (P_3^{Si})Fe(NNH$_2$) and (P_3^{Si})Fe(NNMe$_2$).[53] Indeed, the Mössbauer spectra reported for (P_3^{Si})Fe(NNR$_2$) are nearly identical with that of [(P_3^B)Fe(NNMe$_2$)]$^-$. To simulate the latter, we again employed the spin-Hamiltonian described above to simultaneously fit dilute frozen solution spectra with the external field oriented parallel and

perpendicular to the applied γ-radiation. Using the g-tensor components measured independently from EPR spectroscopy, and the reported parameters of $(P_3^{Si})Fe(NNMe_2)$ as an initial guess,[53] we obtained a unique spectral simulation (Figure S.32 and Table S.7). It was found that two additional quadrupole doublet impurities (totaling ca. 30% of the spectral area) were required to obtain a satisfactory simulation (reduced $\chi^2 = 0.77$), which is consistent with the typical purity reported for $(P_3^{Si})Fe(NNH_2)$ and $(P_3^{Si})Fe(NNMe_2)$.[53]

S.7 NMR Spectra

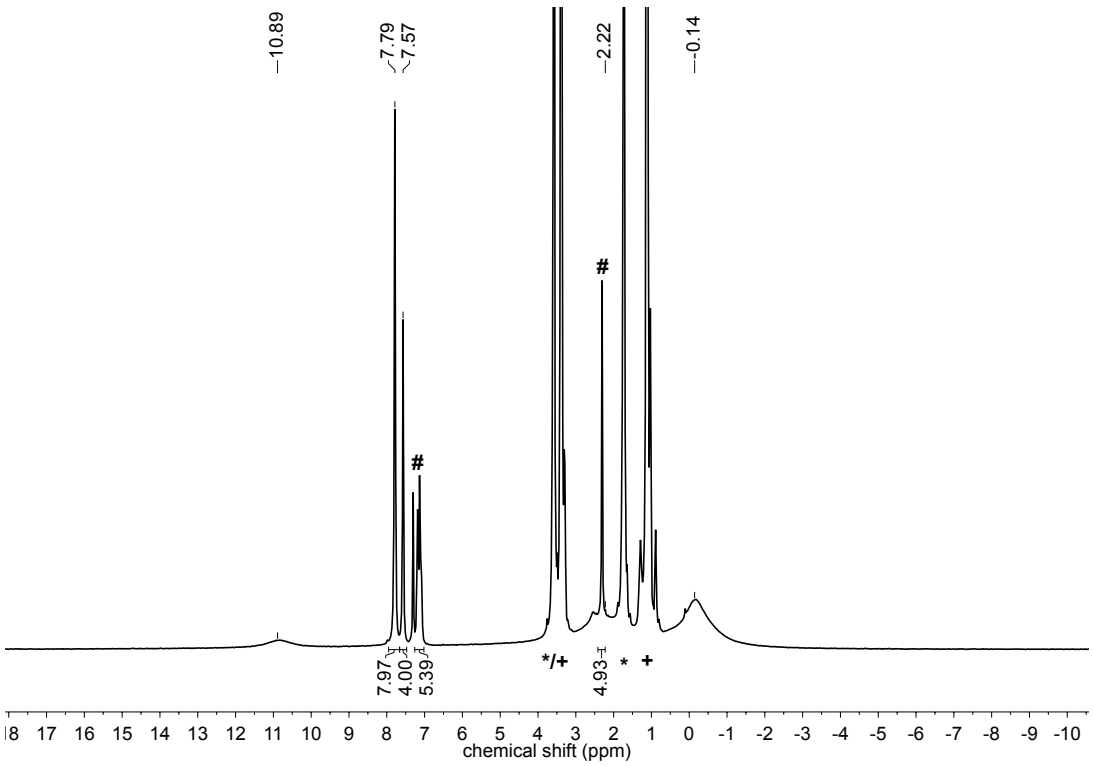

Figure S.1: ^{1}H NMR spectra of [(P_3^B)Fe(NNMe$_2$)][BAr^F_4] (500 MHz, d_8-THF, 293 K). $^{\#}$Denotes co-crystallized toluene. *Denotes signals from the lock solvent. $^{+}$Denotes signals from Et_2O added as a reference for the Evans method.

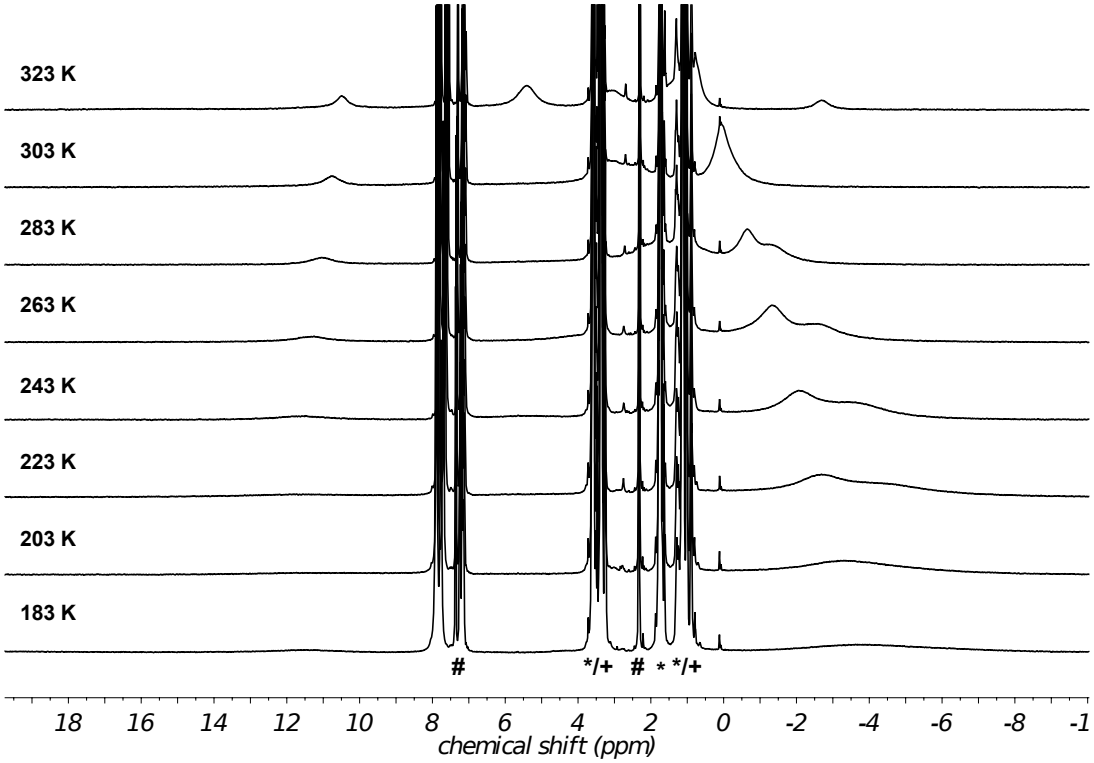

Figure S.2: Variable temperature ^{1}H NMR spectra of [(P_3^B)Fe(N$_2$Me$_2$)][BAr^F_4] (500 MHz, d_8-THF). $^{\#}$Denotes co-crystallized toluene. *Denotes signals from the lock solvent. $^{+}$Denotes signals from Et_2O added as a reference for the Evans method.

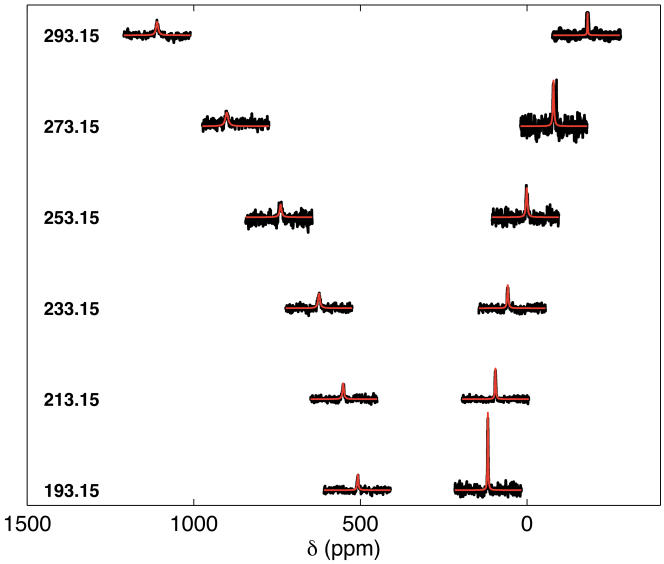

Figure S.3: Variable temperature ^{15}N NMR spectra of (P_3^B)Fe($^{15}N^{15}NMe_2$) (500 MHz, d_8-toluene). Temperatures (K) are shown to the left of each spectrum. The raw data are plotted in black, with least-squares fits to a Lorentzian peak shape are shown in red.

S.8 EPR Spectra

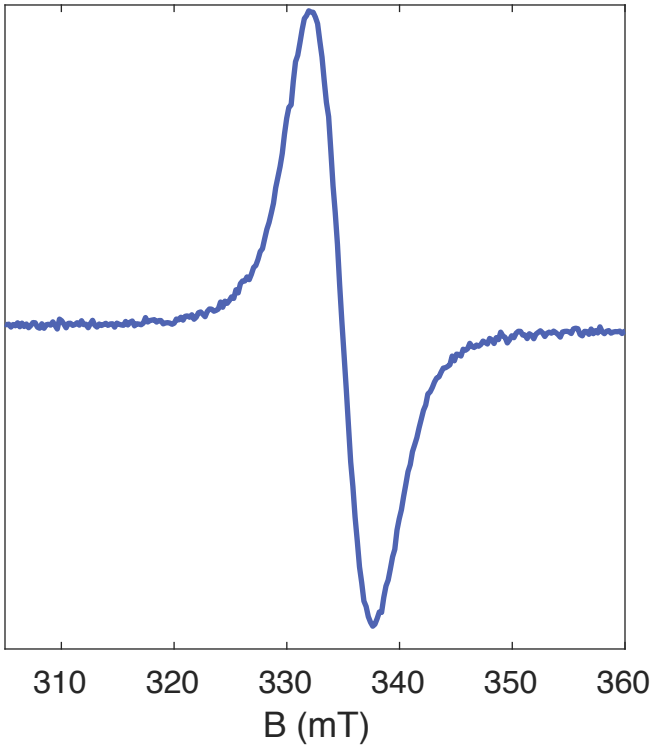

Figure S.4: Room-temperature X-band EPR spectrum of [(P_3^B)Fe($NNMe_2$)][BAr^F_4] (2 mM, 2-MeTHF).

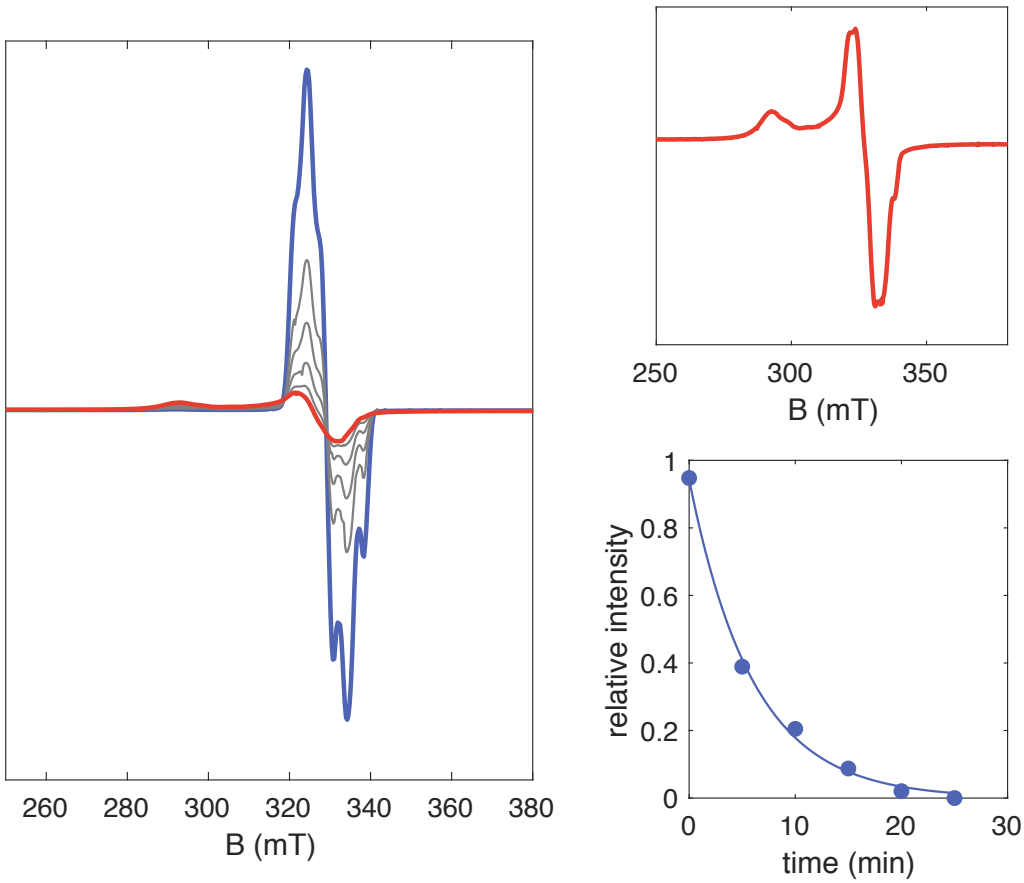

Figure S.5: The decay of $[(P_3{}^B)Fe(NNMe_2)]^-$, monitored by X-band EPR spectroscopy. The left panel shows a spectrum of $[(P_3{}^B)Fe(NNMe_2)]^-$ (10 mM, 2-MeTHF, 77 K) in blue. This sample was thawed to room temperature for five minutes, flash-frozen in liquid N_2, and its spectrum was recollected. Repeating this process several times lead to the monotonic decay of the signals attributed to $[(P_3{}^B)Fe(NNMe_2)]^-$ (gray spectra), producing a the final spectrum shown in red, which is also reproduced in the upper right panel. The approximate decay kinetics of the signal of $[(P_3{}^B)Fe(NNMe_2)]^-$ is shown in the lower right panel (closed circles), along with a mono-exponential fit (solid line).

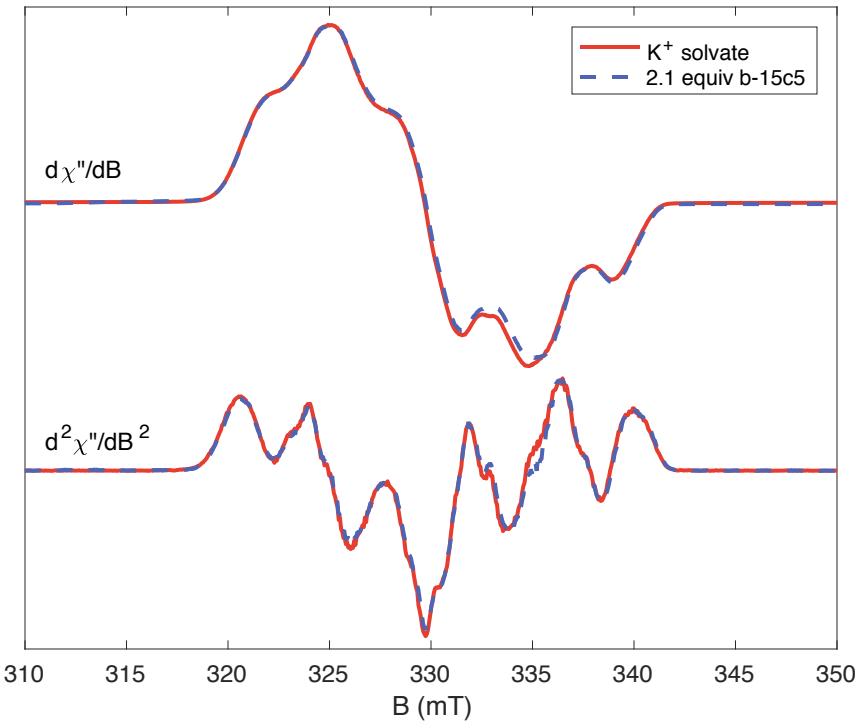

Figure S.6: Overlaid X-band EPR spectra of $[(P_3{}^B)Fe(NNMe_2)]^-$ with (dashed blue) and without (red) the addition of 2.1 equiv of benzo-15-c-5.

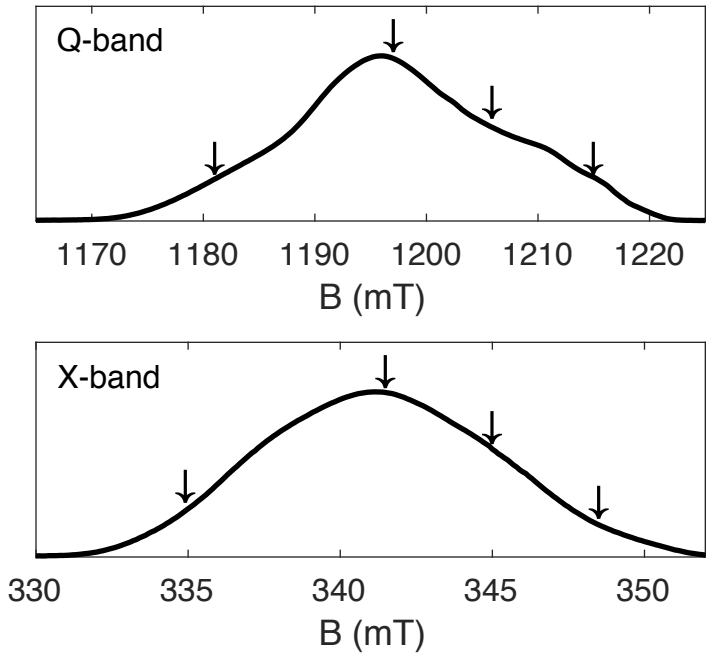

Figure S.7: ESE-detected Q- and X-band field-swept absorption spectra of $[(P_3{}^B)Fe(NNMe_2)]^-$ (2-MeTHF, 15 K). Field positions where ENDOR and/or HYSCORE data were collected are indicated by vertical arrows.

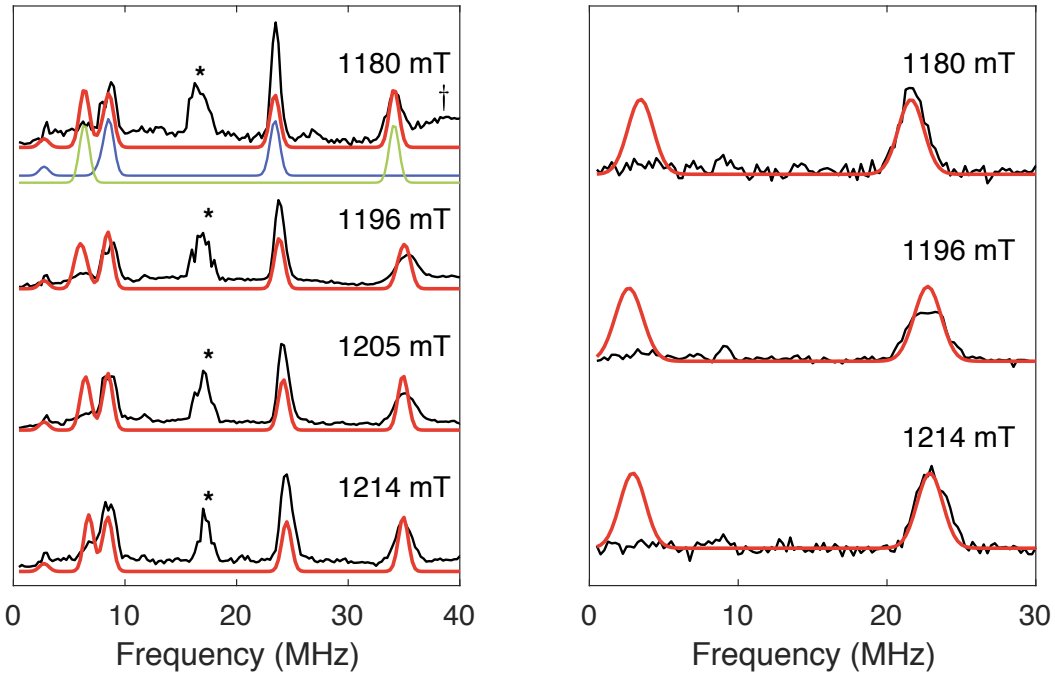

Figure S.8: Overlaid Q-band ENDOR spectra of $[(P_3{}^B)Fe(NNMe_2)]^-$; the field at which each spectrum was collected is indicated above each spectrum (*denotes a harmonic arising from weakly-coupled protons (ligand and/or solvent). (Left) Spectra collected on a natural abundance isotope (N.A.I.) sample. Raw data are shown in black, along with simulations in red. A deconvolution of the simulation in terms of the contributions from ^{11}B (blue) and $^{31}P_\gamma$ (green) is also shown for the spectrum collected at 1180 mT. See the main text for the full simulation parameters for these nuclei. (Right) Difference spectra between a sample of $[(P_3{}^B)Fe(NN(^{13}CH_3)_2)]^-$ and the N.A.I. sample, showing contributions from the N-^{13}C nuclei only. Raw data are shown in black, with simulations in red. See the main text for the full simulation parameters. Acquisition parameters: T = 15 K; MW frequency = 34.104 GHz; τ = 600 ns; MW pulse length = $(\pi/2, \pi)$ = (80, 160) ns; RF pulse length = 60 μs; shot repetition time (srt) = 5 ms.

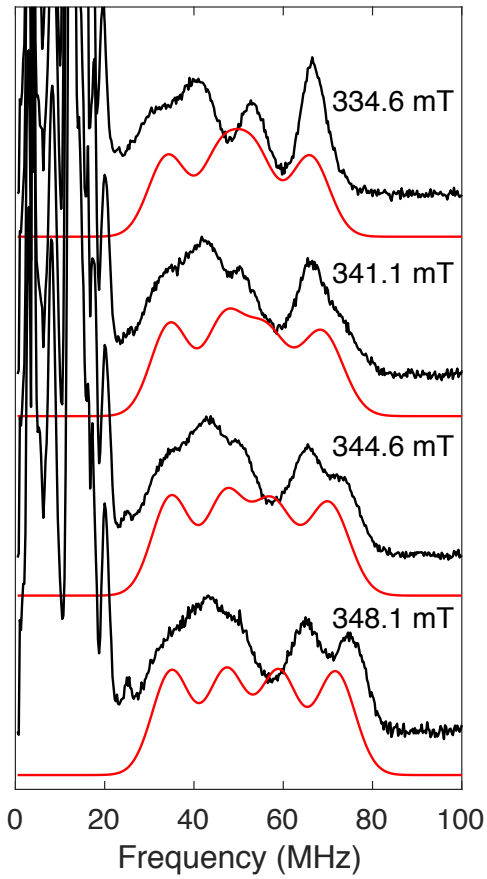

Figure S.9: Overlaid X-band ENDOR spectra of $[(P_3{}^B)Fe(NNMe_2)]^-$, showing resonances due to two strongly-coupled ^{31}P nuclei. The fields at which each spectrum was collected is indicated above each spectrum. Raw data are shown in black, with simulations shown in red. See the main text for the full simulation parameters for these nuclei. Acquisition parameters: T = 15 K; MW frequency = 9.734 GHz; τ = 240 ns; MW pulse length = $(\pi/2, \pi)$ = 40, 80 ns; RF pulse length = 40 μs; shot repetition time (srt) = 3 ms.

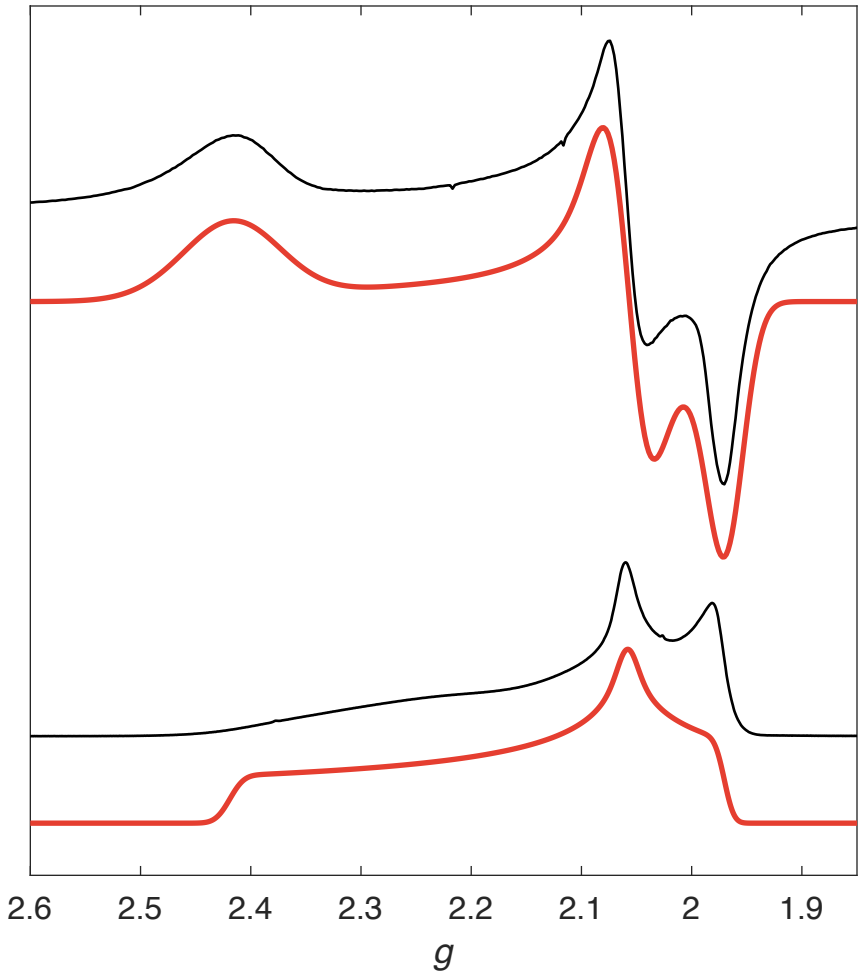

Figure S.10: (Top) CW X-band spectrum of [(P_3^B)Fe(NAd)][BAr^F_4] (5 mM, 2-MeTHF, 77 K). The experimental spectrum is shown in black, with a simulation in red. (Bottom) ESE-detected Q-band field-swept absorption spectrum of [(P_3^B)Fe(NAd)][BAr^F_4] (5 mM, 2-MeTHF, 10 K). The experimental spectrum is shown in black, with a simulation in red. Simulation parameters: g_{min} = 1.970, g_{mid} = 2.058, g_{max} = 2.419. To account for unresolved HFC, the CW spectrum was inhomogeneously-broadened using `HStrain = [187 190 400]`.

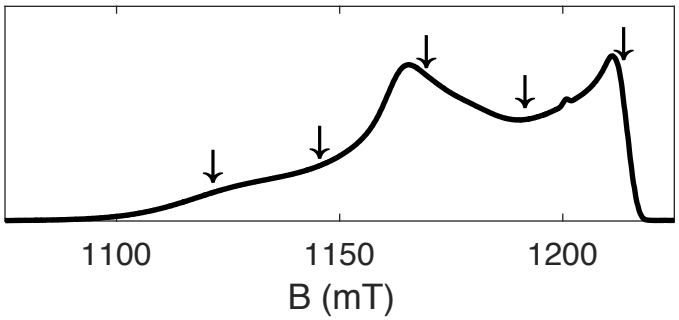

Figure S.11: ESE-detected Q-band field-swept absorption spectrum of $[(P_3{}^B)Fe(NNMe_2)]^+$ (2-MeTHF, 12 K). Field positions where ENDOR and/or HYSCORE data were collected are indicated by vertical arrows.

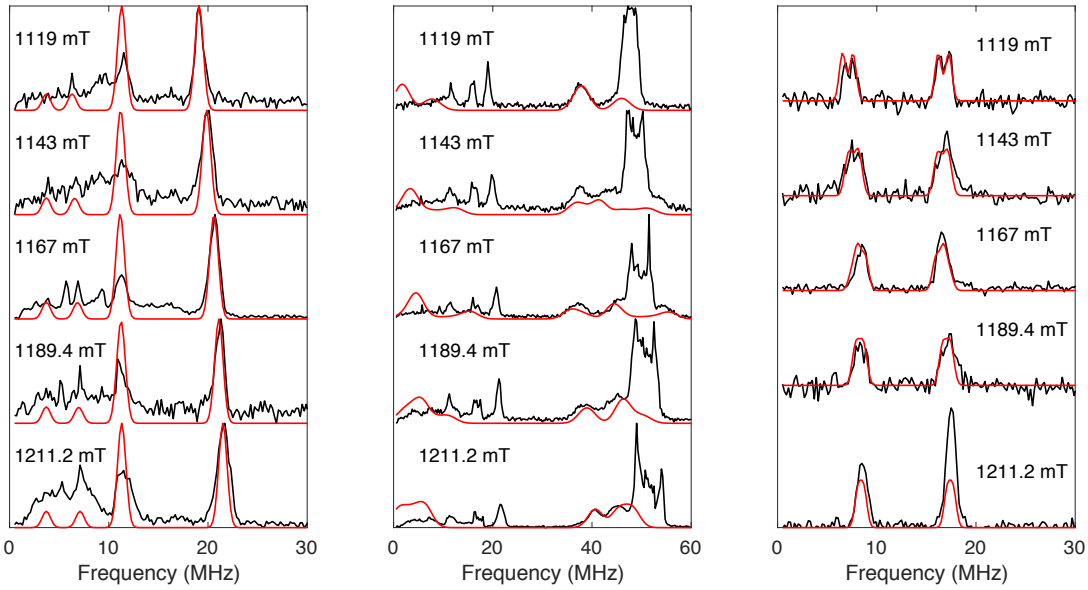

Figure S.12: Overlaid Q-band ENDOR spectra of $[(P_3{}^B)Fe(NNMe_2)]^+$; the field at which each spectrum was collected is indicated above each spectrum. (Left) Low frequency region of spectra collected on a natural abundance isotope (N.A.I.) sample. Raw data are shown in black, along with simulation of a single ^{11}B nucleus in red. (Middle) Wide frequency scans showing the contributions from three ^{31}P nuclei. Raw data are shown in black, with simulations in red. The features centered around 50 MHz are due to weakly-coupled ^{1}H nuclei (ligand and solvent). (Right) Difference spectra between a sample of $[(P_3{}^B)Fe(NN(^{13}CH_3)_2)]^+$ and the N.A.I. sample, showing contributions from the N-^{13}C nuclei only. Raw data are shown in black, with simulations in red. See the main text for the full simulation parameters. Acquisition parameters: T = 15 K; MW frequency = 34.044 GHz; τ = 600 ns; MW pulse length = $(\pi/2, \pi)$ = 80, 160 ns; RF pulse length = 60 μs; shot repetition time (srt) = 5 ms.

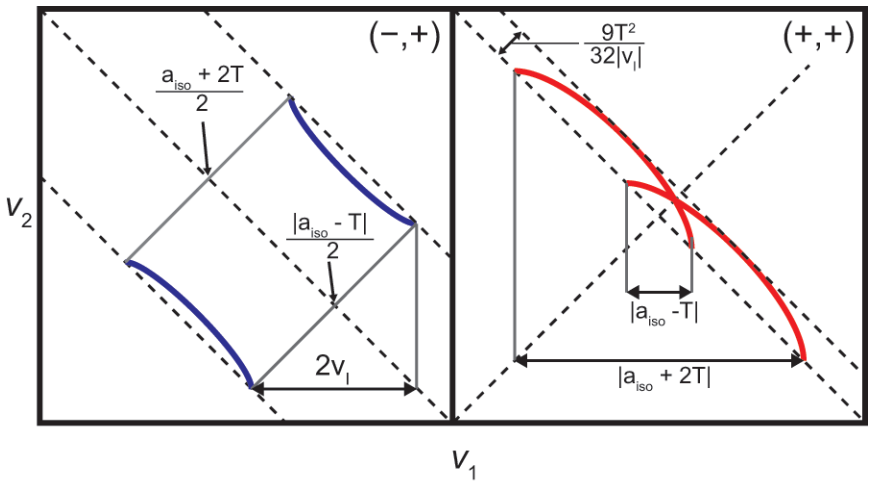

Figure S.13: Sample HYSCORE powder patterns for an $S = 1/2, I = 1/2$ spin system with an axial hyperfine tensor which contains isotropic (a_{iso}) and dipolar ($\boldsymbol{T}$) contributions. Blue correlation ridges represent the strong coupling case; red correlation ridges represent the weak coupling case.

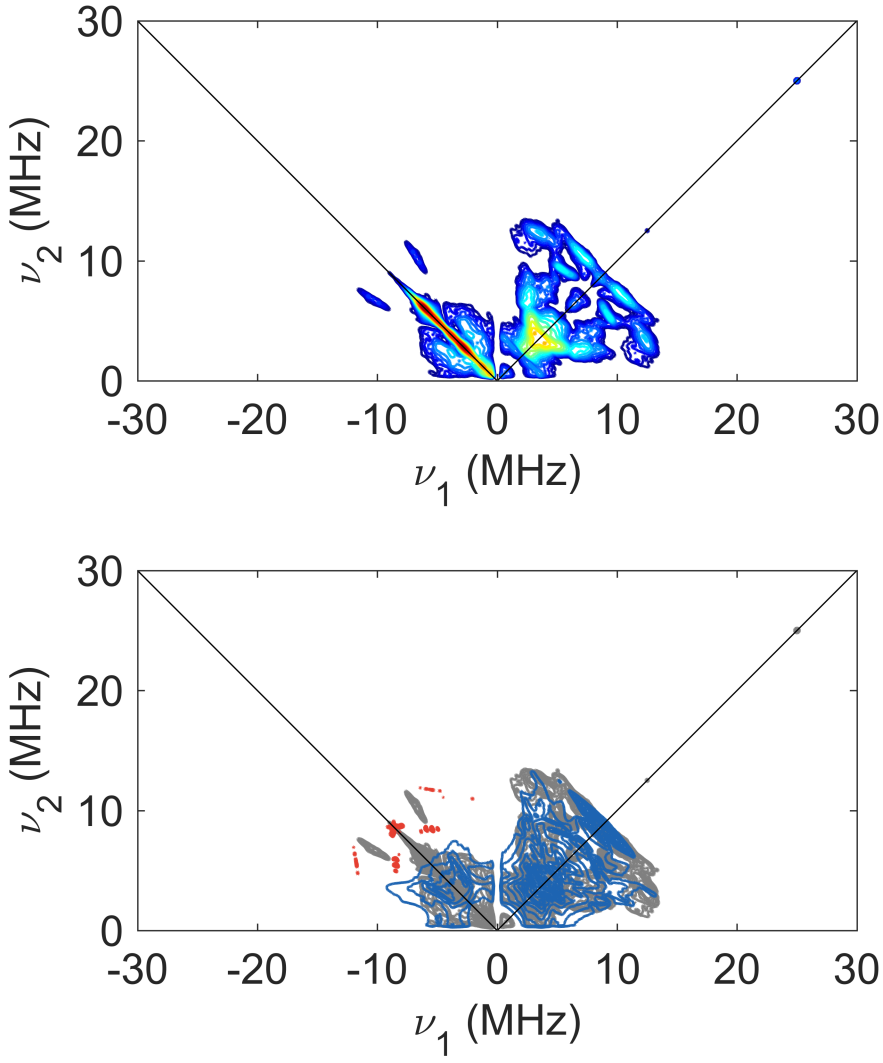

Figure S.14: HYSCORE spectrum of $[(P_3{}^B)Fe(^{14}N^{14}NMe_2)]^-$ collected at a field of 1180 mT. The raw data are presented in the top panel, with intensities encoded by the color map. The bottom panel reproduces the experimental spectrum in grey, and overlays simulations due to N_α (red) and N_β (blue). Note that the simulations were calculated for each nucleus separately, and thus do not show effects due to multinuclear coherences. See Table S.23 for simulation details.

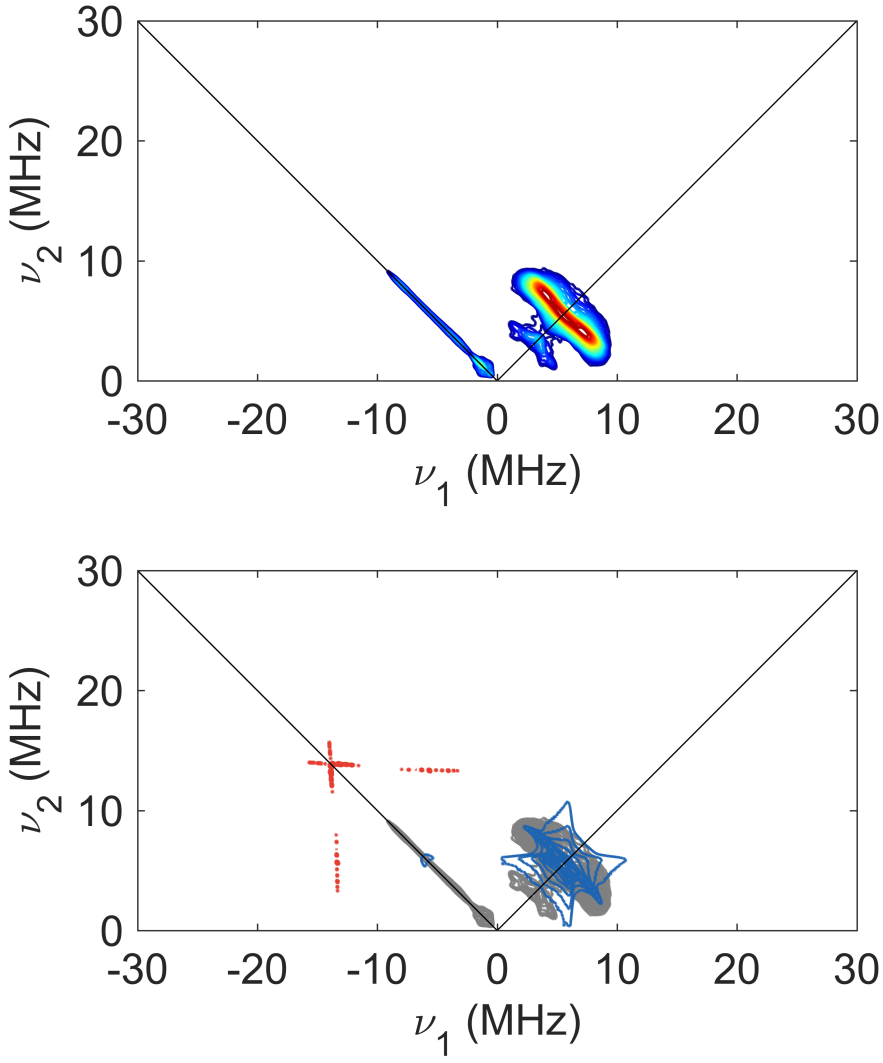

Figure S.15: HYSCORE spectrum of $[(P_3{}^B)Fe(^{15}N^{15}NMe_2)]^-$ collected at a field of 1180 mT. The raw data are presented in the top panel, with intensities encoded by the color map. The bottom panel reproduces the experimental spectrum in grey, and overlays simulations due to N_α (red) and N_β (blue). Note that the simulations were calculated for each nucleus separately, and thus do not show effects due to multinuclear coherences. See Table S.23 for simulation details.

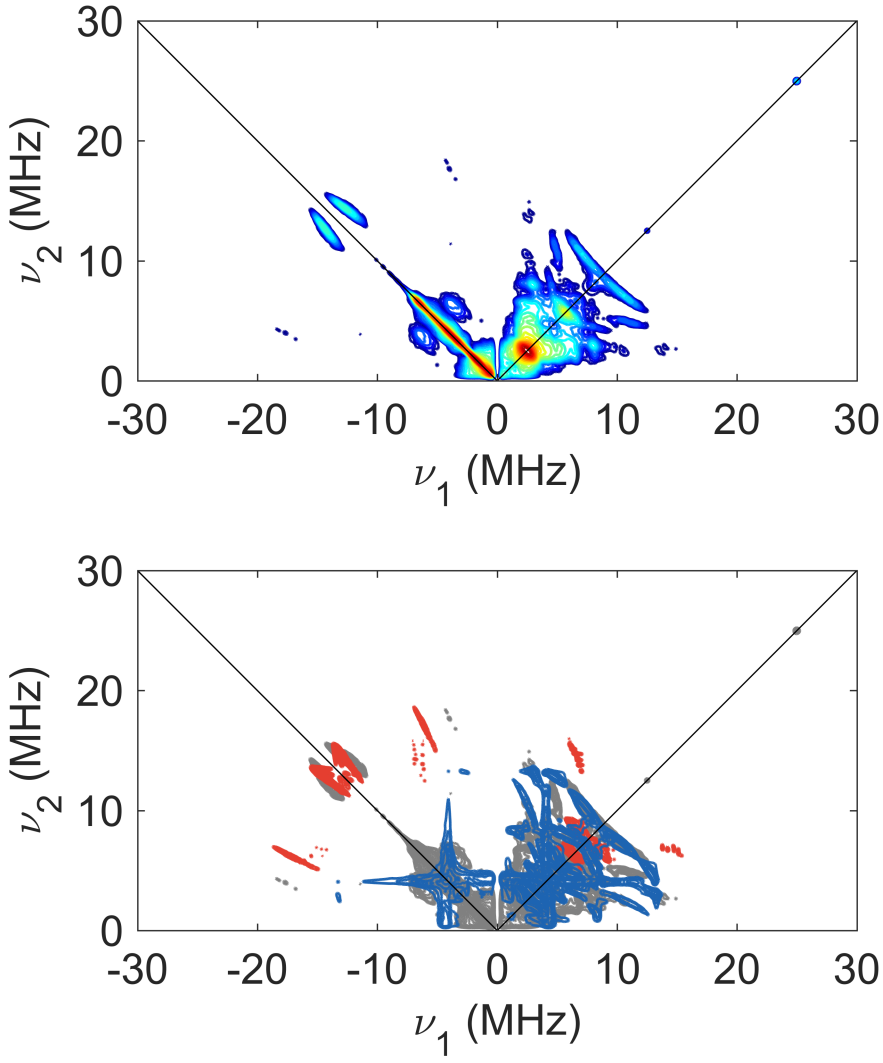

Figure S.16: HYSCORE spectrum of $[(P_3{}^B)Fe(^{14}N^{14}NMe_2)]^-$ collected at a field of 1196 mT. The raw data are presented in the top panel, with intensities encoded by the color map. The bottom panel reproduces the experimental spectrum in grey, and overlays simulations due to N_α (red) and N_β (blue). Note that the simulations were calculated for each nucleus separately, and thus do not show effects due to multinuclear coherences. See Table S.23 for simulation details.

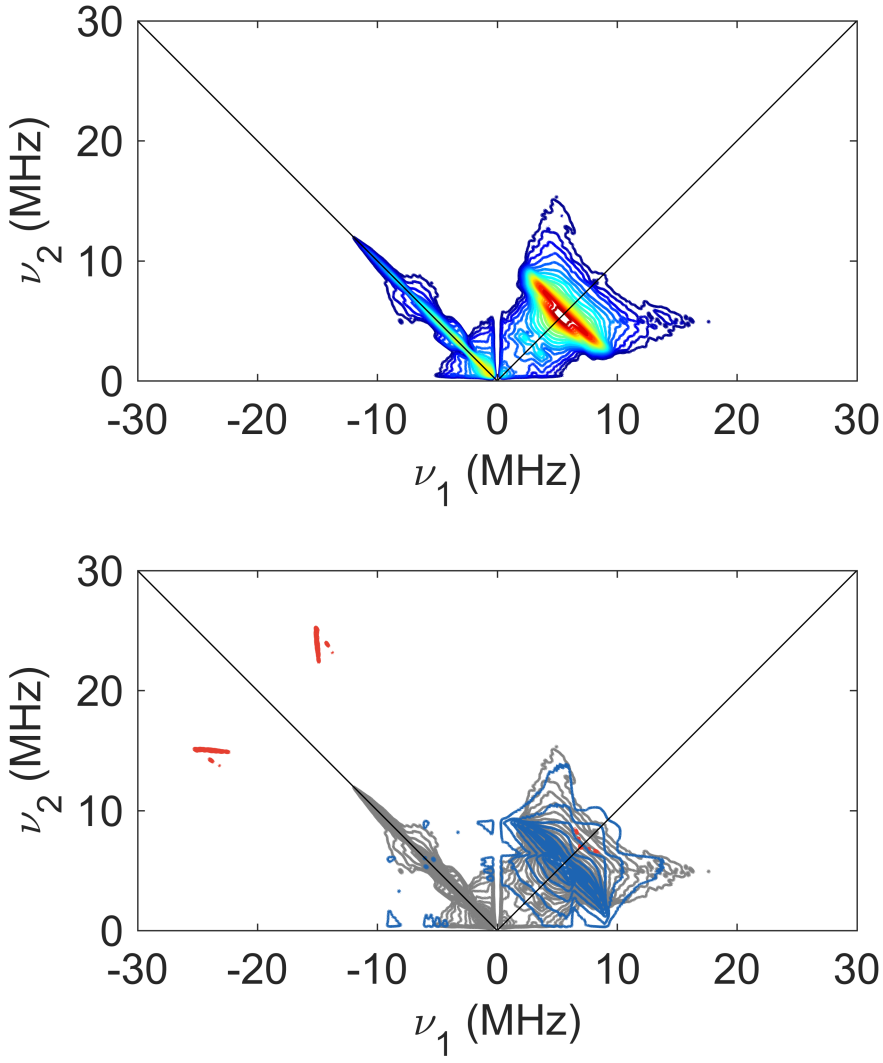

Figure S.17: HYSCORE spectrum of $[(P_3{}^B)Fe(^{15}N^{15}NMe_2)]^-$ collected at a field of 1196 mT. The raw data are presented in the top panel, with intensities encoded by the color map. The bottom panel reproduces the experimental spectrum in grey, and overlays simulations due to N_α (red) and N_β (blue). Note that the simulations were calculated for each nucleus separately, and thus do not show effects due to multinuclear coherences. See Table S.23 for simulation details.

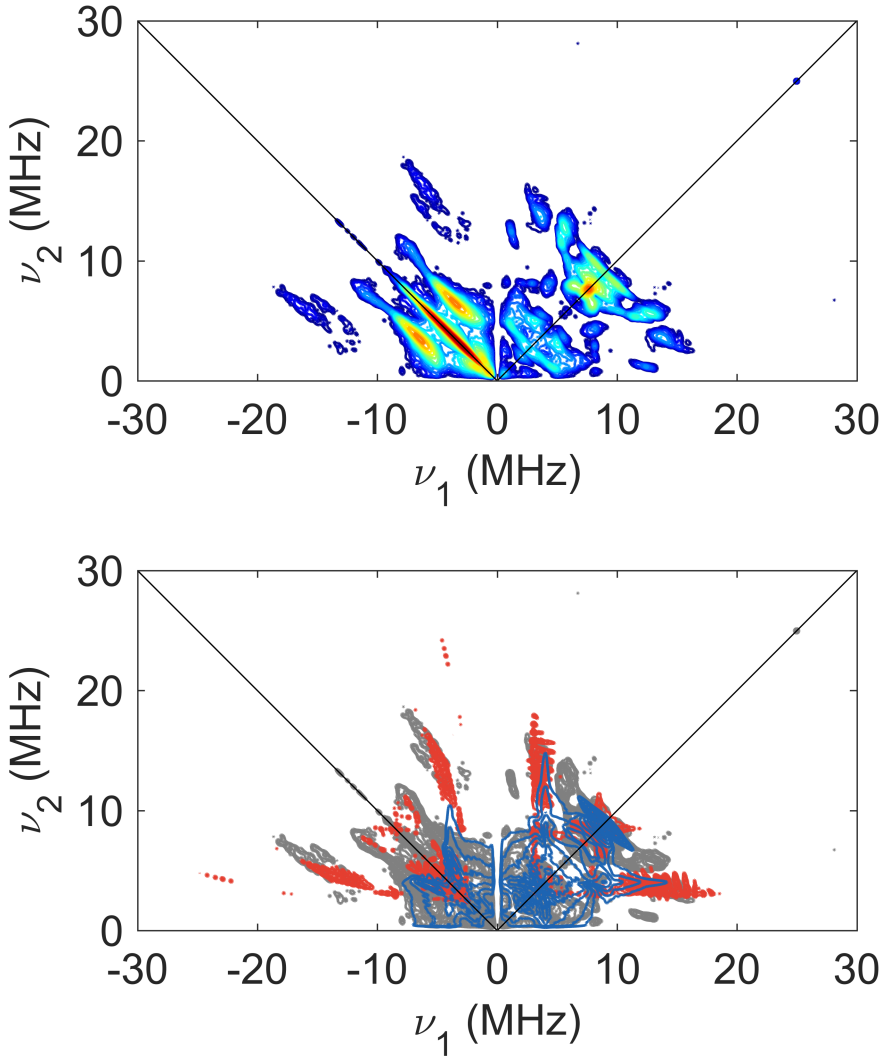

Figure S.18: HYSCORE spectrum of $[(P_3{}^B)Fe(^{14}N^{14}NMe_2)]^-$ collected at a field of 1214 mT. The raw data are presented in the top panel, with intensities encoded by the color map. The bottom panel reproduces the experimental spectrum in grey, and overlays simulations due to N_α (red) and N_β (blue). Note that the simulations were calculated for each nucleus separately, and thus do not show effects due to multinuclear coherences. See Table S.23 for simulation details.

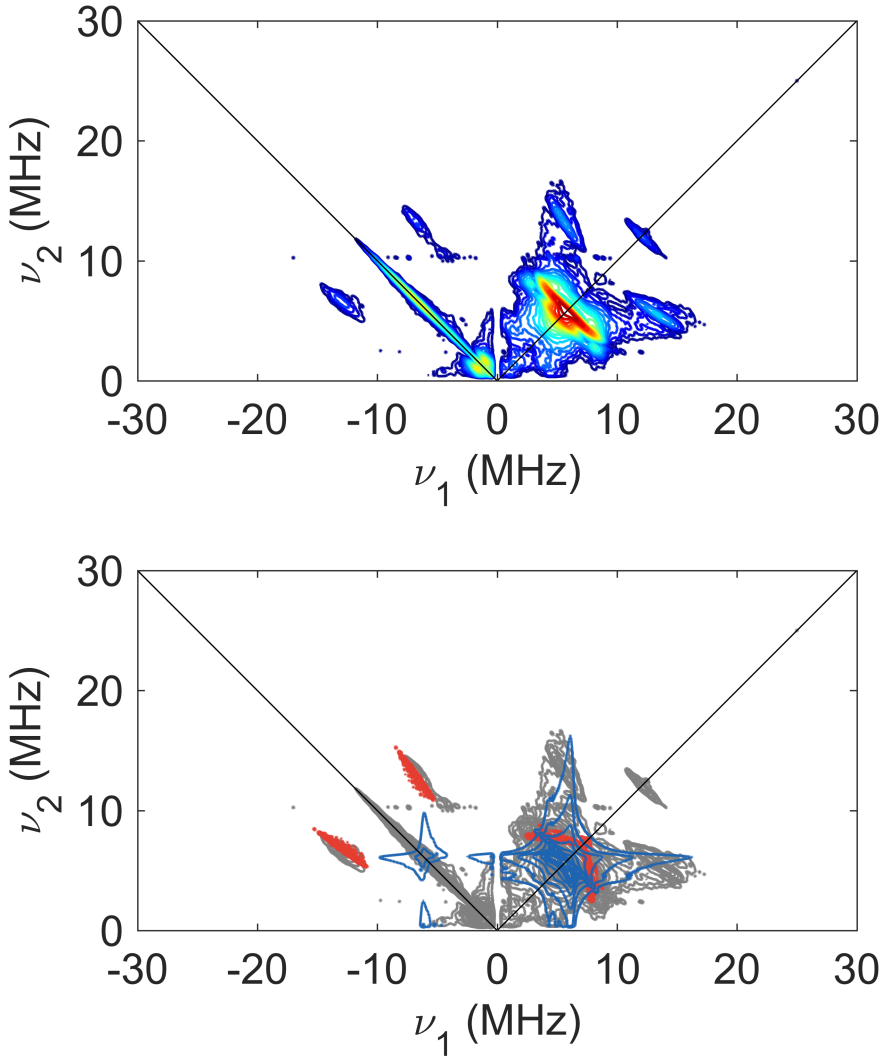

Figure S.19: HYSCORE spectrum of $[(P_3{}^B)Fe(^{15}N^{15}NMe_2)]^-$ collected at a field of 1214 mT. The raw data are presented in the top panel, with intensities encoded by the color map. The bottom panel reproduces the experimental spectrum in grey, and overlays simulations due to N_α (red) and N_β (blue). Note that the simulations were calculated for each nucleus separately, and thus do not show effects due to multinuclear coherences. See Table S.23 for simulation details.

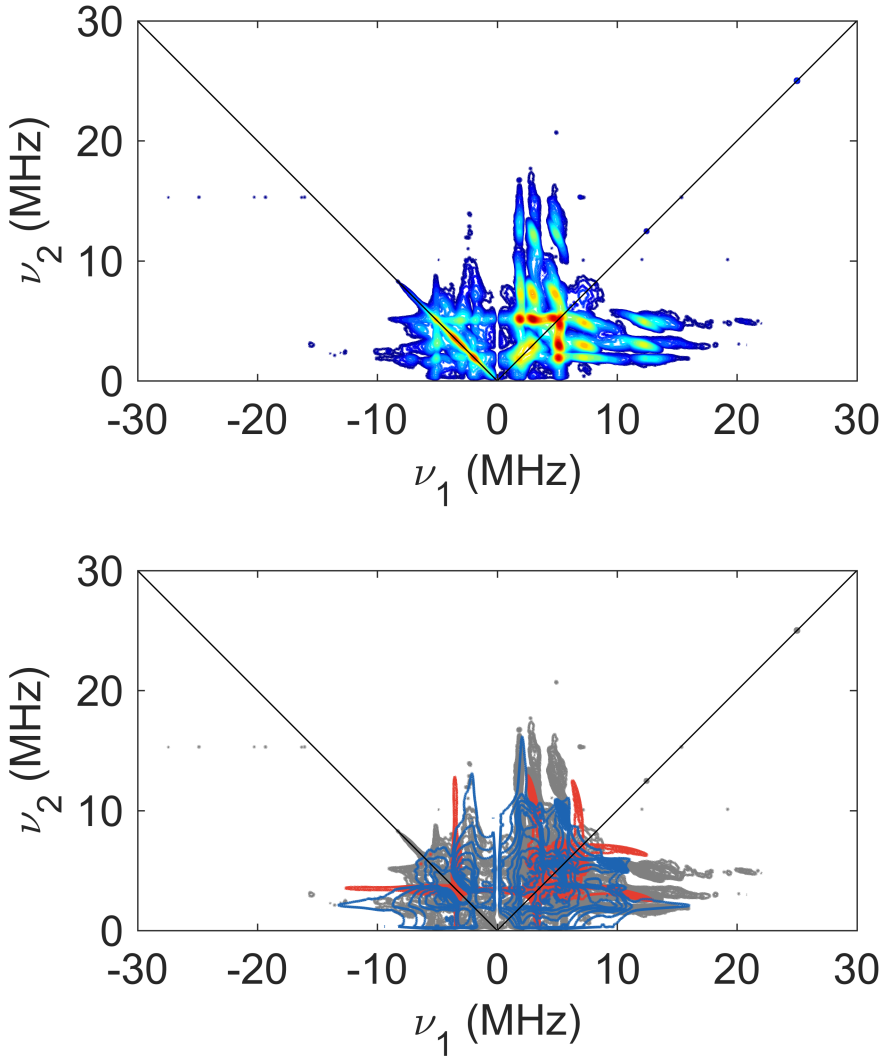

Figure S.20: HYSCORE spectrum of $[(P_3{}^B)Fe(^{14}N^{14}NMe_2)]^+$ collected at a field of 1119 mT. The raw data are presented in the top panel, with intensities encoded by the color map. The bottom panel reproduces the experimental spectrum in grey, and overlays simulations due to N_α (red) and N_β (blue). Note that the simulations were calculated for each nucleus separately, and thus do not show effects due to multinuclear coherences. See Table S.23 for simulation details.

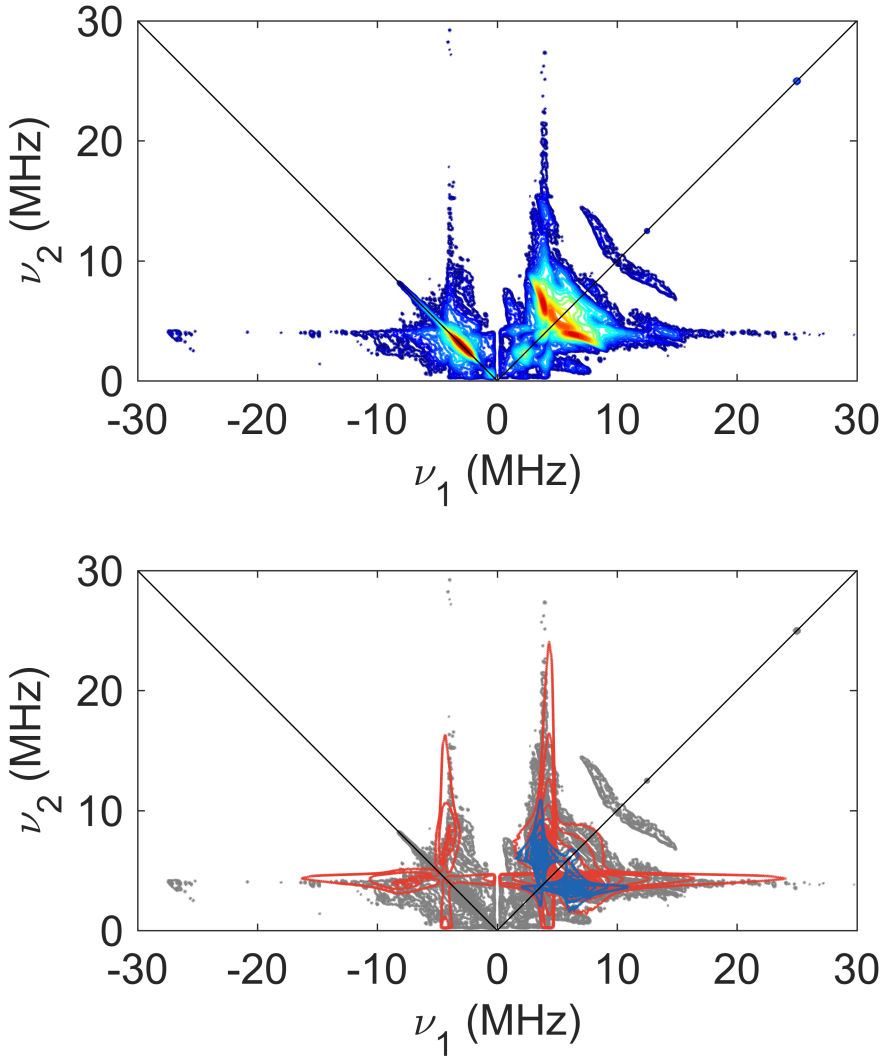

Figure S.21: HYSCORE spectrum of $[(P_3{}^B)Fe(^{15}N^{15}NMe_2)]^+$ collected at a field of 1119 mT. The raw data are presented in the top panel, with intensities encoded by the color map. The bottom panel reproduces the experimental spectrum in grey, and overlays simulations due to N_α (red) and N_β (blue). Note that the simulations were calculated for each nucleus separately, and thus do not show effects due to multinuclear coherences (cf. Figure S.22). See Table S.23 for simulation details.

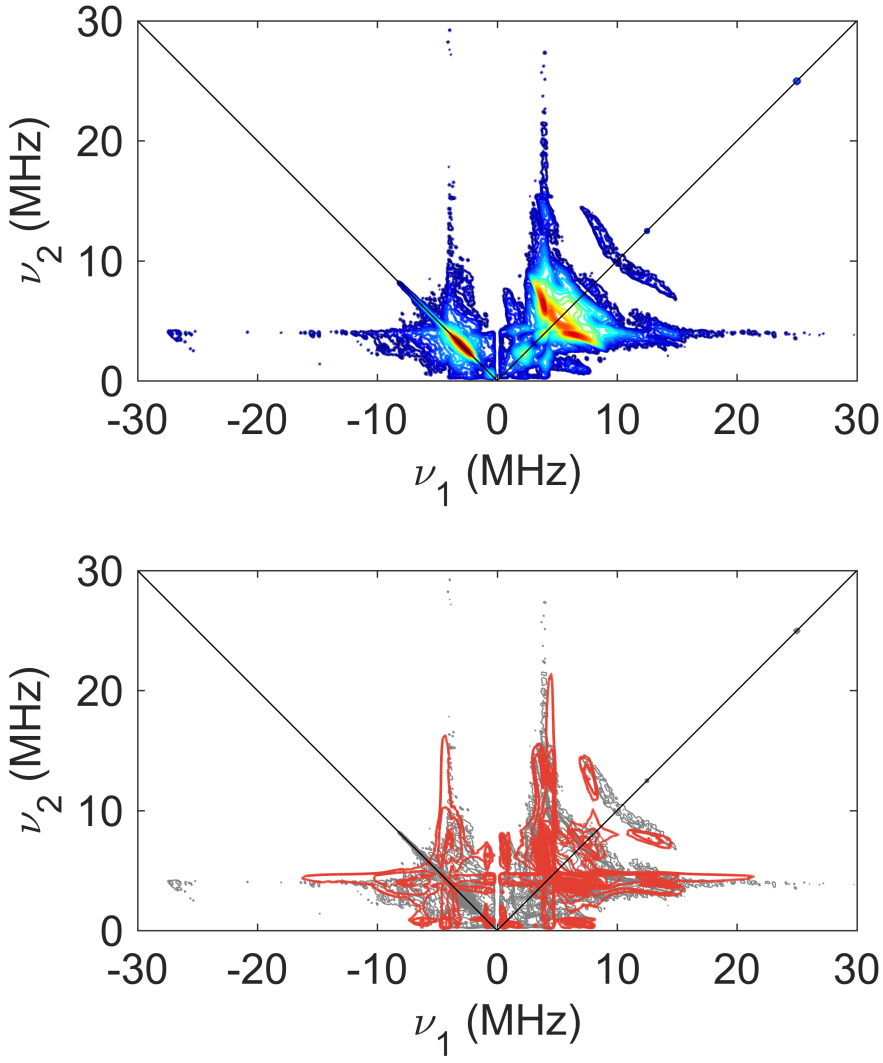

Figure S.22: HYSCORE spectrum of $[(P_3{}^B)Fe(^{15}N^{15}NMe_2)]^+$ collected at a field of 1119 mT. The raw data are presented in the top panel, with intensities encoded by the color map. The bottom panel reproduces the experimental spectrum in grey, and overlays a simulation (red) in which N_α and N_β were treated simultaneously to show the effect of multinuclear coherences (cf. Figure S.21). See Table S.23 for simulation details.

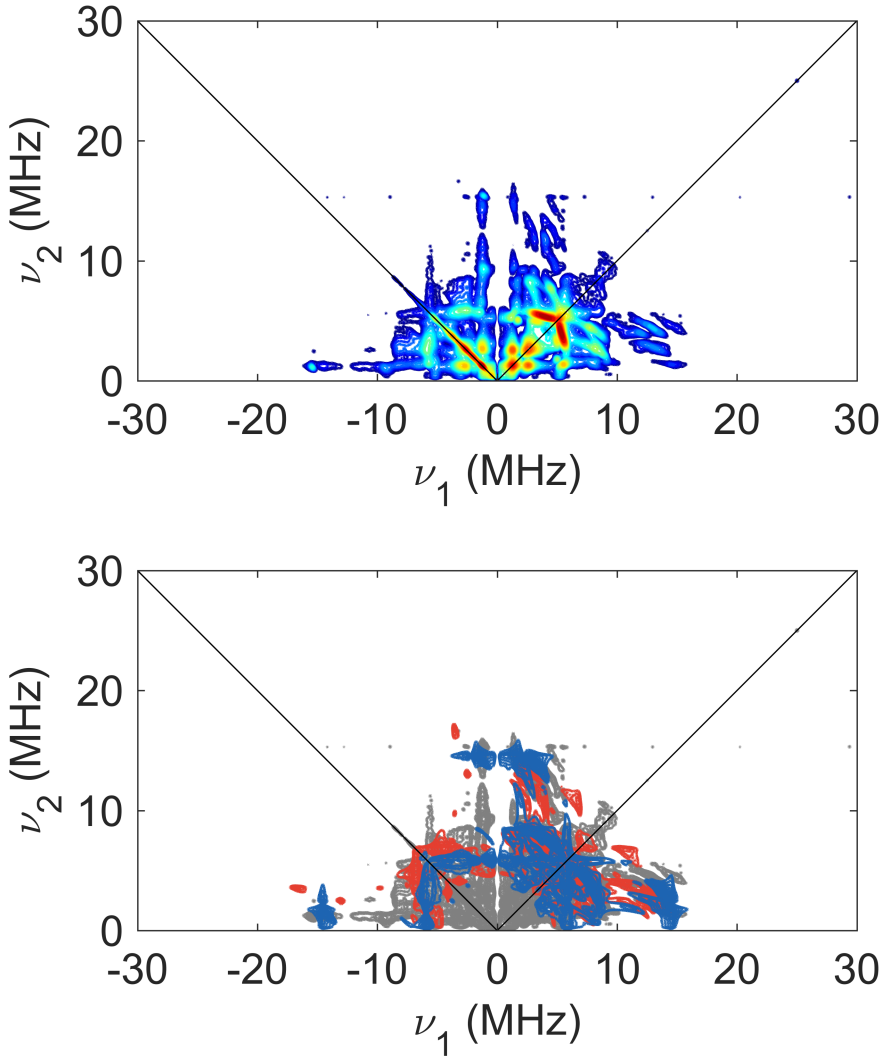

Figure S.23: HYSCORE spectrum of $[(P_3{}^B)Fe(^{14}N^{14}NMe_2)]^+$ collected at a field of 1167 mT. The raw data are presented in the top panel, with intensities encoded by the color map. The bottom panel reproduces the experimental spectrum in grey, and overlays simulations due to N_α (red) and N_β (blue). Note that the simulations were calculated for each nucleus separately, and thus do not show effects due to multinuclear coherences. See Table S.23 for simulation details.

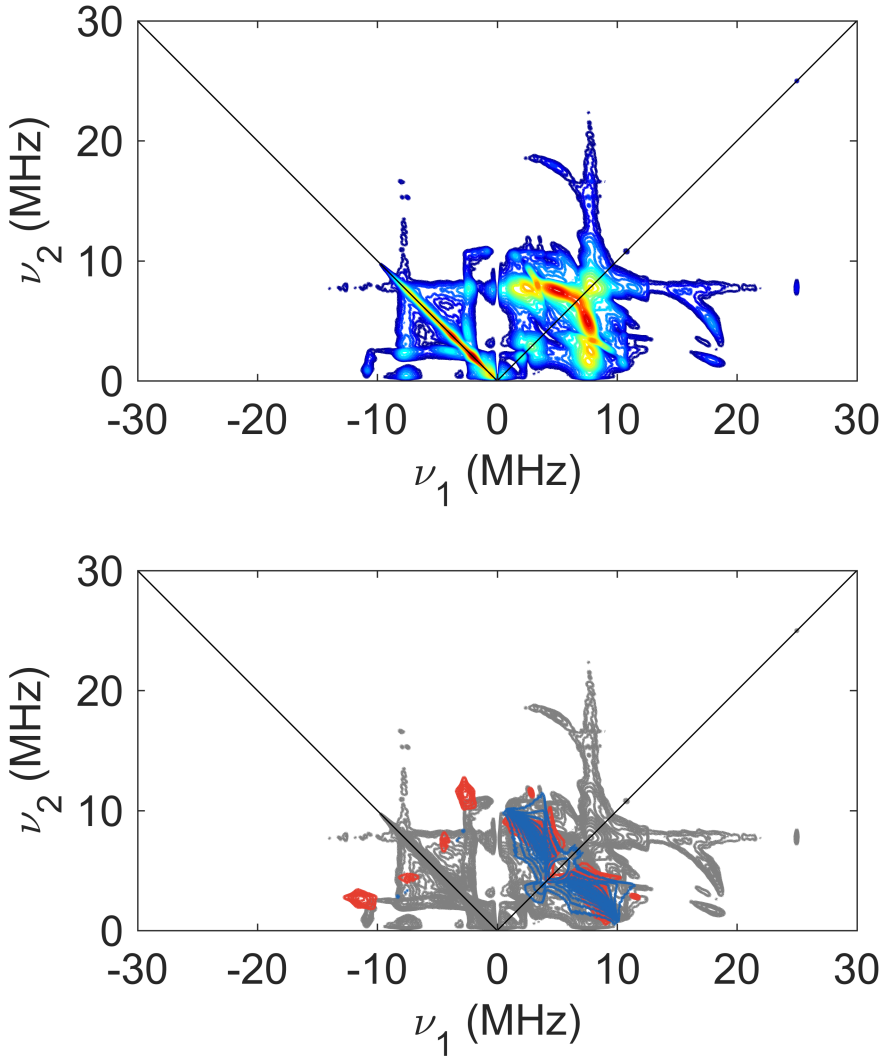

Figure S.24: HYSCORE spectrum of $[(P_3{}^B)Fe(^{15}N^{15}NMe_2)]^+$ collected at a field of 1167 mT. The raw data are presented in the top panel, with intensities encoded by the color map. The bottom panel reproduces the experimental spectrum in grey, and overlays simulations due to N_α (red) and N_β (blue). Note that the simulations were calculated for each nucleus separately, and thus do not show effects due to multinuclear coherences. Such coherences can be observed in this spectrum in the $(+,+)$ quadrant in the region spanned by $(5, 20)$ to $(20, 5)$ MHz (cf. Figure S.25). See Table S.23 for simulation details.

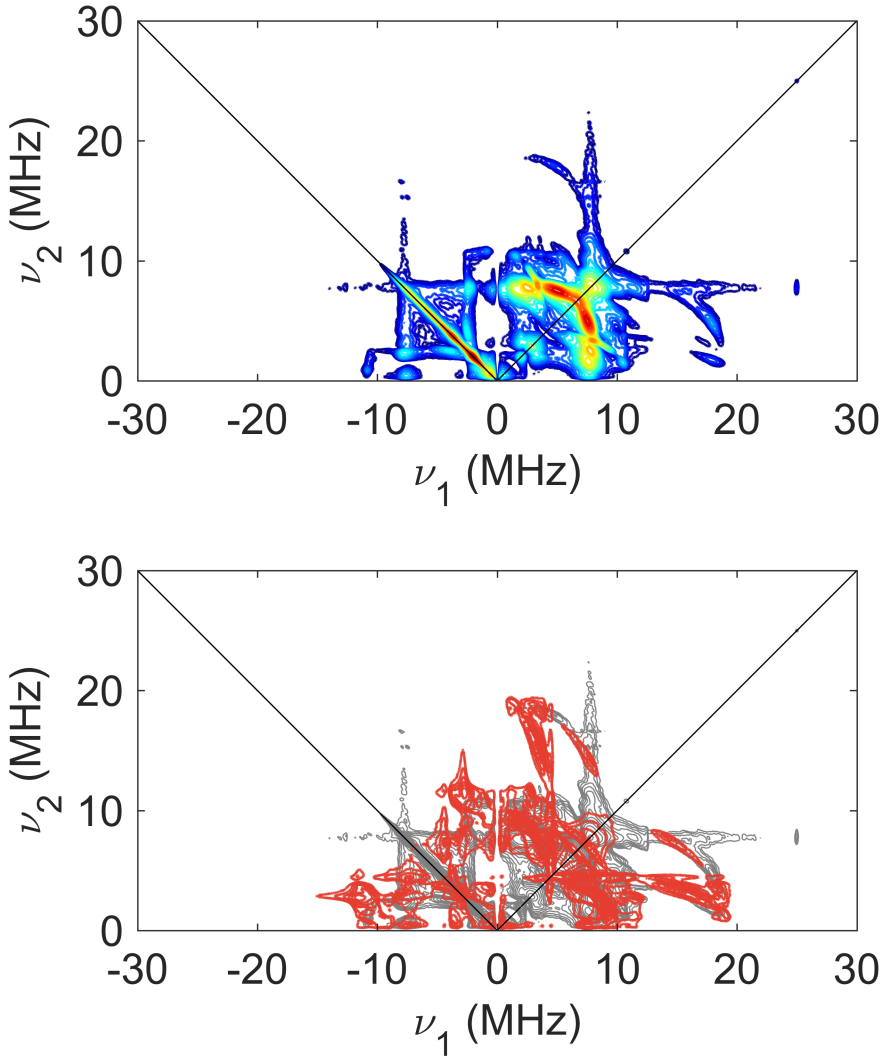

Figure S.25: HYSCORE spectrum of $[(P_3{}^B)Fe(^{15}N^{15}NMe_2)]^+$ collected at a field of 1167 mT. The raw data are presented in the top panel, with intensities encoded by the color map. The bottom panel reproduces the experimental spectrum in grey, and overlays a simulation (red) in which N_α and N_β were treated simultaneously to show the effect of multinuclear coherences (cf. Figure S.24). See Table S.23 for simulation details.

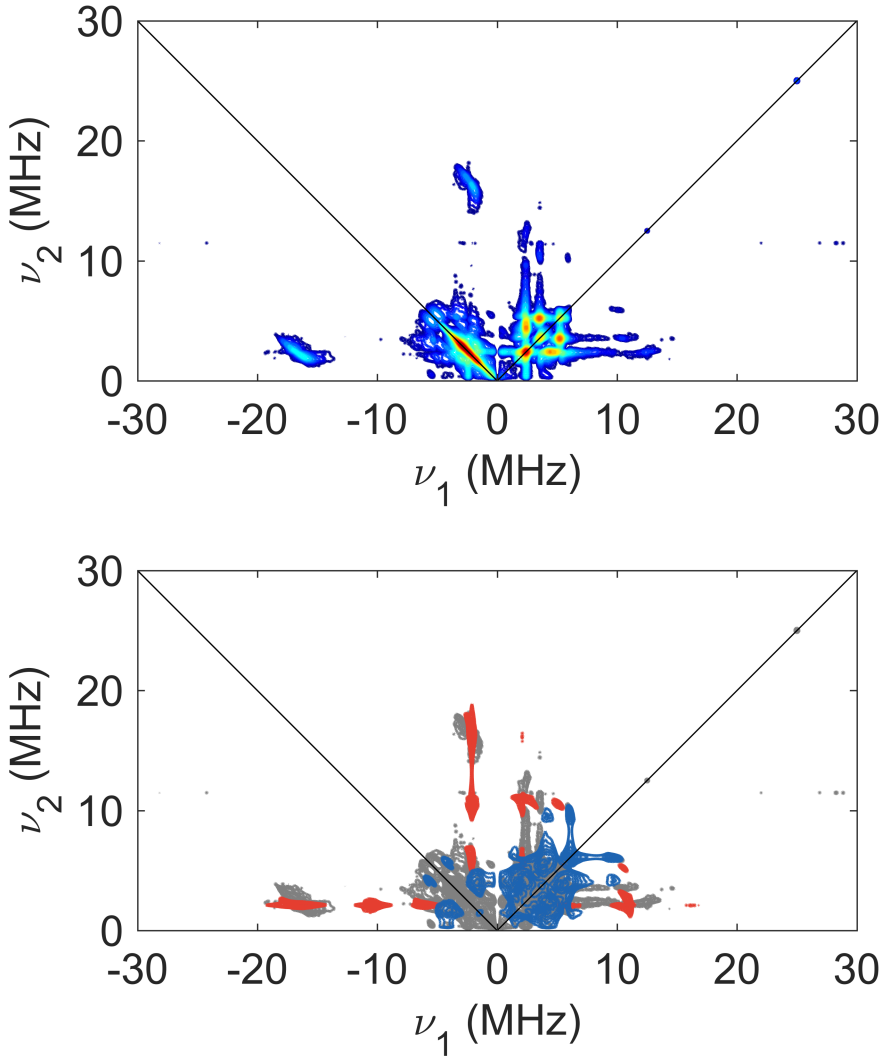

Figure S.26: HYSCORE spectrum of $[(P_3{}^B)Fe(^{14}N^{14}NMe_2)]^+$ collected at a field of 1211 mT. The raw data are presented in the top panel, with intensities encoded by the color map. The bottom panel reproduces the experimental spectrum in grey, and overlays simulations due to N_α (red) and N_β (blue). Note that the simulations were calculated for each nucleus separately, and thus do not show effects due to multinuclear coherences. See Table S.23 for simulation details.

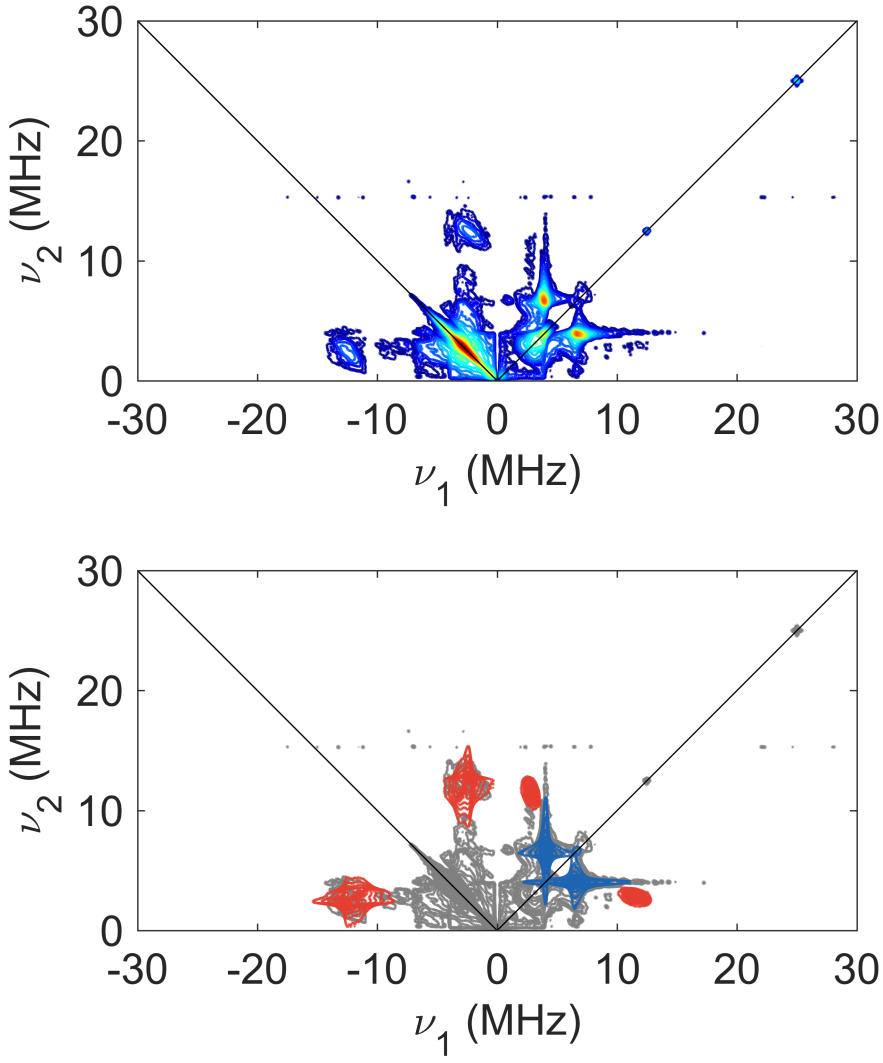

Figure S.27: HYSCORE spectrum of $[(P_3{}^B)Fe(^{15}N^{15}NMe_2)]^+$ collected at a field of 1211 mT. The raw data are presented in the top panel, with intensities encoded by the color map. The bottom panel reproduces the experimental spectrum in grey, and overlays simulations due to N_α (red) and N_β (blue). Note that the simulations were calculated for each nucleus separately, and thus do not show effects due to multinuclear coherences. See Table S.23 for simulation details.

S.9 IR Spectra

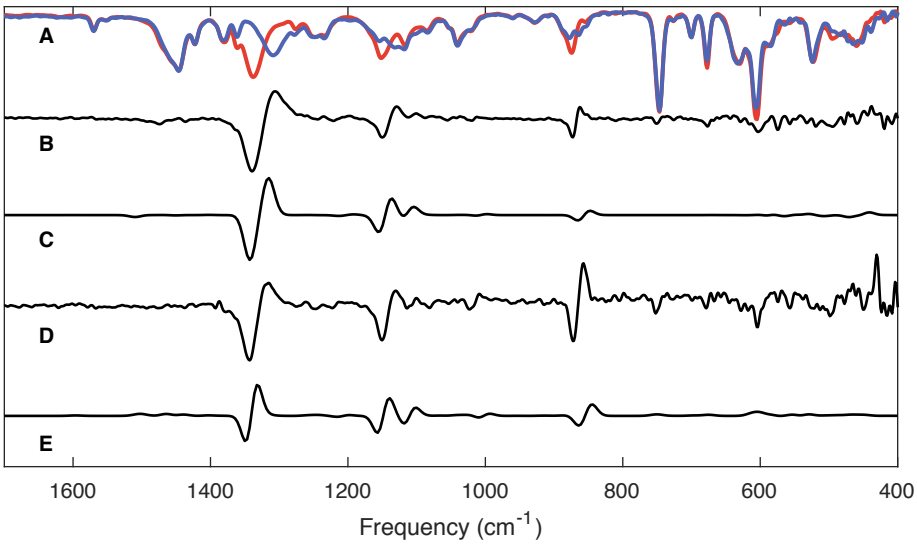

Figure S.28: IR spectra of (P_3^B)Fe($NNMe_2$) isotopologues. (A) Overlaid spectra of a natural abundance isotope (N.A.I.) sample (red), and that of (P_3^B)Fe($^{15}N^{15}NMe_2$) (blue). (B) Experimental N.A.I.–^{15}N difference spectrum. (C) DFT-calculated N.A.I.–^{15}N difference spectrum. (D) Experimental N.A.I–^{13}C difference spectrum (the ^{13}C sample is that of (P_3^B)Fe($NN(^{13}CH_3)_2$)). (E) DFT-calculated N.A.I.–^{13}C difference spectrum. Note that the N–N stretching vibration at 1337 cm^{-1} is mixed with N–C stretching modes.

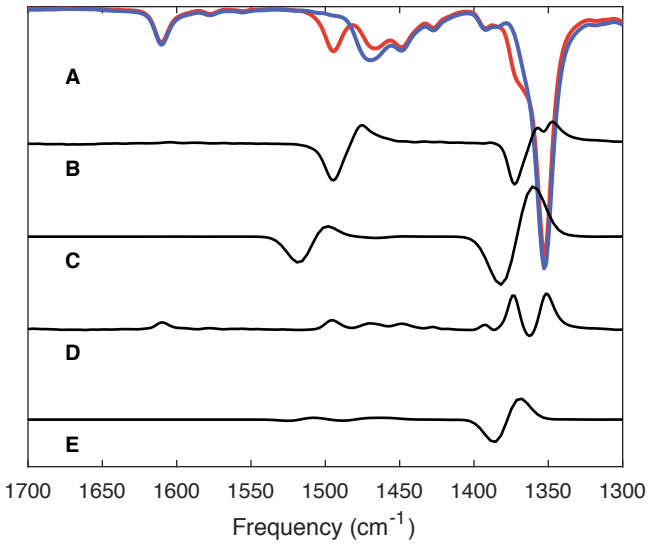

Figure S.29: IR spectra of [(P_3^B)Fe(NNMe$_2$)][BAr^F_4] isotopologues. (A) Overlaid spectra of a natural abundance isotope (N.A.I.) sample (red), and that of [(P_3^B)Fe(^{15}N^{15}NMe$_2$)]$^+$ (blue). (B) Experimental N.A.I.–^{15}N difference spectrum. (C) DFT-calculated N.A.I.–^{15}N difference spectrum. (D) Experimental N.A.I–^{13}C difference spectrum (the ^{13}C sample is that of [(P_3^B)Fe(NN(^{13}CH$_3$)$_2$)]$^+$). (E) DFT-calculated N.A.I.–^{13}C difference spectrum. The N–N stretching vibration appears at 1495 cm^{-1}. Note that at lower frequencies, the IR spectra are dominated by resonances from the [BAr^F_4]$^-$ counterion, and reliable difference spectra could not be collected.

S.10 UV-vis Spectra

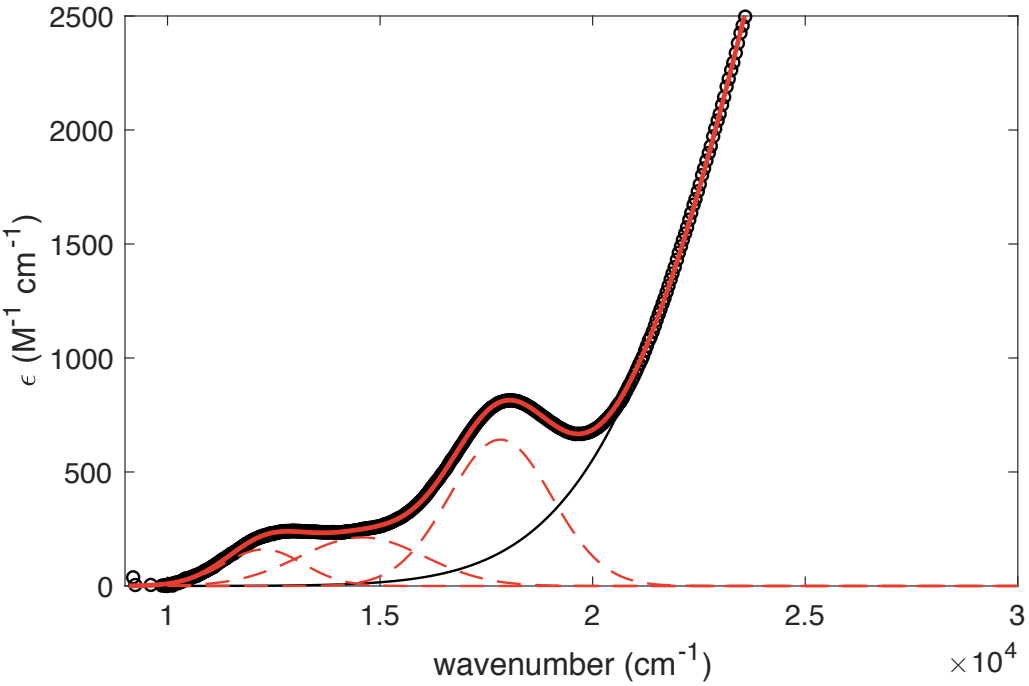

Figure S.30: UV-vis spectrum of ($P_3{}^B$)Fe($NNMe_2$) (2-MeTHF, 153 K). The experimental data are shown as open circles, with a Gaussian spectra deconvolution shown in red. Individual sub-components are shown as dashed red and solid black lines. See Table S.5 for the fitting parameters.

S.11 Mössbauer Spectra

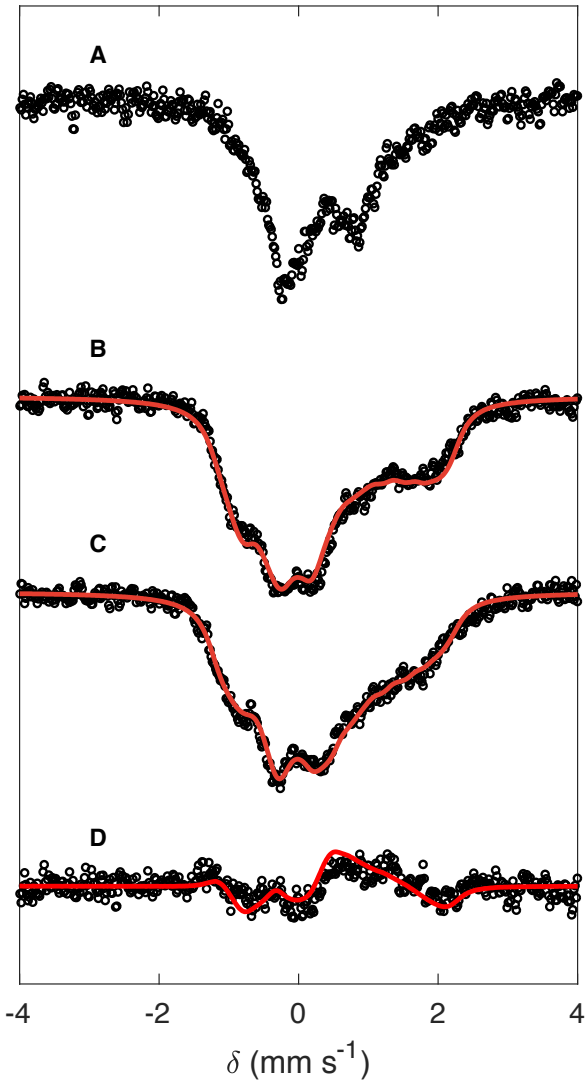

Figure S.31: 80 K Mössbauer spectra of [(P_3^B)Fe($NNMe_2$)][BAr^F_4]. Raw data are shown as open circles, with simulations shown as solid red lines; individual sub-components are plotted in blue and black. (A) Polycrystalline sample (natural abundance) collected in a parallel 50 mT field. (B) Frozen solution sample of [(P_3^B)Fe($NNMe_2$)][BAr^F_4] (40 mM, natural abundance, 2-MeTHF), collected in a parallel 50 mT field. (C) Frozen solution sample of [(P_3^B)Fe($NNMe_2$)][BAr^F_4] (40 mM, natural abundance, 2-MeTHF), collected in a perpendicular 50 mT field. (D) Difference spectrum (B)−(C). See Table S.6 for fit parameters.

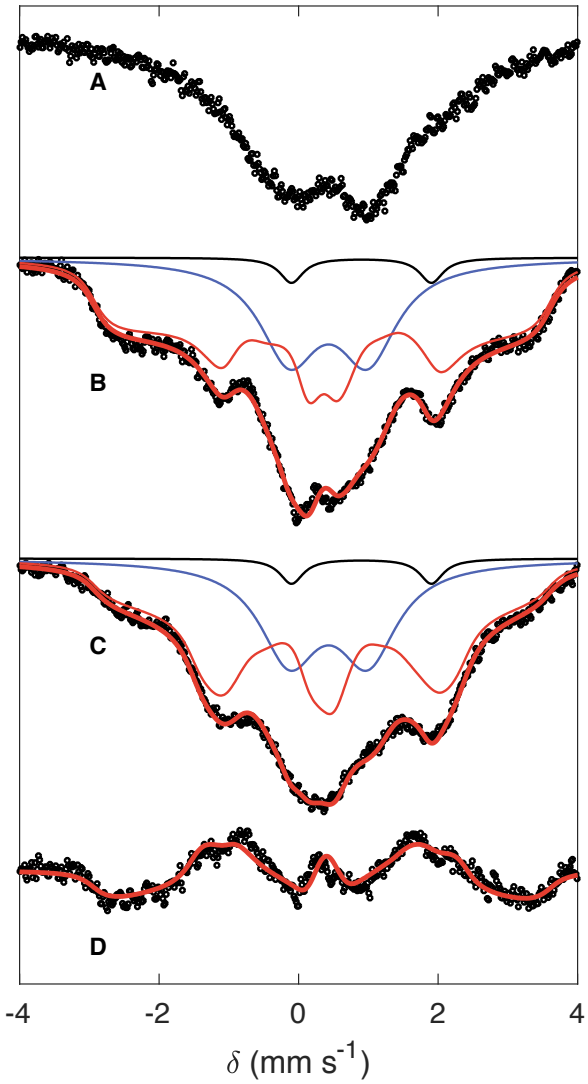

Figure S.32: 80 K Mössbauer spectra of $[(P_3{}^B)Fe(NNMe_2)]^-$. Raw data are shown as open circles, with simulations shown as solid red lines; individual sub-components are plotted in red, blue, and black. (A) Frozen solution sample of $[(P_3{}^B)^{57}Fe(NNMe_2)]^-$ (4 mM, 2-MeTHF), collected in zero applied field. (B) Frozen solution sample of $[(P_3{}^B)^{57}Fe(NNMe_2)]^-$ (4 mM, 2-MeTHF), collected in a parallel 50 mT field. (C) Frozen solution sample of $[(P_3{}^B)^{57}Fe(NNMe_2)]^-$ (4 mM, 2-MeTHF), collected in a perpendicular 50 mT field. (D) Difference spectrum (B)−(C). See Table S.7 for fit parameters.

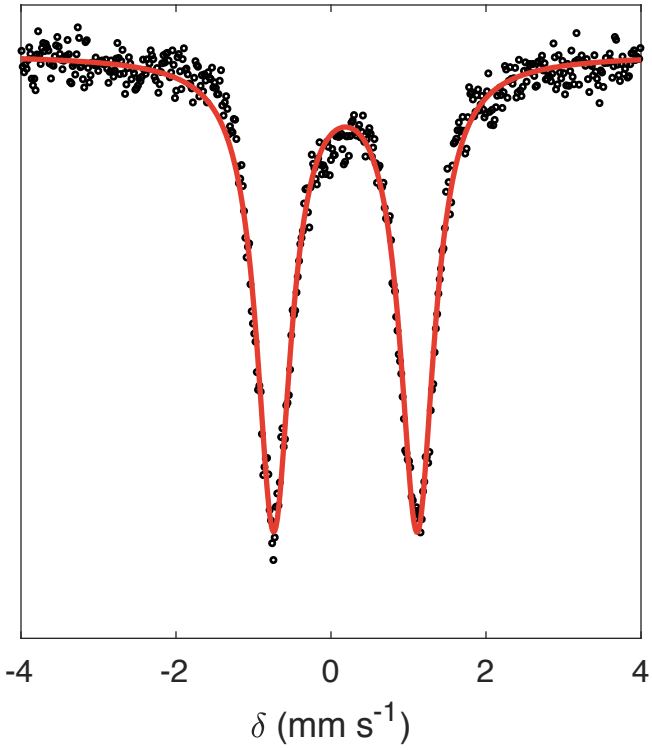

Figure S.33: 80 K Mössbauer spectrum of $(P_3{}^B)Fe(NN[Si]_2)$ (30 mM, 2-MeTHF, natural abundance) collected in the presence of a parallel 50 mT field. Raw data are shown as open circles, with a simulation shown as a solid red line. Simulation parameters: δ = 0.19 mm s^{-1}; $|\Delta E_Q|$ = 1.85 mm s^{-1}; FWHM = 0.54 mm s^{-1}.

S.12 Cyclic voltammograms

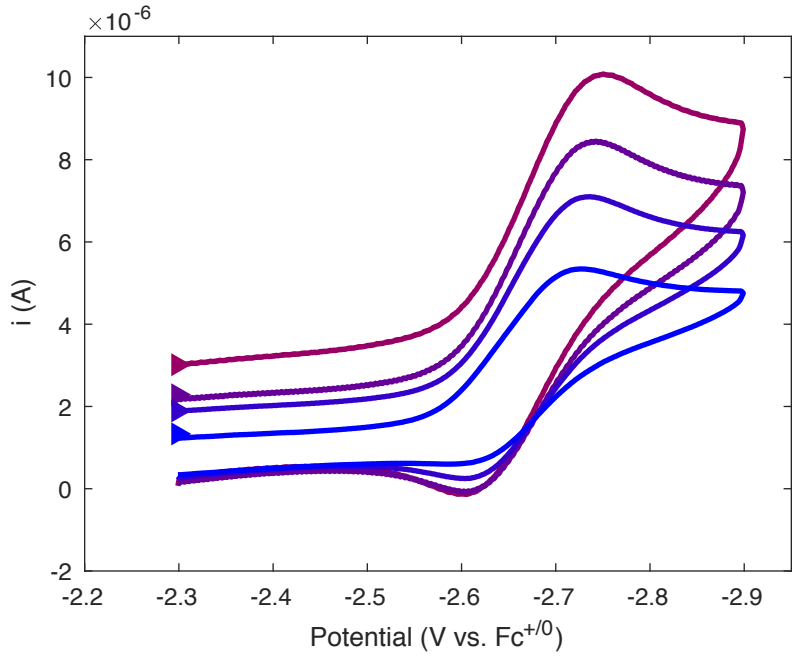

Figure S.34: Cyclic voltammograms of $(P_3{}^B)Fe(NNMe_2)$ (THF, 293 K). Each voltammogram was scanned cathodically through the $[(P_3{}^B)Fe(NNMe_2)]^{0/-}$ couple at ca. −2.6 V. The scan rate was increased in increments of 50 mV s^{-1} from 50 mV s^{-1} (blue) to 200 mV s^{-1} (magenta). The complete CV of $(P_3{}^B)Fe(NNMe_2)$ can be found in ref. [5].

S.13 Additional Supplementary Figures

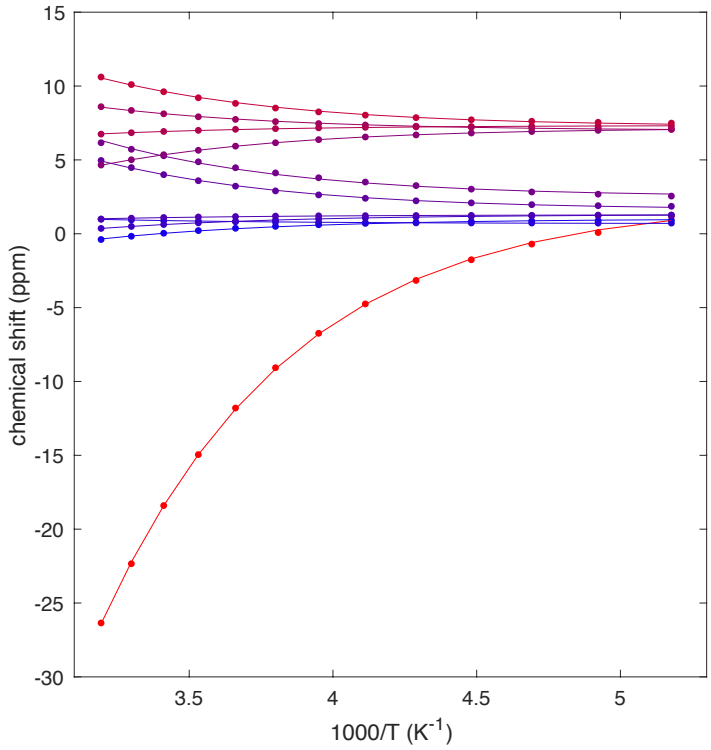

Figure S.35: Simulation of previously-reported variable temperature ^{1}H NMR spectra of (P_3^B)Fe(NNMe$_2$) (500 MHz, d_8-toluene).[5] Circles show the experimental data, while the solid lines show the least-squares fit to the model described in Table S.3. The red curve represents the N-CH$_3$ protons.

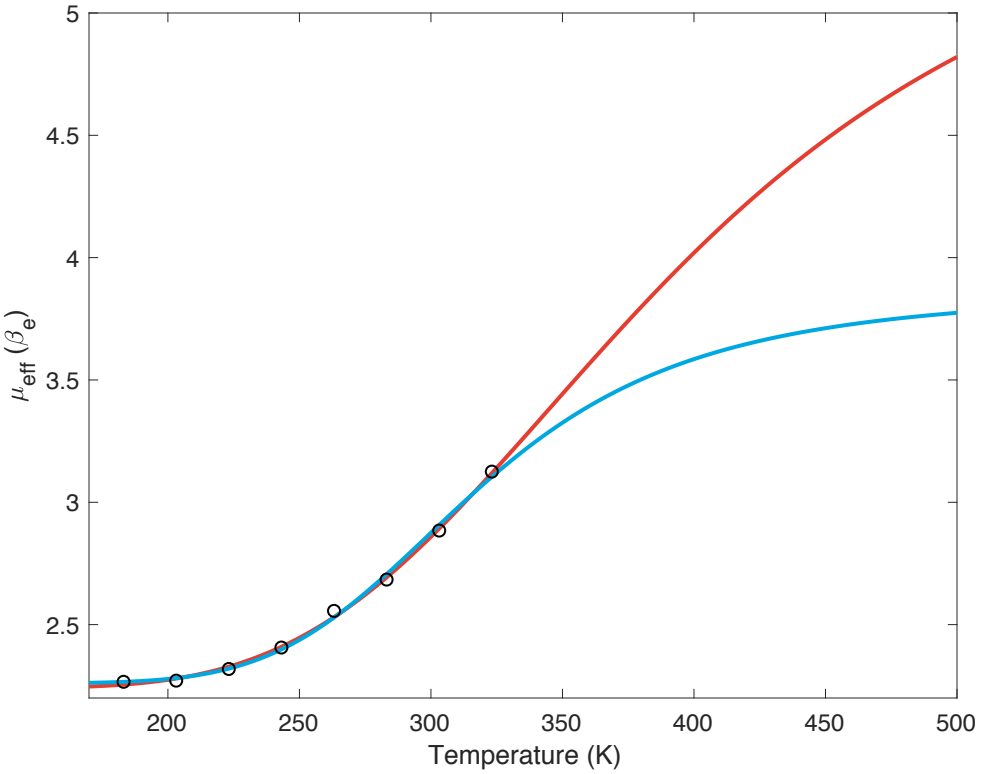

Figure S.36: Simulations of the variable-temperature magnetic susceptibility data of $[(P_3{}^B)Fe(NNMe_2)]^+$. The raw data are plotted as black circles, with simulations assuming the excited state multiplicity is $S = 3/2$ shown in blue, and assuming $S = 5/2$ shown in red. Simulation parameters are shown in Table S.4.

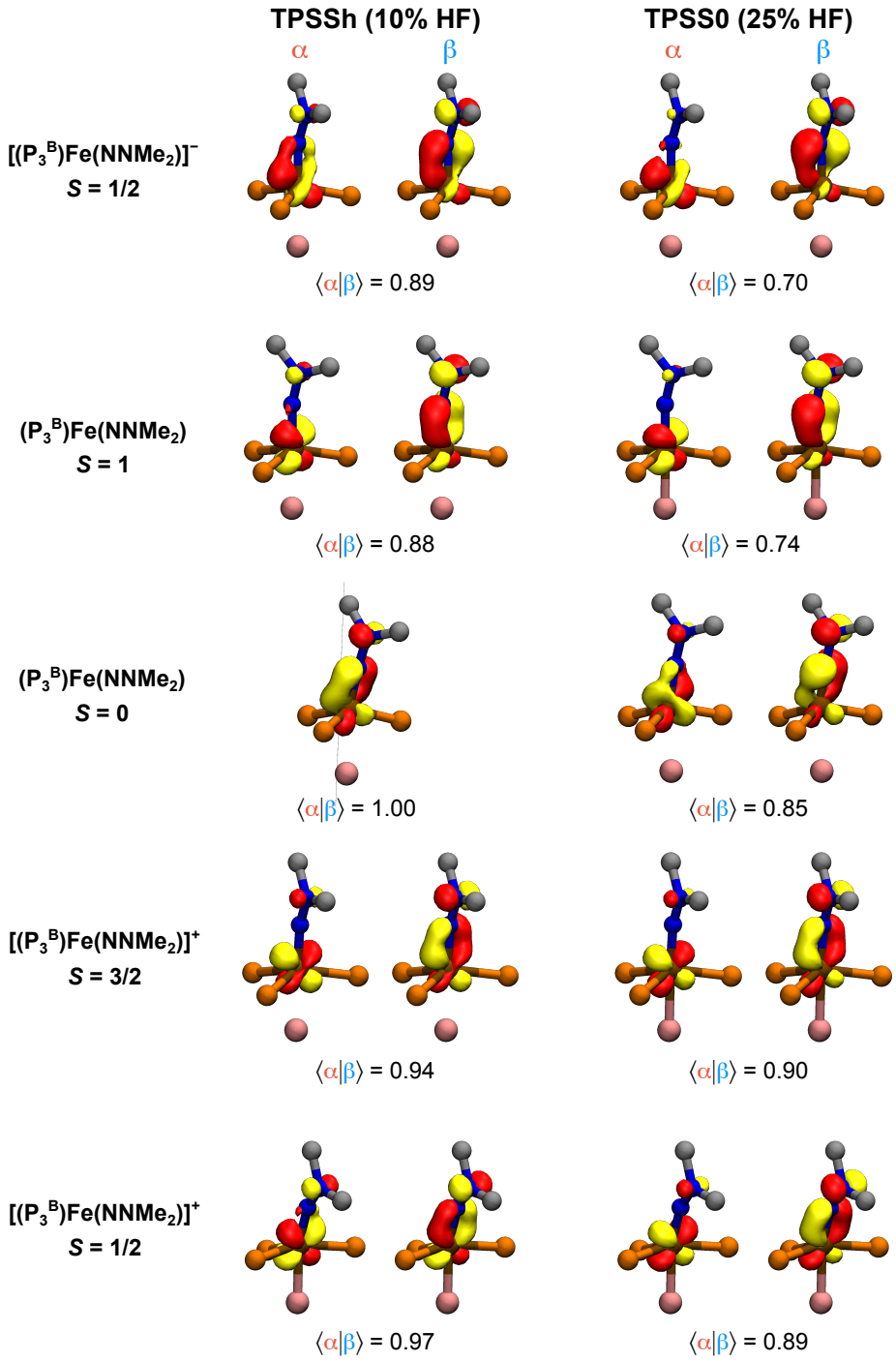

Figure S.37: Unrestricted corresponding orbitals for the $3d_{yz}/\pi^*_{NN}$ interaction from DFT calculations using either 10% (TPSSh) or 25% (TPSS0) exact exchange in the exchange-correlation functional. Orbitals from both the α and β manifold are plotted (isovalue = 0.075 a.u.), with overlap integrals indicated beneath.

S.14 Active Space Orbitals Used in Multireference Calculations

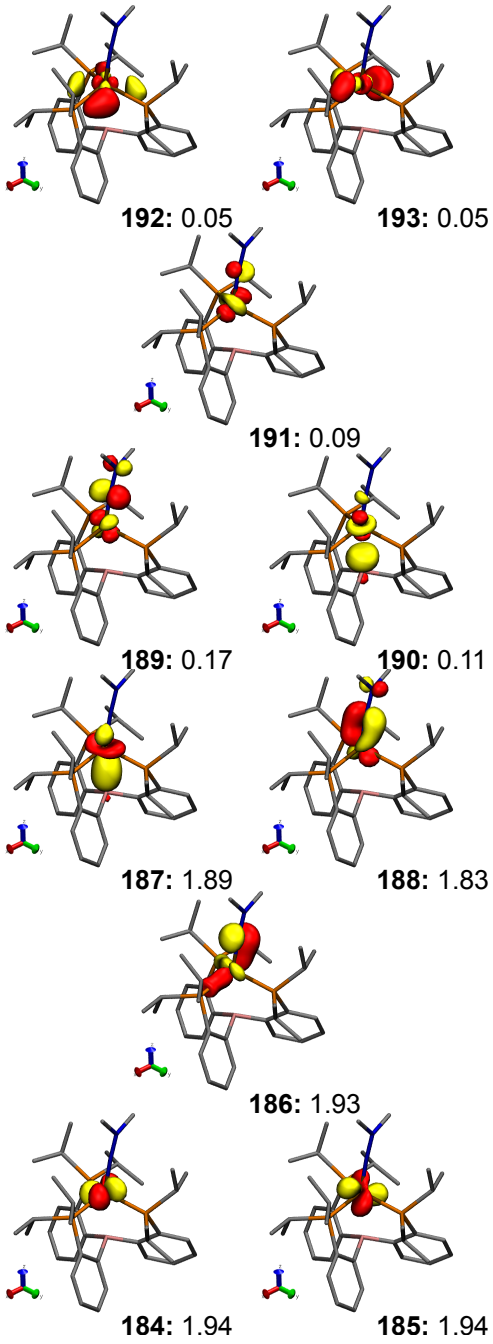

Figure S.38: CAS(10,10) active space natural orbitals from a state-specific calculation of $(P_3{}^B)Fe(NNMe_2)$ in the $^1\Gamma_{0,0}$ state. Orbital labels are given bold, with the corresponding occupation number in normal weight. All surfaces are rendered with an isovalue of 0.075 a.u..

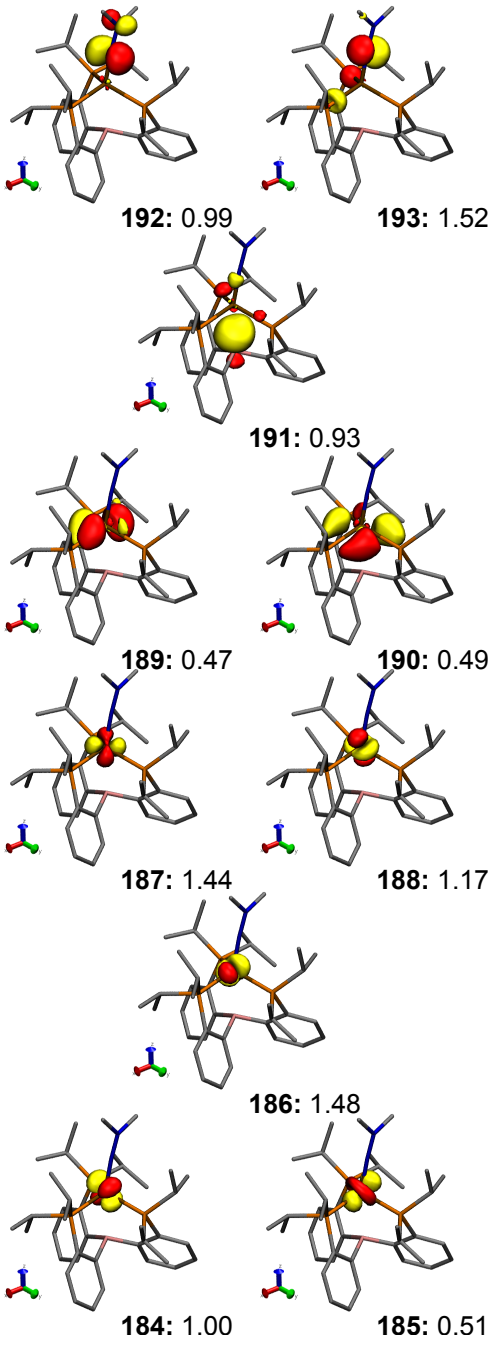

Figure S.39: CAS(10,10) active space orbitals from a state-specific calculation of $(P_3{}^B)Fe(NNMe_2)$ in the $^1\Gamma_{0,0}$ state obtained after Foster-Boys localization. Orbital labels are given bold, with the corresponding occupation number in normal weight. All surfaces are rendered with an isovalue of 0.075 a.u..

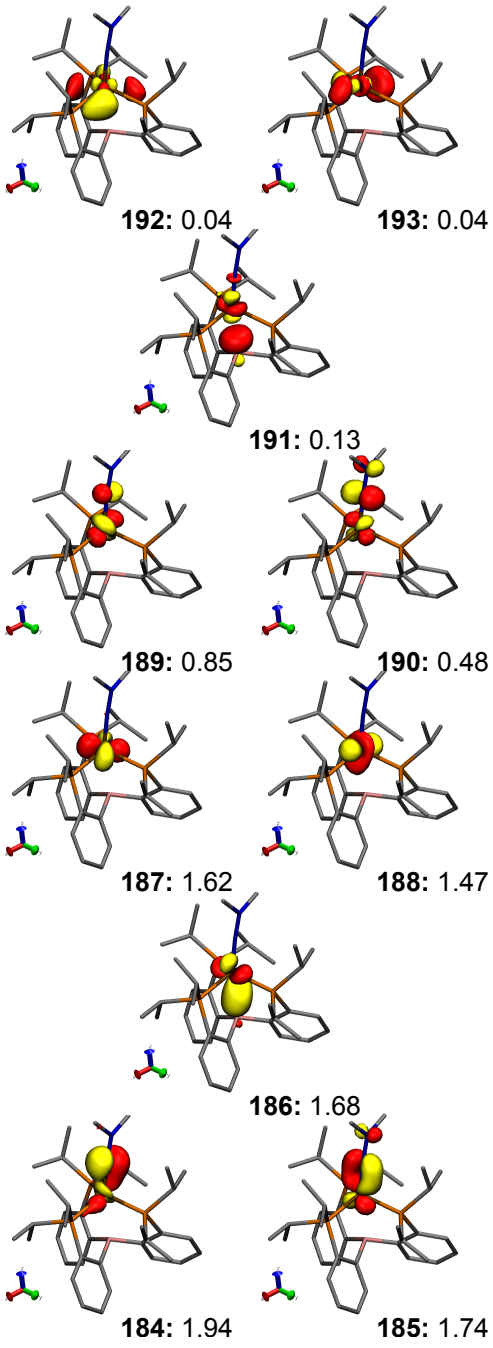

Figure S.40: CAS(10,10) active space natural orbitals from a state-averaged calculation of (P_3^B)Fe($NNMe_2$) over the 10 lowest-energy singlet states. Orbital labels are given bold, with the corresponding occupation number in normal weight. All surfaces are rendered with an isovalue of 0.075 a.u..

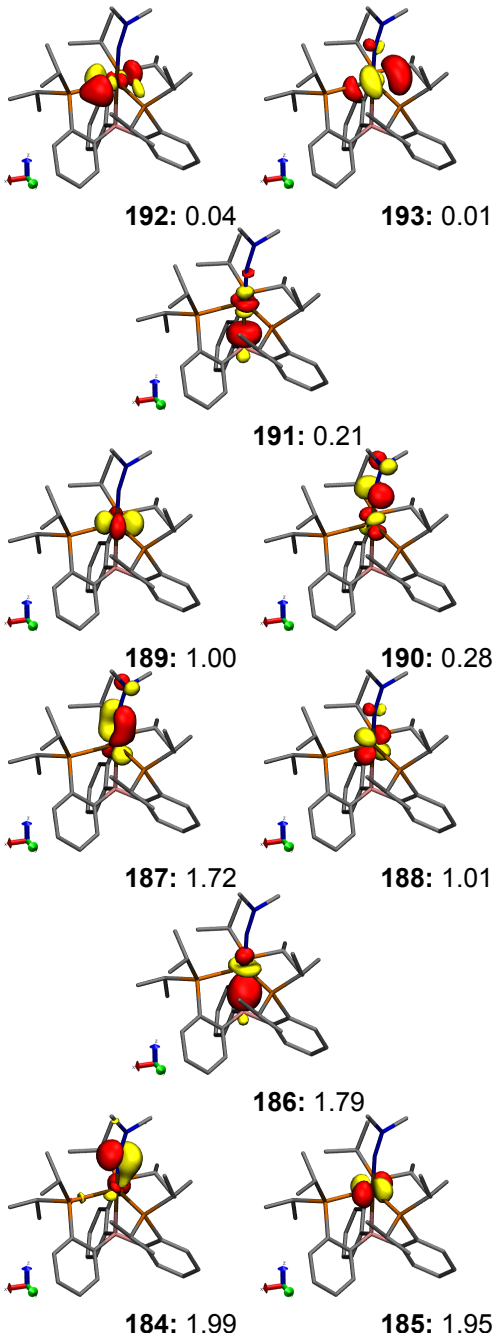

Figure S.41: CAS(10,10) active space natural orbitals from a state-specific calculation of $(P_3{}^B)Fe(NNMe_2)$ in the $^3\Gamma_{0,0}$ state, in the triplet geometry. Orbital labels are given bold, with the corresponding occupation number in normal weight. All surfaces are rendered with an isovalue of 0.075 a.u..

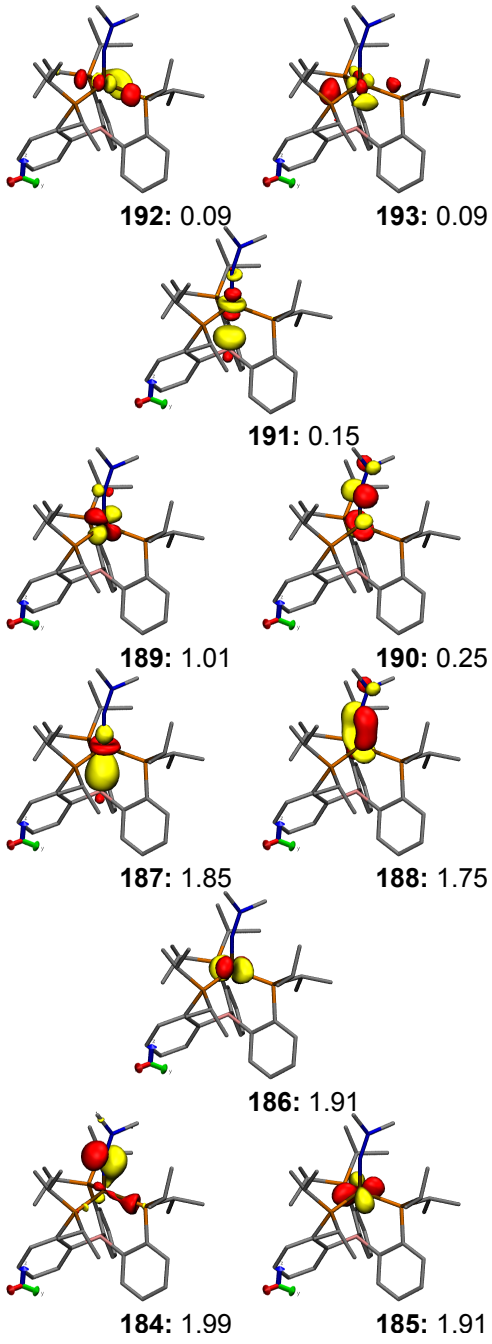

Figure S.42: CAS(11,10) active space natural orbitals from a state-specific calculation of $[(P_3{}^B)Fe(NNMe_2)]^-$ in the $^2\Gamma_{-,0}$ state. Orbital labels are given bold, with the corresponding occupation number in normal weight. All surfaces are rendered with an isovalue of 0.075 a.u..

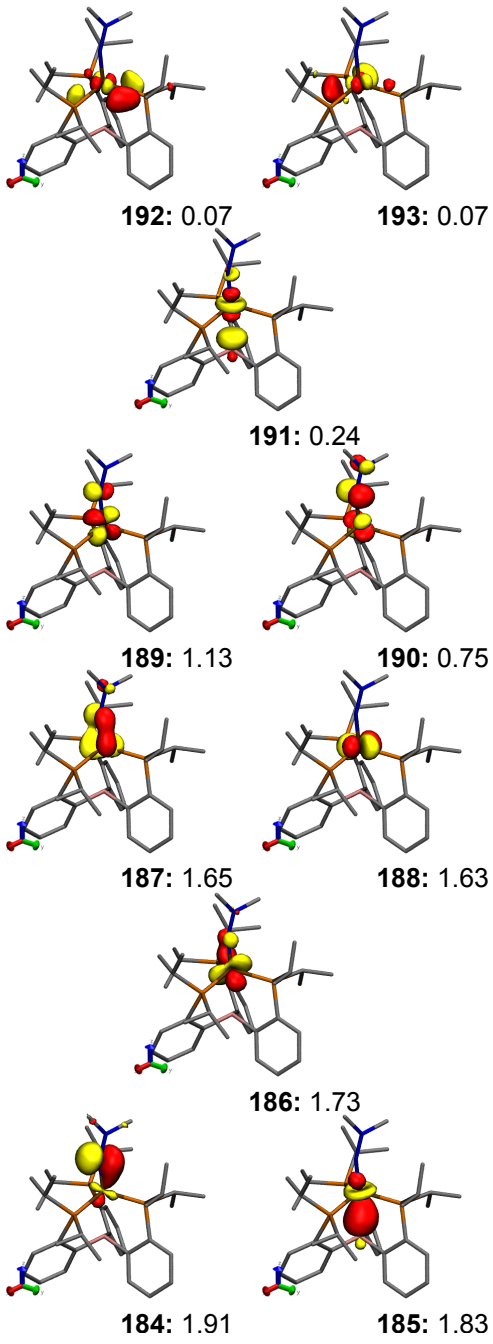

Figure S.43: CAS(11,10) active space natural orbitals from a state-averaged calculation of $[(P_3{}^B)Fe(NNMe_2)]^-$ over the 10 lowest-energy doublet states. Orbital labels are given bold, with the corresponding occupation number in normal weight. All surfaces are rendered with an isovalue of 0.075 a.u..

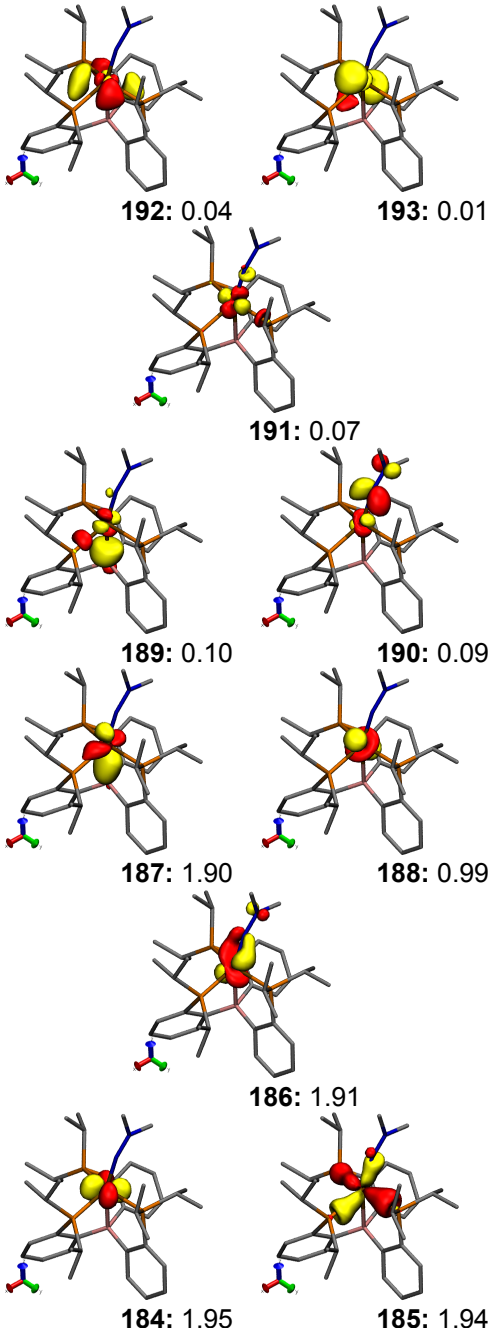

Figure S.44: CAS(9,10) active space natural orbitals from a state-specific calculation of $[(P_3{}^B)Fe(NNMe_2)]^+$ in the $^2\Gamma_{+,0}$ state. Orbital labels are given bold, with the corresponding occupation number in normal weight. All surfaces are rendered with an isovalue of 0.075 a.u.. Note that under the reduced symmetry of this redox state, π_N mixes significantly with a P-based group orbital, and we will refer to this orbital as σ_L. In addition, the Fe 3d orbitals of $3d_{xz}$ and $3d_{x^2-y^2}$ parentage mix significantly, and we will instead label these $3d_{\sigma,1}$ and $3d_{\sigma,2}$.

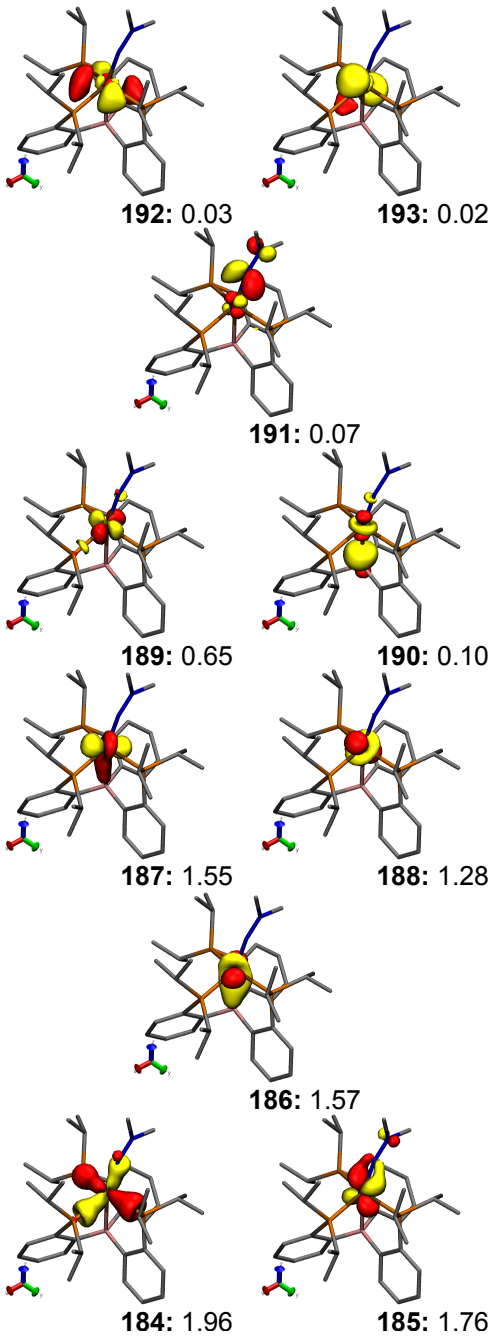

Figure S.45: CAS(9,10) active space natural orbitals from a state-averaged calculation of $[(P_3{}^B)Fe(NNMe_2)]^+$ over the 10 lowest-energy doublet states. Orbital labels are given bold, with the corresponding occupation number in normal weight. All surfaces are rendered with an isovalue of 0.075 a.u..

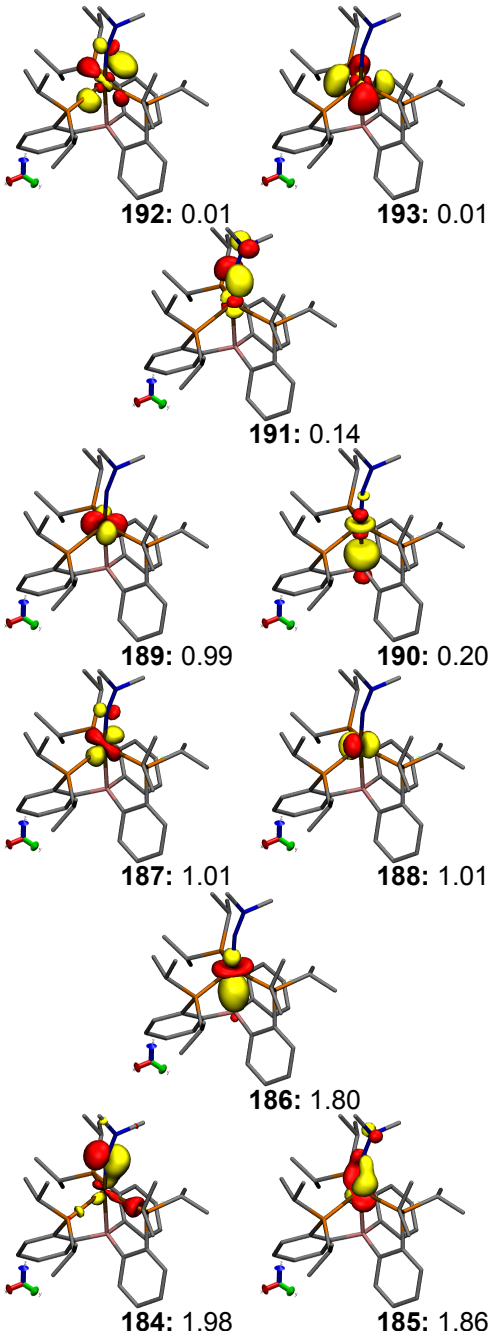

Figure S.46: CAS(9,10) active space natural orbitals from a state-specific calculation of $[(P_3{}^B)Fe(NNMe_2)]^+$ in the $^4\Gamma_{+,0}$ state, in the quartet geometry. Orbital labels are given bold, with the corresponding occupation number in normal weight. All surfaces are rendered with an isovalue of 0.075 a.u..

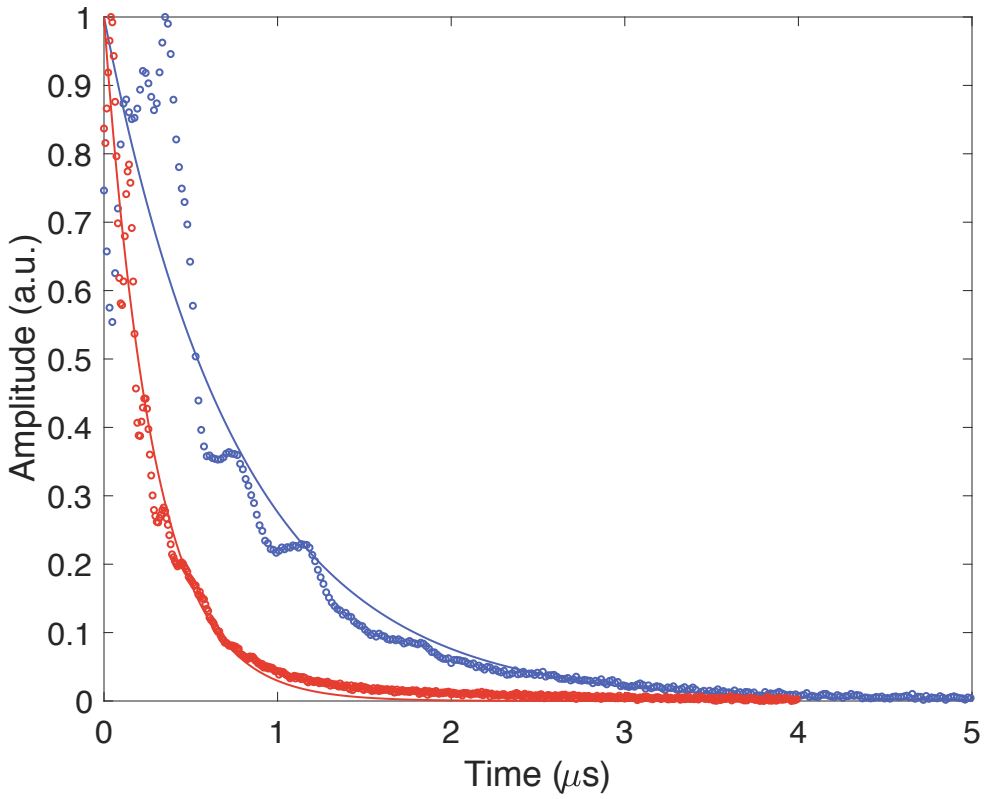

Figure S.47: Determination of the spin-spin relaxation time (T_2) from Hahn spin-echo decay measurements. Raw data are shown as open circles, with monoexponential fits ($A = A_0 \exp(-t/T_2)$) as solid lines. Data for [(P_3^B)Fe($NNMe_2$)][BAr^F_4] (2 mM, 2-MeTHF, 12 K) are shown in blue, while data for [(P_3^B)Fe(NAd)][BAr^F_4] (2 mM, 2-MeTHF, 12 K) are shown in red.

S.15 Supplementary Tables

Table S.1: Crystal data and structure refinement for $[(P_3{}^B)Fe(NNMe_2)][BAr^F{}_4]\cdot Et_2O$

Empirical formula	$C_{74}H_{82}B_2F_{24}FeN_2OP_3$
Formula weight	1641.79
Temperature (K)	100(2)
Crystal system	Orthorhombic
Space group	$Pca2_1$
a (Å)	21.094(3)
b (Å)	19.460(3)
c (Å)	18.649(3)
α (°)	90
β (°)	90
γ (°)	90
Volume (Å^3)	7655.4(19)
Z	4
ρ_{calc} (g cm^{-3})	1.424
μ (mm^{-1})	0.363
F(000)	3380
Crystal size (mm^3)	$0.1 \times 0.1 \times 0.1$
Radiation	Mo K_α (λ = 0.71073 Å)
2θ range for data collection (°)	2.196 to 30.574
Index ranges	$-30 \leq h \leq 30, -27 \leq k \leq 27, -26 \leq l \leq 26$
Reflections collected	259650
Independent reflections	23383 (R_{int} = 0.0707)
Data/restraints/parameters	23383 / 1 / 980
Goodness-of-fit on F^2	1.034
Final R indexes (I $\geq 2\sigma$(I))	R_1 = 0.0451, wR_2 = 0.1114
Final R indexes (all data)	R_1 = 0.0620, wR_2 = 0.1209
Largest diff. peak/hole (e Å^{-3})	1.827 and −0.462

Table S.2: Crystal data and structure refinement for [K(benzo-15-c-5)$_2$][(P_3^B)Fe(NNMe$_2$)]·4 (2-MeTHF)

Empirical formula	$C_{86}H_{140}BFeKN_2O_{14}P_3$
Formula weight	1624.66
Temperature (K)	100(2)
Crystal system	Triclinic
Space group	P-1
a (Å)	13.2390(5)
b (Å)	18.3254(7)
c (Å)	19.9275(8)
α (°)	87.899(3)
β (°)	75.367(2)
γ (°)	69.520(2)
Volume (Å^3)	4375.0(3)
Z	2
ρ_{calc} (g cm^{-3})	1.233
μ (mm^{-1})	2.812
F(000)	1754
Crystal size (mm^3)	$0.1 \times 0.1 \times 0.1$
Radiation	Cu K$_\alpha$ (λ = 1.54178 Å)
2θ range for data collection (°)	2.578 to 61.165
Index ranges	$-15 \leq h \leq 13, -20 \leq k \leq 20, -22 \leq l \leq 21$
Reflections collected	53935
Independent reflections	12204 (R_{int} = 0.0915)
Data/restraints/parameters	12204 / 577 / 1097
Goodness-of-fit on F^2	1.101
Final R indexes (I $\geq 2\sigma$(I))	R_1 = 0.0884, wR_2 = 0.2176
Final R indexes (all data)	R_1 = 0.1344, wR_2 = 0.2390
Largest diff. peak/hole (e Å^{-3})	0.693 and −0.524

Table S.3: Best fit parameters for the simulation of the VT NMR data of $(P_3{}^BB)Fe(NNMe_2)$ shown in Figure S.35. The following model was used,

$$\delta_{\text{obs}} = \delta_d + 10^{12} \cdot a_{\text{iso}} \cdot \frac{2hg_e\beta_e}{g_N\beta_N k_B T} \frac{1}{3+\exp\left(\frac{\Delta E}{RT}\right)}$$

For a derivation, see the supplementary discussion above. The 95% confidence interval is given in brackets below each parameter.

Resonance	δ_d (ppm)	a_{iso} (MHz)	ΔE (kcal mol^{-1})
N-CH_3	2.15 [2.06, 2.25]	−48.4 [−50.5, −46.3]	
*i*Pr-CH_3	1.00 [0.96, 1.06]	−2.3 [−2.5, −2.1]	
*i*Pr-CH_3	0.69 [0.64, 0.74]	0.47 [0.32, 0.64]	
*i*Pr-CH_3	1.30 [1.26, 1.35]	−1.6 [−1.8, −1.4]	
*i*Pr-CH_3	1.29 [1.24, 1.33]	−0.45 [−0.6, −0.3]	
*i*Pr-CH	1.64 [1.60, 1.69]	5.6 [5.3, 5.9]	
*i*Pr-CH	2.52 [2.47, 2.57]	6.4 [6.1, 6.7]	
Ar-CH	7.16 [7.12, 7.21]	−4.3 [−4.5, −4.0]	
Ar-CH	6.99 [6.94, 7.04]	2.7 [2.5, 2.9]	
Ar-CH	7.33 [7.29, 7.39]	−1.0 [−1.1, −0.8]	
Ar-CH	7.27 [7.23, 7.32]	5.5 [5.3, 5.8]	
			3.62 [3.59, 3.65]

Table S.4: Best fit parameters for the simulation of the VT magnetic susceptibility data of $[(P_3{}^B)Fe(NNMe_2)]^+$ shown in Figure S.36. The 95% confidence interval is given in brackets below each parameter.

g_2 ($\mu_2[\beta_e]$)	μ_1	ΔH (kcal mol^{-1})	ΔS (cal mol^{-1} K^{-1})	RMSE
4 (3.87)	2.26 [2.22, 2.30]	4.79 [4.03, 5.55]	13.6 [11.1, 16.1]	0.02
6 (5.92)	2.24 [2.21, 2.27]	3.65 [3.22, 4.09]	6.8 [5.5, 8.2]	0.02

Table S.5: Fit parameters for the Gaussian spectral deconvolution of the UV-vis spectrum of $(P_3{}^B)Fe(NNMe_2)$, shown in Figure S.30. The 95% confidence interval is given below each parameter in brackets.

Component	f	$\bar{\nu}_0$ (cm^{-1})	$\sigma_{1/2}$ (cm^{-1})
1	0.0016 [0.0009, 0.0023]	12 260 [12 140, 12 380]	2 193 [1 988, 2 398]
2	0.0034 [0.0022, 0.0045]	14 580 [14 420, 14 740]	3 449 [2 457, 4 441]
3	0.0084 [0.0079, 0.0090]	17 830 [17 770, 17 890]	2 864 [2 786, 2 942]
4 (baseline)	0.21 [0.20, 0.22]	28 170 [28 030, 28 310]	9 159 [9 027, 9 292]

Table S.6: Mössbauer simulation parameters for the spectra shown in Figure S.31

Component	**1** ([(**P**$_3^{\mathbf{B}}$)**Fe(NNMe$_2$)**]$^+$)
g_3 (= g_{max})	2.192
g_2 (= g_{mid})	2.089
g_1 (= g_{min})	2.005
δ (mm s^{-1})	0.30
$\lvert\Delta E_Q\rvert$ (mm s^{-1})	1.13
η	0
A_3 (MHz)	0
A_2 (MHz)	10.7
A_1 (MHz)	24.8
β (HFC frame)	23.5°
FWHM (mm s^{-1})	0.38
Relative area	1.02

Table S.7: Mössbauer simulation parameters for the spectra shown in Figure S.32

Component	**1** ([(**P**$_3^{\mathbf{B}}$)**Fe(NNMe$_2$)**]$^-$)	**2**	**3**
g_3 (= g_{max})	2.068	–	–
g_2 (= g_{mid})	2.041	–	–
g_1 (= g_{min})	2.006	–	–
δ (mm s^{-1})	0.39	0.43	0.90
$\lvert\Delta E_Q\rvert$ (mm s^{-1})	1.20	1.13	2.01
η	0.8	–	–
A_3 (MHz)	53.9	–	–
A_2 (MHz)	15.2	–	–
A_1 (MHz)	18.1	–	–
FWHM (mm s^{-1})	0.44	1.03	0.41
Relative area	0.74	0.35	0.04

Table S.8: Fit parameters for T_2 measurments presented in Figure S.47. The 95% confidence interval is given below each parameter.

Compound	T_2 (ns)
$[(P_3{}^B)Fe(NNMe_2)][BAr^F{}_4]$	777 [742, 816]
$[(P_3{}^B)Fe(NAd)][BAr^F{}_4]$	284 [276, 292]

Table S.9: Comparison of experimental (XRD) and gas-phase optimized core structures of $[(P_3{}^B)Fe(NNMe_2)]^{+/0/-}$.

	$[(P_3{}^B)Fe(NNMe_2)]^+$		$(P_3{}^B)Fe(NNMe_2)$		$[(P_3{}^B)Fe(NNMe_2)]^-$	
	XRD	TPSS	XRD	TPSS	XRD	TPSS
d(Fe–N_α) (Å)	1.738(3)	1.727	1.680(2)	1.667	1.771(7)	1.756
d(Fe–B) (Å)	2.315(3)	2.313	2.534(3)	2.498	2.472(9)	2.447
d(Fe–P1) (Å)	2.2816(9)	2.294	2.2390(8)	2.238	2.280(2)	2.300
d(Fe–P2) (Å)	2.3168(9)	2.356	2.2670(8)	2.298	2.243(2)	2.236
d(Fe–P3) (Å)	2.2626(9)	2.290	2.2469(9)	2.220	2.233(2)	2.234
d(N_α–N_β) (Å)	1.252(4)	1.268	1.293(3)	1.303	1.27(1)	1.303
∠(P2FeP3) (°)	154.93(4)	154.33	125.03(3)	128.75	118.13(9)	118.60
∠(P1FeP3) (°)	96.10(3)	96.06	109.88(4)	108.52	112.22(9)	110.97
∠(P1FeP2) (°)	100.31(3)	100.08	104.28(3)	103.29	115.00(9)	115.88
∠(Fe$N_\alpha N_\beta$) (°)	159.7(3)	159.68	176.1(1)	174.34	161.6(6)	156.11
∠(BFeN_α) (°)	157.36(1)	157.94	168.91(1)	166.08	177.9(3)	175.95
Mean Error (%)[a]	–	0.589	–	1.22	–	1.13

[a]The mean error is calculated as the mean value of $|p_{exp} - p_{calc}|/p_{exp}$ for each parameter p in the table, multiplied by 100.

Table S.10: Spin state energetics for $[(P_3{}^B)Fe(NNMe_2)]^+$ from geometry optimizations using the TPSS functional

S	ΔH (kcal mol^{-1})	ΔS (cal mol^{-1} K^{-1})
1/2	0	0
3/2	14.5	10.5
5/2	40.7	11.8

Table S.11: Adiabatic doublet–quartet gap of $[(P_3{}^B)Fe(NNMe_2)]^+$ as a function of % HF exchange

% HF (Functional)	$\Delta E(^4\Gamma_{+,0} - {}^2\Gamma_{+,0})$ (kcal mol^{-1})
0 (TPSS)	15.4
10 (TPSSh)	8.7
25 (TPSS0)	−1.8

Table S.12: Comparison of experimental and DFT-predicted EPR properties of free *N*,*N*-dimethylhydrazyl radicals.

	$[H_2NNMe_2)]^+$		$HNNMe_2$		$[NNMe_2]^-$	
	Expt.[25,27]	DFT	Expt.[26,27]	DFT	DFT (ground state)	DFT (planar)
g_{iso}	2.0035	2.0034	2.0038	2.0037	2.0043	2.0042
$a_{iso}(^{14}N_\alpha)$ (MHz)	26.8	26.6	26.9	25.7	22.0	23.1
$a_{iso}(^{14}N_\beta)$ (MHz)	44.4	40.1	32.2	32.4	26.2	6.9
$a_{iso}(^{1}H_\alpha)$ (MHz)[a]	19.4	−6.6	38.4	−29.8	–	–
$a_{iso}(^{1}H_\gamma)$ (MHz)[b]	39.8	43.3	19.4	18.2	6.3	10.7
$a_{iso}(^{13}C)$ (MHz)	n.d.	−16.6	n.d.	−3.6/5.9	37.1	−21.6

[a]The discrepancy in the experimental and DFT-calculated values of $a_{iso}(^1H_\alpha)$ is likely due to the omission of environmental factors such as hydrogen bonding and other non-covalent interactions.
[b]In the DFT-predicted values, $a_{iso}(^1H_\gamma)$ was averaged over all protons of the N-CH_3 group.

Table S.13: DFT-predicted HFC constants of free $[NNMe_2]^-$.

	$[NNMe_2]^-$	
	DFT (ground state)	DFT (planar)
$A_1(^{14}N_\alpha)$ (MHz)	−8.2	−8.3
$A_2(^{14}N_\alpha)$ (MHz)	−11.7	−12.2
$A_3(^{14}N_\alpha)$ (MHz)	86.0	89.7
$a_{iso}(^{14}N_\alpha)$ (MHz)	22.0	23.1
$t(^{14}N_\alpha)$ (MHz)	32.0	33.3
$\delta_{HFC}(^{14}N_\alpha)$	0.06	0.06
$A_1(^{14}N_\beta)$ (MHz)	18.2	−3.1
$A_2(^{14}N_\beta)$ (MHz)	19.5	−5.1
$A_3(^{14}N_\beta)$ (MHz)	40.9	28.9
$a_{iso}(^{14}N_\beta)$ (MHz)	26.2	6.9
$t(^{14}N_\beta)$ (MHz)	7.3	11.0
$\delta_{HFC}(^{14}N_\beta)$	0.09	0.09
$a_{iso}(^{13}C)$ (MHz)	37.1	−21.6

Table S.14: Wavefunction composition (in terms of CI coefficients) from a state-specific CASSCF(10,10) calculation on the $^1\Gamma_{0,0}$ state of $(P_3{}^B)Fe(NNMe_2)$, in terms of the natural orbitals shown in Figure S.38.

Weight	Configuration									
	184	185	186	187	188	189	190	191	192	193
	$3d_{x^2-y^2}$	$3d_{xy}$	$3d_{xz} + \pi_N$	$3d_{z^2} + 2p_z$	$3d_{yz} + \pi^*_{NN}$	$3d_{yz} - \pi^*_{NN}$	$3d_{z^2} - 2p_z$	$3d_{xz} - \pi_N$	$3d'_1$	$3d'_2$
0.79807	2	2	2	2	2	0	0	0	0	0
0.04513	2	2	2	2	0	2	0	0	0	0
0.02251	2	2	2	0	2	0	2	0	0	0
0.01930	2	2	1	2	1	1	0	1	0	0
0.00851	2	2	2	1	1	1	1	0	0	0
0.00633	2	2	0	2	2	0	0	2	0	0
0.00468	2	2	1	1	2	0	1	1	0	0
0.00454	1	2	2	1	2	0	1	0	0	1
0.00438	2	1	2	1	2	0	1	0	1	0
0.00376	1	1	2	2	2	0	0	0	1	1
0.00371	2	1	2	1	2	0	1	0	0	1
0.00308	1	2	2	1	2	0	1	0	1	0
0.00270	2	0	2	2	2	0	0	2	0	0
0.00254	2	1	2	2	1	1	0	0	1	0

Table S.15: Wavefunction compositions (in terms of CI coefficients) from a SA-CASSCF(10,10) calculation on the 10 lowest-energy singlet states of $(P_3{}^B)Fe(NNMe_2)$, in terms of the natural orbitals shown in Figure S.40. Only the first 5 states are listed, with only the largest 4 configurations given.

State	Weight	Configuration									
		184	185	186	187	188	189	190	191	192	193
		$3d_{xz} + \pi_N$	$3d_{yz} + \pi^*_{NN}$	$3d_{z^2} + 2p_z$	$3d_{xy}$	$3d_{x^2-y^2}$	$3d_{xz} - \pi_N$	$3d_{yz} - \pi^*_{NN}$	$3d_{z^2} - 2p_z$	$3d'_1$	$3d'_2$
$^1\Gamma_{0,0}$	0.73869	2	2	2	2	2	0	0	0	0	0
	0.03858	2	0	2	2	2	0	2	0	0	0
	0.02466	2	2	0	2	2	0	0	2	0	0
	0.02102	1	1	2	2	2	1	1	0	0	0
$^1\Gamma_{0,1}$	0.69366	2	2	2	2	1	1	0	0	0	0
	0.04856	2	2	1	2	2	1	0	0	0	0
	0.04618	2	0	2	2	1	1	2	0	0	0
	0.02955	2	2	0	2	2	1	0	2	0	0
$^1\Gamma_{0,2}$	0.61429	2	2	2	1	2	1	0	0	0	0
	0.06375	2	2	2	2	1	0	1	0	0	0
	0.06016	2	2	2	1	2	0	1	0	0	0
	0.04594	2	0	2	1	2	1	2	0	0	0
$^1\Gamma_{0,3}$	0.27517	2	2	2	1	2	0	1	0	0	0
	0.16222	2	2	1	2	2	1	0	0	0	0
	0.10756	2	2	1	2	2	0	1	0	0	0
	0.08747	2	2	2	1	2	1	0	0	0	0
$^1\Gamma_{0,4}$	0.24561	2	2	1	2	2	0	1	0	0	0
	0.23534	2	2	2	2	1	0	1	0	0	0
	0.11832	2	2	2	1	2	0	1	0	0	0
	0.11374	2	2	1	2	2	1	0	0	0	0

Table S.16: NEVPT2 energies from a SA-CASSCF(10,10) calculation on the 10 lowest-energy singlet states of $(P_3{}^B)Fe(NNMe_2)$. Only the first 5 states are listed.

State	Energy (cm^{-1})	
	Expt.	NEVPT2
$^1\Gamma_{0,0}$	0	0
$^1\Gamma_{0,1}$	12 260	13 595.8
$^1\Gamma_{0,2}$	14 580	14915.2
$^1\Gamma_{0,3}$	17 830	17 382.2
$^1\Gamma_{0,4}$		19 278.3

Table S.17: Wavefunction composition (in terms of CI coefficients) from a state-specific CASSCF(10,10) calculation on the $^3\Gamma_{0,0}$ state of $(P_3{}^B)Fe(NNMe_2)$, in terms of the natural orbitals shown in Figure S.41.

Weight	Configuration									
	184	185	186	187	188	189	190	191	192	193
	π_N	$3d_{xy}$	$3d_{z^2} + 2p_z$	$3d_{yz} + \pi^*_{NN}$	$3d_{xz}$	$3d_{x^2-y^2}$	$3d_{yz} - \pi^*_{NN}$	$3d_{z^2} - 2p_z$	$3d'_1$	$3d'_2$
0.69631	2	2	2	2	1	1	0	0	0	0
0.06830	2	2	2	0	1	1	2	0	0	0
0.06280	2	2	2	1	1	1	1	0	0	0
0.04748	2	2	0	2	1	1	0	2	0	0
0.03549	2	2	1	2	1	1	0	1	0	0
0.01548	2	2	1	1	1	1	1	1	0	0
0.00750	2	1	1	2	1	1	0	1	1	0
0.00732	2	2	0	0	1	1	2	2	0	0
0.00603	2	1	2	1	1	1	1	0	1	0
0.00527	2	2	0	1	1	1	1	2	0	0
0.00446	2	2	1	0	1	1	2	1	0	0
0.00445	1	2	2	1	2	1	1	0	0	0
0.00418	2	0	2	2	1	1	0	0	2	0

Table S.18: Wavefunction composition (in terms of CI coefficients) from a state-specific CASSCF(11,10) calculation on the $^2\Gamma_{-,0}$ state of $[(P_3{}^B)Fe(NNMe_2)]^-$, in terms of the natural orbitals shown in Figure S.42.

Weight	Configuration									
	184	185	186	187	188	189	190	191	192	193
	π_N	$3d_{xy}$	$3d_{x^2-y^2}$	$3d_{z^2} + 2p_z$	$3d_{yz} + \pi^*_{NN}$	$3d_{xz}$	$3d_{yz} - \pi^*_{NN}$	$3d_{z^2} - 2p_z$	$3d'_1$	$3d'_2$
0.71930	2	2	2	2	2	1	0	0	0	0
0.06432	2	2	2	2	0	1	2	0	0	0
0.03124	2	2	2	2	1	1	1	0	0	0
0.02818	2	2	2	0	2	1	0	2	0	0
0.01185	2	2	1	1	2	1	0	1	1	0
0.01183	2	1	1	2	2	1	0	0	1	1
0.01154	2	1	2	1	2	1	0	1	0	1
0.00979	2	2	2	1	1	1	1	1	0	0
0.00966	2	2	2	1	2	1	0	1	0	0
0.00885	2	2	0	2	2	1	0	0	2	0
0.00842	2	2	1	2	1	1	1	0	1	0
0.00829	2	0	2	2	2	1	0	0	0	2
0.00778	2	1	2	2	1	1	1	0	0	1
0.00451	1	2	2	2	1	2	1	0	0	0
0.00409	2	2	1	2	2	1	0	0	1	0
0.00347	2	2	2	0	0	1	2	2	0	0
0.00329	2	1	2	2	2	1	0	0	0	1

Table S.19: Wavefunction composition (in terms of CI coefficients) from a state-specific CASSCF(9,10) calculation on the $^2\Gamma_{+,0}$ state of $[(P_3{}^B)Fe(NNMe_2)]^+$, in terms of the natural orbitals shown in Figure S.44.

	Configuration									
Weight	184	185	186	187	188	189	190	191	192	193
	$3d_{xy}$	$3d_{\sigma,1} + \sigma_L$	$3d_{yz} + \pi^*_{NN}$	$3d_{z^2} + 2p_z$	$3d_{\sigma,2}$	$3d_{z^2} - 2p_z$	$3d_{yz} - \pi^*_{NN}$	$3d_{\sigma,1} - \sigma_L$	$3d'_1$	$3d'_2$
0.84932	2	2	2	2	1	0	0	0	0	0
0.02116	2	2	2	0	1	2	0	0	0	0
0.01430	2	2	0	2	1	0	2	0	0	0
0.01321	2	1	1	2	1	0	1	1	0	0
0.01147	2	2	1	1	1	1	1	0	0	0
0.01072	2	1	2	1	1	1	0	1	0	0
0.00722	1	2	2	1	1	1	0	0	1	0
0.00656	1	2	1	2	1	0	1	0	1	0
0.00566	1	1	2	2	1	0	0	1	1	0
0.00541	2	2	1	2	1	0	1	0	0	0
0.00468	2	0	2	2	1	0	0	2	0	0
0.00403	2	2	2	1	1	1	0	0	0	0
0.00397	2	1	2	2	1	0	0	1	0	0
0.00320	0	2	2	2	1	0	0	0	2	0
0.00287	2	2	2	1	0	1	0	0	0	1

Table S.20: Wavefunction composition (in terms of CI coefficients) from a state-specific CASSCF(9,10) calculation on the $^4\Gamma_{+,0}$ state of $[(P_3{}^B)Fe(NNMe_2)]^+$, in terms of the natural orbitals shown in Figure S.46.

Weight	Configuration									
	184	185	186	187	188	189	190	191	192	193
	π_N	$3d_{yz} + \pi^*_{NN}$	$3d_{z^2} + 2p_z$	$3d_{xz}$	$3d_{x^2-y^2}$	$3d_{xy}$	$3d_{z^2} - 2p_z$	$3d_{yz} - \pi^*_{NN}$	$3d'_1$	$3d'_2$
0.77474	2	2	2	1	1	1	0	0	0	0
0.05316	2	2	1	1	1	1	1	0	0	0
0.04719	2	2	0	1	1	1	2	0	0	0
0.03563	2	1	2	1	1	1	0	1	0	0
0.02456	2	0	2	1	1	1	0	2	0	0
0.01859	2	1	1	1	1	1	1	1	0	0
0.00827	1	1	2	2	1	1	0	1	0	0
0.00266	2	1	0	1	1	1	2	1	0	0
0.00261	2	0	1	1	1	1	1	2	0	0

Table S.21: NEVPT2 energies of the doublet excited states of $[(P_3{}^B)Fe(NNMe_2)]^-$, and their contributions to the g-shifts from CASCI.[a]

State	NEVPT2 Energy (cm^{-1})	Δg_1	Δg_2	Δg_3
$^2\Gamma_{-,0}$	0	0	0	0
$^2\Gamma_{-,1}$	10654.9	−0.0129697	−0.0012106	-0.0045002
$^2\Gamma_{-,2}$	11227.1	0.0024437	0.0006445	0.0598511
$^2\Gamma_{-,3}$	11299.4	0.0003412	0.0329346	0.0002667
$^2\Gamma_{-,4}$	16337.2	0.0219329	0.0003345	0.0073102
$^2\Gamma_{-,5}$	18057.5	0.0005674	0.0110975	0.0000371
$^2\Gamma_{-,6}$	21860.3	−0.0004066	0.0006536	−0.0003774
$^2\Gamma_{-,7}$	22084.9	−0.0050565	−0.0078387	−0.0074183
$^2\Gamma_{-,8}$	22123.6	−0.0068105	−0.0000398	−0.0000452
$^2\Gamma_{-,9}$	24520.3	−0.0004940	−0.0001497	−0.0000481

[a]Using a SA-CASSCF(11,10) reference averaging over the first 10 doublet states.

Table S.22: NEVPT2 energies of the doublet excited states of $[(P_3{}^B)Fe(NNMe_2)]^+$, and their contributions to the g-shifts from CASCI.[a]

State	NEVPT2 Energy (cm^{-1})	Δg_1	Δg_2	Δg_3
$^2\Gamma_{+,0}$	0	0	0	0
$^2\Gamma_{+,1}$	7082.5	−0.0001191	0.0002972	0.2501078
$^2\Gamma_{+,2}$	11972.5	0.0000317	0.1221519	0.0008200
$^2\Gamma_{+,3}$	18195.9	0.0006481	0.0002731	0.0018648
$^2\Gamma_{+,4}$	20516.0	−0.0004503	−0.0013382	−0.0036448
$^2\Gamma_{+,5}$	20751.1	0.0048607	−0.0053158	0.0001804
$^2\Gamma_{+,6}$	23678.4	0.0028159	−0.0008443	−0.0019128
$^2\Gamma_{+,7}$	25174.6	−0.0003754	−0.0018492	−0.0006176
$^2\Gamma_{+,8}$	27428.8	−0.0045815	−0.0000001	−0.0001709
$^2\Gamma_{+,9}$	28140.1	−0.0001686	0.0005518	0.0000103

[a]Using a SA-CASSCF(9,10) reference averaging over the first 10 doublet states.

Table S.23: Simulation parameters for HYSCORE spectra of $[(P_3{}^B)Fe(NNMe_2)]^{+/-}$

Charge	Nucleus	e^2qQ/h (MHz)	η	A_1 (MHz)	A_2 (MHz)	A_3 (MHz)	α_{HFC} (°)	β_{HFC} (°)	γ_{HFC} (°)	α_{NQI} (°)	β_{NQI} (°)	γ_{NQI} (°)
–	$^{14}N_\alpha$	−5.2	0.4	−3.9	−29.2	11.8	0	0	0	0	0	0
–	$^{15}N_\alpha$	–	–	5.4	41.0	−16.5	0	0	0	–	–	–
–	$^{14}N_\beta$	−4.0	0.4	1.6	−5.7	1.6	0	0	0	10	30	30
–	$^{15}N_\beta$	–	–	−2.2	8.0	−2.2	0	0	0	–	–	–
+	$^{14}N_\alpha$	−3.2	0.4	−10.7	−5.7	−0.1	0	20	0	0	0	0
+	$^{15}N_\alpha$	–	–	15.0	8.0	1	0	20	0	–	–	–
+	$^{14}N_\beta$	−2.8	0.4	−1.5	−7.3	−1.5	0	0	0	0	30	30
+	$^{15}N_\beta$	–	–	2.1	10.2	2.1	0	0	0	–	–	–

Table S.24: Experimental vibrational data of $[(P_3{}^B)Fe(NNMe_2)]^{+/0/-}$ versus QCC-NCA simulation results. All data are in units of cm^{-1}.

$(P_3{}^B)Fe(NNMe_2)$	Experimental		QCC-NCA	
	n.a.i.	^{15}N	n.a.i.	^{15}N
ν(Fe–N)	545	540	545	541
δ_{IP}(Fe–N–N)			572, 605	568, 600
δ_{OOP}(Fe–N–N)	448	442	448/455, 470, 504	444/453, 468, 501
ν_s(N–Me)	874	864	868	859
ν_s(N–N)	1337	1309	1354	1328
ν_{as}(N–Me)	1146	1132	1216	1195

$[(P_3{}^B)Fe(NNMe_2)]^-$	Experimental		QCC-NCA	
	n.a.i.	^{15}N	n.a.i.	^{15}N
ν(Fe–N)	346, 541	346, 530	341, 541	341, 533
δ_{IP}(Fe–N–N)	541	530	541	533
δ_{OOP}(Fe–N–N)	428	422	430, 468	424, 466
ν_s(N–Me)			970	963
ν_s(N–N)			1095, 1108, 1307	1081, 1099, 1284
ν_{as}(N–Me)			1188	1170

$[(P_3{}^B)Fe(NNMe_2)]^+$	Experimental		QCC-NCA	
	n.a.i.	^{15}N	n.a.i.	^{15}N
ν(Fe–N)	348, 495	348, 486	344, **493**, 588	344, **489**, 577
δ_{IP}(Fe–N–N)	588	579	493, **588**	489, **577**
δ_{OOP}(Fe–N–N)	495	486	446, 482, 488, 498	445, 475, 484, 497
ν_s(N–Me)			828	818
ν_s(N–N)	~1371, 1495	~1357, 1472	1155, 1388, 1519	1145, 1369, 1506
ν_{as}(N–Me)			973, 1194	965, 1176

Table S.25: Summary of key force constants from QCC-NCA. Stretching force constants are in units of mdyn $Å^{-1}$, and bending force constants are in units of mdyn Å

Force constant	$[(P_3{}^B)Fe(NNMe_2)]^+$	$(P_3{}^B)Fe(NNMe_2)$	$[(P_3{}^B)Fe(NNMe_2)]^-$
Fe–N	3.59	4.83	2.97
Fe–B	0.47	0.39	0.44
N–N	8.55	6.83	6.78
Fe–P1/P2/P3	1.27/1.05/1.18	1.46/1.22/1.89	1.03/1.49/1.31
$Fe–N–N_{IP}$	0.59	1.98	0.68

S.16 Coordinates of DFT-optimized Structures

Table S.26: Optimized coordinates for $(P_3{}^B)Fe(NNMe_2)$ ($S = 0$)

Atom	x (Å)	y (Å)	z (Å)
Fe	0.010810998	0.002966934	-0.001302714
N	-0.390510321	0.01898391	1.616401712
N	-0.827415331	0.030745215	2.843693045
C	-2.217758519	-0.274867715	3.194977816
H	-2.796318257	-0.344237735	2.276363525
H	-2.277763132	-1.227498025	3.737426271
H	-2.625876726	0.520787096	3.829905123
C	0.125689465	0.107068636	3.954449794
H	1.009317938	0.646884551	3.617606441
H	-0.340536458	0.644085961	4.787209705
H	0.419145748	-0.895186612	4.298737703
P	-0.698775353	2.086658112	-0.662662846
P	2.183726055	0.005201533	-0.53718875
P	-0.839837025	-1.981975676	-0.514319181
B	0.011910862	0.006228248	-2.498968646
C	1.355124973	0.808658815	-2.955421833
C	2.496134924	0.87872916	-2.114774737
C	2.608200731	2.105458591	-4.634959336
H	2.63764868	2.595859695	-5.610621927
C	3.731937145	2.145149235	-3.79560697
H	4.640892487	2.661477176	-4.110343221
C	-3.026528744	1.441475452	-4.611453717
H	-3.565292252	1.222216761	-5.536230437
C	1.443238002	1.444927836	-4.217360219
H	0.57186115	1.440904271	-4.876839362
C	-3.380196473	2.563095141	-3.84506715
H	-4.189858533	3.220951746	-4.166854058
C	3.677079762	1.525522836	-2.538273827
H	4.552095142	1.571415559	-1.891800966
C	-1.984991961	0.60001894	-4.190290509
H	-1.724658617	-0.269146707	-4.799174172
C	-0.0069553	-1.522218982	-3.032150923
C	-1.664815664	1.964298402	-2.221530293
C	0.521404793	3.502250432	-1.078255824

Atom	*x* (Å)	*y* (Å)	*z* (Å)
H	1.304418609	2.954672982	-1.618728776
C	-2.691956871	2.827622126	-2.650981748
H	-2.973662659	3.701651146	-2.060171146
C	0.369473573	-1.866191676	-4.352223211
H	0.747502689	-1.0892206	-5.020946587
C	0.305913819	-3.188257521	-4.81705624
H	0.618025174	-3.422703868	-5.837311806
C	-1.950136691	2.972820151	0.462019048
H	-2.128517115	3.940911542	-0.037547463
C	-1.28174303	0.840845908	-2.987761436
C	-0.454099498	-2.572607722	-2.196140624
C	-3.289801381	2.215308177	0.528651453
H	-3.989442669	2.751898567	1.189327955
H	-3.762867343	2.109029519	-0.454207519
H	-3.142321211	1.20759741	0.937677818
C	-0.523289211	-3.904299286	-2.656406285
H	-0.849039301	-4.709010782	-1.9943716
C	-0.141398661	-4.214360784	-3.96929229
H	-0.180008659	-5.246656585	-4.322209934
C	-0.02714879	4.577590603	-2.033945067
H	0.7659002	5.314552233	-2.239278922
H	-0.3483447	4.153379695	-2.991986982
H	-0.875548882	5.126478682	-1.595844536
C	-1.456243606	3.26228948	1.893391391
H	-1.223542164	2.331429326	2.422429689
H	-0.566741569	3.897775801	1.923113071
H	-2.25215694	3.780570842	2.452424581
C	-2.741351387	-2.082094356	-0.411941997
H	-2.955981137	-1.74082789	0.614004777
C	-3.410231778	-1.105619579	-1.388732151
H	-4.499049792	-1.097249294	-1.221189285
H	-3.029674204	-0.086703206	-1.269828936
H	-3.23067521	-1.406745059	-2.429827807
C	-3.345615767	-3.488081485	-0.599595203
H	-3.093901454	-3.895268907	-1.58945581
H	-3.02658587	-4.209142929	0.164440444
H	-4.443757449	-3.418425752	-0.54567529
C	1.183069536	4.182693628	0.136161206

Atom	*x* (Å)	*y* (Å)	*z* (Å)
H	0.522464742	4.941002012	0.580300085
H	1.469827881	3.474019591	0.923871163
H	2.094901945	4.704839076	-0.192722379
C	-0.434850634	-3.493401791	0.564263027
H	-0.953139092	-4.328918779	0.068424728
C	-0.980524849	-3.382561233	1.997575013
H	-0.465608508	-2.58020409	2.542558686
H	-2.060461698	-3.186517266	2.030267219
H	-0.79820139	-4.323985897	2.539620196
C	1.060204525	-3.833014068	0.605233763
H	1.216714438	-4.76662638	1.16889238
H	1.479899926	-3.971155839	-0.398277836
H	1.622338505	-3.036756795	1.11244379
C	2.946297917	0.938915657	0.944685194
H	2.063668974	1.510224431	1.267283347
C	4.082927436	1.953525635	0.720433282
H	5.026817999	1.477914292	0.42237746
H	3.820827456	2.700025576	-0.038706943
H	4.272775887	2.491514568	1.663658997
C	3.27787099	-0.041704333	2.088530631
H	3.427148005	0.516106776	3.027086344
H	2.462479936	-0.761049439	2.245953101
H	4.20089376	-0.605863958	1.899523893
C	3.371925712	-1.477324083	-0.725048179
H	3.177491653	-2.092810554	0.165059165
C	3.067234367	-2.312963001	-1.979754469
H	3.73729491	-3.187041849	-2.007879145
H	2.034808598	-2.670673676	-2.013477795
H	3.243316636	-1.724429239	-2.891186734
C	4.873921076	-1.123223938	-0.744501163
H	5.134867179	-0.555337442	-1.647718217
H	5.207088388	-0.555200472	0.13135129
H	5.456369246	-2.058286869	-0.77068719

Table S.27: Optimized coordinates for $(P_3{}^B)Fe(NNMe_2)$ ($S = 1$)

Atom	x (Å)	y (Å)	z (Å)
Fe	-0.12851598	0.062280363	-0.102780068
N	-0.234364418	0.169677327	1.655626079
N	-0.649450298	0.17454816	2.863959827
C	-2.023939068	-0.199651204	3.258588289
H	-2.522119616	-0.616452181	2.385732061
H	-1.991288604	-0.945423387	4.061912974
H	-2.569684518	0.681815297	3.61797156
C	0.217533277	0.591543768	3.983704175
H	1.1370962	0.993854975	3.564516919
H	-0.289225683	1.358804897	4.582435344
H	0.444818703	-0.264462999	4.632506783
P	-0.807626839	2.225927219	-0.749632016
P	2.283809981	-0.09921249	-0.457036762
P	-0.966868102	-2.052136895	-0.541967282
B	-0.018189098	0.015019443	-2.457683187
C	1.348898587	0.830494928	-2.838543717
C	2.497470084	0.871878518	-1.995188085
C	2.5951055	2.2204177	-4.459766538
H	2.618967008	2.748582858	-5.415800806
C	3.71518295	2.242735879	-3.615395786
H	4.617877241	2.785354117	-3.902908648
C	-3.072036159	1.299953194	-4.669639984
H	-3.589933436	1.02362838	-5.591102932
C	1.440602774	1.524498279	-4.072364252
H	0.572323957	1.535411435	-4.735846031
C	-3.485850021	2.430708979	-3.948271072
H	-4.325299395	3.035298083	-4.296798084
C	3.664892106	1.560812364	-2.390868693
H	4.540077441	1.582167683	-1.742912908
C	-2.002424039	0.517914379	-4.20712089
H	-1.705866039	-0.363975673	-4.779731744
C	-0.006326032	-1.515954165	-3.009773017
C	-1.74986475	1.975329975	-2.299481565
C	0.365271435	3.641060904	-1.212259702
H	0.875204425	3.203087736	-2.082402898
C	-2.817976557	2.769455319	-2.761595338

Atom	*x* (Å)	*y* (Å)	*z* (Å)
H	-3.154925208	3.639363142	-2.193247155
C	0.438593062	-1.836314143	-4.315633495
H	0.842136391	-1.043218323	-4.950062921
C	0.411059985	-3.149267622	-4.808333862
H	0.776939664	-3.361370156	-5.81564963
C	-2.081465535	3.053483849	0.368088359
H	-2.43733516	3.937737959	-0.185293202
C	-1.311262914	0.82919963	-3.012027475
C	-0.49254477	-2.589099217	-2.220301463
C	-3.283267093	2.119153065	0.592870252
H	-4.008200197	2.590988569	1.275123021
H	-3.800420675	1.89036015	-0.347477335
H	-2.958882461	1.169390495	1.038867111
C	-0.524618129	-3.912569473	-2.709296988
H	-0.87983365	-4.731049859	-2.079488433
C	-0.070216795	-4.195852881	-4.004667733
H	-0.080956608	-5.221510975	-4.378436205
C	-0.336178181	4.929589672	-1.675176414
H	0.416824039	5.630895532	-2.068128479
H	-1.060500321	4.739677687	-2.477643915
H	-0.853401872	5.438033287	-0.847250524
C	-1.490204531	3.537739145	1.70489452
H	-0.965458043	2.725649617	2.224915177
H	-0.781983896	4.363811147	1.567298571
H	-2.297446011	3.900904476	2.36070741
C	-2.861491663	-2.201188727	-0.494841955
H	-3.116199364	-1.878191998	0.529022442
C	-3.514659009	-1.217794688	-1.477542358
H	-4.608308669	-1.227281901	-1.346703228
H	-3.157198611	-0.19232524	-1.331137551
H	-3.294841457	-1.496649364	-2.516928787
C	-3.427892108	-3.616485699	-0.715371993
H	-3.154637176	-3.99830873	-1.709565051
H	-3.092161748	-4.340801686	0.038929788
H	-4.528068099	-3.581107337	-0.668902614
C	1.43873714	3.939043187	-0.152880352
H	1.03927259	4.510678756	0.696114811
H	1.879813328	3.015624669	0.23575477

Atom	*x* (Å)	*y* (Å)	*z* (Å)
H	2.244665221	4.537596003	-0.604008469
C	-0.517300153	-3.529974195	0.549710062
H	-0.993505368	-4.399701664	0.069643257
C	-1.075914972	-3.400974639	1.977172108
H	-0.618231787	-2.545346965	2.491693931
H	-2.166873943	-3.274727623	1.998327136
H	-0.836680711	-4.307747522	2.554810615
C	0.994713873	-3.786898109	0.595590479
H	1.20453828	-4.690043792	1.190481719
H	1.414403025	-3.936666786	-0.406535306
H	1.513944604	-2.941401339	1.067031807
C	3.05916538	0.757476873	1.053412226
H	2.197676352	1.356402265	1.389130893
C	4.261260956	1.711380625	0.919331765
H	5.180513096	1.199214296	0.607124097
H	4.064848222	2.522930874	0.208409214
H	4.46283948	2.174033469	1.899815629
C	3.29845033	-0.299347038	2.152933222
H	3.49363018	0.19895618	3.116129751
H	2.419273926	-0.947098592	2.278495446
H	4.167802413	-0.935020581	1.935284898
C	3.478389675	-1.560058991	-0.754897155
H	3.295841497	-2.22533142	0.102622021
C	3.123134694	-2.322988028	-2.041840503
H	3.774320318	-3.206675388	-2.135730642
H	2.082386554	-2.660205242	-2.059629438
H	3.281439526	-1.692058265	-2.927721121
C	4.982232671	-1.221758812	-0.781126625
H	5.225848449	-0.545048987	-1.61169451
H	5.342682389	-0.773011698	0.151981899
H	5.554597266	-2.150258135	-0.940892526

Table S.28: Optimized coordinates for $[(P_3{}^B)Fe(NNMe_2)]^-$

Atom	*x* (Å)	*y* (Å)	*z* (Å)
Fe	-0.005092376	-0.005895153	0.025536424
N	0.083855081	-0.114140551	1.775774862
N	-0.373142023	-0.089207148	2.995472732
C	-1.713276662	0.384299472	3.377686584
H	-2.215514035	0.718371382	2.472723548
H	-1.6446341	1.219588947	4.089735916
H	-2.291928839	-0.42412762	3.848039026
C	0.4833868	-0.456600265	4.127720757
H	1.300878283	-1.073051297	3.755843202
H	-0.099461882	-1.024473683	4.86673922
H	0.898721038	0.433418276	4.62925606
P	-0.964724703	1.961255376	-0.421813696
P	-1.108089586	-1.878977464	-0.499888163
P	2.23044693	0.027460233	-0.51381437
B	-0.016239277	0.014116215	-2.421812863
C	1.33891221	-0.733673884	-2.953037645
C	1.431303198	-1.352273392	-4.223876236
H	0.559788464	-1.342325183	-4.88430435
C	2.58789431	-2.028955796	-4.645727261
H	2.608949136	-2.515272438	-5.625313431
C	3.706208413	-2.104347336	-3.801725459
H	4.600545115	-2.651590123	-4.110675234
C	3.657862795	-1.478584326	-2.545025398
H	4.522225225	-1.553732653	-1.880723138
C	2.49327555	-0.803352831	-2.126742808
C	3.34153525	-0.922716921	0.702759318
H	4.32081521	-1.060392656	0.216144749
C	3.540823546	-0.097115466	1.988228263
H	2.563036562	0.184443274	2.401155092
H	4.112770187	0.824102496	1.810006966
H	4.085176957	-0.686602777	2.74638828
C	2.775845776	-2.312056739	1.028855523
H	3.427528091	-2.829156209	1.755237606
H	2.708858916	-2.937314474	0.129001126
H	1.768325357	-2.218015293	1.456948527
C	3.418547425	1.540488826	-0.756264207

Atom	*x* (Å)	*y* (Å)	*z* (Å)
H	3.247568568	2.151930974	0.143471527
C	3.02638388	2.372311727	-1.986767911
H	3.643638765	3.285854906	-2.036174202
H	1.973594994	2.66828402	-1.973933857
H	3.193983576	1.80119524	-2.911499808
C	4.92844236	1.237080971	-0.849793198
H	5.151941428	0.617720456	-1.730683234
H	5.33621221	0.734989981	0.03790327
H	5.481235928	2.185031533	-0.971972631
C	-1.330207307	-0.79011196	-2.963441651
C	-1.923639208	-0.572632607	-4.230968123
H	-1.52028292	0.207651919	-4.881744487
C	-3.042794728	-1.300861056	-4.666162973
H	-3.48435675	-1.090618756	-5.644626021
C	-3.605579	-2.286068942	-3.840417552
H	-4.48651728	-2.84652843	-4.16386517
C	-3.036468128	-2.52919843	-2.579877636
H	-3.493010197	-3.279104345	-1.929388682
C	-1.919426037	-1.786448235	-2.144456362
C	-0.285795656	-3.634058862	-0.570706099
H	0.268951565	-3.687694531	0.380215445
C	-1.228672014	-4.853700963	-0.655567761
H	-1.841872546	-4.814742422	-1.568182796
H	-1.898923957	-4.962323573	0.207421147
H	-0.622021863	-5.77408688	-0.71411777
C	0.721878157	-3.745118547	-1.723168406
H	1.241419956	-4.71762039	-1.675086056
H	1.473385982	-2.952152114	-1.697482627
H	0.211657583	-3.683499942	-2.695259377
C	-2.570171279	-2.410926379	0.60797145
H	-3.033332822	-3.275226123	0.106751886
C	-3.648452338	-1.324867313	0.711363956
H	-4.439137734	-1.630035713	1.41863355
H	-4.117249023	-1.139416771	-0.263646905
H	-3.220309231	-0.376474159	1.05895624
C	-2.08645233	-2.875875172	1.993838007
H	-1.499931874	-2.093233987	2.488417896
H	-1.450150613	-3.769442073	1.928250876

Atom	*x* (Å)	*y* (Å)	*z* (Å)
H	-2.946850906	-3.12697123	2.638100238
C	-0.066920651	1.557424952	-2.948375854
C	0.338406406	1.936898818	-4.252199385
H	0.750723617	1.177582079	-4.922437726
C	0.274579074	3.266645125	-4.697170022
H	0.616613943	3.523752354	-5.703843617
C	-0.209079535	4.270216344	-3.843218148
H	-0.246073248	5.311459223	-4.173756654
C	-0.626723491	3.924277894	-2.548267445
H	-0.979076291	4.71311643	-1.879343533
C	-0.553295507	2.587272303	-2.103771526
C	-2.879227261	2.21805345	-0.400118427
H	-3.189285471	1.731896609	0.540835341
C	-3.423213863	3.660511774	-0.394851021
H	-3.112757354	4.202258993	-1.30066347
H	-3.110246153	4.244883097	0.481230721
H	-4.527090212	3.636466984	-0.395252447
C	-3.519472363	1.450405281	-1.566793274
H	-4.61756898	1.43536347	-1.460596831
H	-3.160121606	0.417754591	-1.620835558
H	-3.277236453	1.932413327	-2.525200183
C	-0.508680999	3.485404188	0.640793275
H	-1.01289121	4.342167381	0.166476436
C	-1.007361204	3.376251462	2.089353201
H	-0.459355021	2.582221897	2.613108694
H	-2.081598034	3.154514362	2.158040616
H	-0.825816278	4.322258576	2.627942532
C	0.998070469	3.768404548	0.646805598
H	1.215569638	4.666983934	1.250229653
H	1.386168655	3.936966179	-0.36506098
H	1.539011983	2.919279207	1.087455804

Table S.29: Optimized coordinates for $[(P_3{}^B)Fe(NNMe_2)]^+$ ($S = 1/2$)

Atom	x (Å)	y (Å)	z (Å)
Fe	-0.006894038	0.013201438	0.019524574
N	-0.669030577	0.062572307	1.613636964
N	-1.531716342	0.095744476	2.542623167
C	-1.11311518	0.192737019	3.958530905
H	-0.025806948	0.228030086	3.989410912
H	-1.480678524	-0.679835104	4.508144558
H	-1.5367311	1.09865183	4.404901503
C	-2.992384449	0.029399015	2.310066187
H	-3.162056077	-0.165839669	1.253070575
H	-3.456263641	0.977492895	2.602240382
H	-3.41768142	-0.772525078	2.922484229
P	2.190409463	0.008566605	-0.638703931
P	-0.526443769	-2.266914039	-0.262805771
P	-0.343508745	2.259254249	-0.277150008
B	0.016338175	0.022800392	-2.293775753
C	2.330496753	-1.0851379	-2.088245118
C	1.146361345	-0.970382319	-2.856007962
C	1.080959514	-1.677838346	-4.076133369
H	0.179140094	-1.622234287	-4.690306542
C	2.152918017	-2.482067704	-4.498927812
H	2.080410635	-3.036800679	-5.436068918
C	3.317754744	-2.582171773	-3.719620008
H	4.147227357	-3.207766674	-4.052225548
C	3.417100859	-1.869898996	-2.513398976
H	4.334063964	-1.934910025	-1.924612594
C	3.305872752	-0.642863684	0.737115964
H	4.326406587	-0.381096231	0.416561652
C	3.108714135	1.591513607	-1.251326588
H	2.297900053	2.326911415	-1.344261234
C	3.007916448	0.048099007	2.082741702
H	1.987681023	-0.194566021	2.412294848
H	3.094997975	1.140021488	2.037861767
H	3.714711212	-0.310165477	2.845681179
C	3.229885923	-2.165688326	0.920816855
H	3.955420305	-2.475706684	1.687889657
H	3.45410004	-2.716855548	0.001008772

Atom	*x* (Å)	*y* (Å)	*z* (Å)
H	2.232144197	-2.461320653	1.269005869
C	4.185231341	2.170341823	-0.309944125
H	5.048706063	1.498242651	-0.209752733
H	3.819124853	2.405648432	0.696565491
H	4.558458483	3.108318031	-0.746665776
C	3.718963955	1.425715025	-2.658451168
H	4.124129442	2.398259702	-2.976141288
H	2.980167949	1.109005581	-3.402062907
H	4.545231697	0.70145845	-2.662185502
C	-1.491336339	-0.503986352	-2.144416865
C	-1.885592095	-1.559593511	-1.257980452
C	-3.242375374	-1.945152354	-1.159305106
H	-3.54714723	-2.719932966	-0.457587984
C	-4.21334731	-1.361517652	-1.981136644
H	-5.251592421	-1.690146471	-1.914151683
C	-3.838306715	-0.36952461	-2.903672775
H	-4.584291457	0.069100729	-3.568486444
C	-2.512468445	0.069189912	-2.952716477
H	-2.243915272	0.867799938	-3.645739828
C	-1.329504782	-3.058840506	1.246462597
H	-2.066699725	-2.289860248	1.521073149
C	0.215339955	-3.675888977	-1.29477314
H	0.935808436	-3.151861985	-1.931494359
C	1.006256026	-4.728330418	-0.491324841
H	0.356241592	-5.390368214	0.093390961
H	1.743215948	-4.282319561	0.184774298
H	1.556374522	-5.361092012	-1.203230338
C	-0.820514653	-4.339034968	-2.22484654
H	-0.30220217	-5.074699337	-2.858260582
H	-1.302867077	-3.608347341	-2.885559576
H	-1.603193525	-4.873141233	-1.670190822
C	-0.32543544	-3.182838254	2.413175617
H	-0.860548258	-3.45298779	3.336373721
H	0.214997423	-2.243572552	2.587191976
H	0.413356381	-3.973016479	2.225057008
C	-2.095197587	-4.389552754	1.06778123
H	-1.415095735	-5.234597929	0.910198986
H	-2.810122502	-4.378559314	0.237536885

Atom	*x* (Å)	*y* (Å)	*z* (Å)
H	-2.659623303	-4.597231415	1.989657396
C	0.105696211	1.525732731	-2.871215516
C	-0.130313379	2.657753827	-2.044934689
C	-0.178955048	3.960101256	-2.591760255
H	-0.355243895	4.825912392	-1.955602065
C	0.02082878	4.157777774	-3.964242007
H	-0.014195359	5.165686965	-4.379888853
C	0.282641144	3.055239651	-4.792130282
H	0.452322539	3.20305375	-5.860049815
C	0.328881196	1.763927924	-4.247566854
H	0.537338375	0.919082439	-4.90749431
C	0.883854618	3.253694821	0.769794479
H	1.75214632	2.58146586	0.764376586
C	-2.028315545	2.914300723	0.246960942
H	-2.075913888	2.618739515	1.30761449
C	0.425289795	3.349144606	2.238660165
H	1.25660509	3.72597968	2.852566546
H	0.139053848	2.366264025	2.633174181
H	-0.417378059	4.04097829	2.369602002
C	1.363273853	4.615775087	0.23307483
H	0.567811749	5.372301368	0.231681432
H	1.766456915	4.541242433	-0.784611769
H	2.167594029	4.989362722	0.884868319
C	-3.164465147	2.211488102	-0.512646706
H	-4.134377476	2.491900127	-0.074768641
H	-3.073333307	1.119326903	-0.48797935
H	-3.172844924	2.518160696	-1.567038353
C	-2.223101004	4.442523961	0.170226298
H	-2.24597719	4.788629471	-0.871212216
H	-1.453903352	5.006945673	0.709774221
H	-3.195362537	4.699120025	0.617724647

Table S.30: Optimized coordinates for $[(P_3{}^B)Fe(NNMe_2)]^+$ ($S = 3/2$)

Atom	x (Å)	y (Å)	z (Å)
Fe	0.114729567	-0.048266611	0.097517887
N	0.000694085	-0.072180277	1.88515728
N	-0.471935433	0.006753745	3.048818202
C	0.351565176	-0.266512096	4.252986706
H	1.34071064	-0.574455418	3.921696725
H	-0.11873068	-1.059582676	4.843360763
H	0.417875391	0.640288596	4.863506592
C	-1.896105804	0.319771437	3.328442484
H	-2.385041734	0.529542117	2.379455267
H	-1.961152167	1.183854626	3.997709105
H	-2.364981867	-0.540467597	3.81778223
P	2.495497634	0.110013869	-0.568719549
P	-0.949538334	-2.206104715	-0.37295833
P	-0.676410487	2.205675051	-0.320040002
B	0.015729349	0.093060295	-2.295365406
C	2.405947465	-0.994800215	-2.022031679
C	1.174637861	-0.9238431	-2.725712688
C	1.03463273	-1.7248628	-3.885820405
H	0.096638197	-1.693580081	-4.444595007
C	2.070395755	-2.560860139	-4.327799732
H	1.937854369	-3.165311084	-5.226781447
C	3.276228494	-2.627184219	-3.609813533
H	4.081772184	-3.281954333	-3.945040109
C	3.444525633	-1.841729007	-2.460664602
H	4.390004121	-1.889940028	-1.917586922
C	3.721674332	-0.679138749	0.618324826
H	4.708284767	-0.662649388	0.125573818
C	3.351230512	1.654355841	-1.272887466
H	2.503347879	2.195102606	-1.720666838
C	3.809537325	0.093071888	1.952406933
H	2.807133094	0.212589388	2.387498547
H	4.260252144	1.084541328	1.850836173
H	4.4246252	-0.478835205	2.663194754
C	3.322351653	-2.138335658	0.910048453
H	4.061140197	-2.594252177	1.58593616
H	3.265137613	-2.753511433	0.004743408

Atom	*x* (Å)	*y* (Å)	*z* (Å)
H	2.343061856	-2.168225225	1.410037055
C	4.017752726	2.572853514	-0.229828863
H	4.960686713	2.143483007	0.135811855
H	3.379257509	2.787824895	0.636473818
H	4.262464814	3.532734785	-0.707643439
C	4.353082702	1.337236967	-2.400227406
H	4.782052705	2.280605964	-2.770703617
H	3.879177437	0.827416275	-3.246565907
H	5.187370491	0.715212488	-2.042932386
C	-1.505070979	-0.433974683	-2.413530919
C	-2.059467683	-1.512169601	-1.654615735
C	-3.382397323	-1.941831268	-1.883008966
H	-3.810609121	-2.749745811	-1.295375098
C	-4.17707404	-1.342179071	-2.869605081
H	-5.197554128	-1.691632454	-3.032203343
C	-3.646876572	-0.299091747	-3.640876638
H	-4.249560019	0.169584383	-4.420695641
C	-2.342072956	0.150625167	-3.400007202
H	-1.951988052	0.973905411	-3.999775853
C	-2.002878641	-2.905350233	1.028212984
H	-2.666623452	-2.05180043	1.246271904
C	-0.048534243	-3.655303366	-1.18449138
H	0.753083078	-3.147218419	-1.735490044
C	0.616618493	-4.615826952	-0.179444233
H	-0.116288918	-5.259072429	0.324961748
H	1.201090871	-4.089729183	0.584815704
H	1.304711262	-5.275661626	-0.727880634
C	-0.909880045	-4.414977952	-2.211264582
H	-0.284148502	-5.173398249	-2.705575363
H	-1.304084742	-3.747295443	-2.987013874
H	-1.755507084	-4.936248232	-1.743013054
C	-1.131715405	-3.17776053	2.27986635
H	-1.760877192	-3.146634625	3.182034779
H	-0.318120252	-2.452535862	2.391125519
H	-0.684540929	-4.178235273	2.235072095
C	-2.880541178	-4.151641459	0.771847046
H	-2.266964171	-5.035668573	0.557384601
H	-3.60129914	-4.034752214	-0.04313331

Atom	*x* (Å)	*y* (Å)	*z* (Å)
H	-3.454775857	-4.368807299	1.685407083
C	0.171628378	1.599037002	-2.81793406
C	-0.343687821	2.678001028	-2.052742201
C	-0.454559277	3.970616408	-2.608846557
H	-0.855548906	4.79871239	-2.026931928
C	-0.014962337	4.21271088	-3.918492985
H	-0.095672516	5.214902954	-4.341614756
C	0.552808664	3.170022677	-4.667240208
H	0.9165645	3.361248439	-5.67834312
C	0.641740902	1.880521934	-4.121571393
H	1.061063343	1.071677733	-4.723984445
C	0.454552274	3.287531122	0.759881659
H	1.335834197	2.634206231	0.853050822
C	-2.423299931	2.698824686	0.165368514
H	-2.389623844	2.617508833	1.263491028
C	-0.110540801	3.494250702	2.178746722
H	0.675474563	3.916832528	2.822009497
H	-0.443917125	2.555057491	2.634679637
H	-0.951403356	4.201641306	2.183325964
C	0.931637851	4.628712543	0.173170161
H	0.11113981	5.353157566	0.078346886
H	1.403425835	4.513080285	-0.809274026
H	1.675835505	5.067379687	0.855380671
C	-3.463181353	1.68891217	-0.351610007
H	-4.451346707	1.93144608	0.067281935
H	-3.212042068	0.657224702	-0.070127547
H	-3.543664921	1.721383583	-1.445613814
C	-2.835711388	4.139650598	-0.19266897
H	-2.947149046	4.260313836	-1.278325993
H	-2.121870264	4.890507873	0.170846478
H	-3.811779296	4.361056792	0.264970372

Table S.31: Optimized coordinates for $[(P_3{}^B)Fe(NNMe_2)]^+$ ($S = 5/2$)

Atom	x (Å)	y (Å)	z (Å)
Fe	0.267596611	0.060055928	0.106699207
N	0.409586857	-0.241222443	1.918569354
N	0.2800223	0.380567154	3.090200181
C	1.486095262	0.55320657	3.913597815
H	2.249607896	1.061357353	3.323007175
H	1.877281395	-0.414199831	4.260350832
H	1.232425754	1.168765304	4.780397525
C	-0.952628588	0.130803938	3.857810382
H	-1.79537242	0.110028173	3.165357428
H	-1.088985985	0.935397548	4.586015028
H	-0.903563697	-0.827743534	4.392796151
P	2.633757263	-0.085262116	-0.665495207
P	-1.045322408	-2.070617368	-0.448118657
P	-0.9394094	2.192134685	-0.16838588
B	0.014174732	0.054915433	-2.340244367
C	2.417945015	-1.082268306	-2.186101971
C	1.152443891	-0.95751715	-2.827642467
C	0.931999366	-1.741585317	-3.987142245
H	-0.031645018	-1.673955722	-4.49573225
C	1.916673014	-2.597497013	-4.501615666
H	1.715524161	-3.181747246	-5.401043831
C	3.154473279	-2.710254779	-3.851841084
H	3.92232931	-3.383062201	-4.2360101
C	3.400087255	-1.956383195	-2.694521037
H	4.361470249	-2.067712651	-2.19107367
C	3.885180183	-1.04673712	0.343501353
H	4.711247899	-1.260409943	-0.35364899
C	3.522593106	1.455219451	-1.284109669
H	2.870135827	1.752534166	-2.118669623
C	4.467541804	-0.259316067	1.530001704
H	3.677545976	0.070898271	2.214989303
H	5.043402885	0.617425271	1.210929248
H	5.148087421	-0.912240004	2.096080139
C	3.274023988	-2.379976394	0.808625245
H	4.031203066	-2.967509506	1.348735497
H	2.921229895	-2.983179546	-0.03740398

Atom	*x* (Å)	*y* (Å)	*z* (Å)
H	2.428607103	-2.198979118	1.487484534
C	3.533592018	2.614785432	-0.271240454
H	4.204612327	2.425097198	0.576179071
H	2.53057234	2.812123938	0.125584561
H	3.883331299	3.530511032	-0.770059792
C	4.924013301	1.167273889	-1.853434327
H	5.311110536	2.076451124	-2.337349225
H	4.904686713	0.372972277	-2.611240285
H	5.639311231	0.885574061	-1.067891032
C	-1.479721184	-0.439671719	-2.600695804
C	-2.047434042	-1.531598067	-1.889174405
C	-3.273001356	-2.088543412	-2.309347195
H	-3.693051294	-2.954575664	-1.804195249
C	-3.970437361	-1.546022192	-3.398968476
H	-4.920615484	-1.984876986	-3.706386099
C	-3.441710094	-0.44338201	-4.085082672
H	-3.981814986	-0.012239938	-4.929708642
C	-2.208944919	0.095816869	-3.690057466
H	-1.794416993	0.939884915	-4.244843724
C	-2.222430717	-2.491786706	0.970223978
H	-2.668886949	-1.501200417	1.161397922
C	-0.165740756	-3.644073156	-1.034690601
H	0.711477424	-3.220268364	-1.546520503
C	0.341451343	-4.554731552	0.100406458
H	-0.478918201	-5.12774313	0.552664703
H	0.858317662	-4.003833668	0.894509898
H	1.051585325	-5.281515394	-0.321095429
C	-0.951242781	-4.465164724	-2.07567659
H	-0.316770588	-5.29581942	-2.420387269
H	-1.227150335	-3.867776394	-2.952361434
H	-1.865916316	-4.902698862	-1.651894586
C	-1.44591408	-2.903536137	2.243055125
H	-2.086567344	-2.732300953	3.120520618
H	-0.522167206	-2.324747148	2.36867863
H	-1.196774038	-3.970773223	2.229640328
C	-3.372766187	-3.49377359	0.732347362
H	-3.00815784	-4.459398834	0.356802252
H	-4.136796696	-3.112406066	0.047377193

Atom	*x* (Å)	*y* (Å)	*z* (Å)
H	-3.871143459	-3.686938953	1.694634089
C	0.241284345	1.621162781	-2.592055936
C	-0.38059699	2.664270806	-1.842559883
C	-0.440765922	3.976923469	-2.35850867
H	-0.935425275	4.768599196	-1.799170825
C	0.149224319	4.288998471	-3.59134605
H	0.092482203	5.306942027	-3.97888548
C	0.830430424	3.29233402	-4.306137097
H	1.311625647	3.531376532	-5.255978199
C	0.877132441	1.98264564	-3.808200737
H	1.38024182	1.208500463	-4.391081552
C	-0.110463211	3.355353651	1.092227662
H	0.786871415	2.775409013	1.36069866
C	-2.780690611	2.497362523	0.041185327
H	-2.90226873	2.433541445	1.133561131
C	-0.953780008	3.497430773	2.375410458
H	-0.333249843	3.953862327	3.160383699
H	-1.308771183	2.532169417	2.753775615
H	-1.820554773	4.154451085	2.219675153
C	0.360535687	4.738735926	0.606733214
H	-0.483007792	5.403010025	0.37390791
H	1.009749555	4.680827073	-0.274517904
H	0.935077941	5.21445133	1.415975204
C	-3.644343385	1.391923363	-0.588474433
H	-4.699141165	1.57062126	-0.33227461
H	-3.368341767	0.396915597	-0.218834758
H	-3.558457521	1.380014353	-1.682157503
C	-3.245293198	3.892297817	-0.420523304
H	-3.18218878	3.98842964	-1.512778388
H	-2.66833847	4.707193363	0.036415064
H	-4.29895097	4.032328363	-0.1363712

Table S.32: Optimized coordinates for $[H_2NNMe_2]^{\bullet+}$

Atom	*x* (Å)	*y* (Å)	*z* (Å)
N	0.002140723	-0.227830199	0.068113865
N	0.001255257	0.139868521	1.353763862
C	-1.274259026	0.083415953	2.075053543
H	-1.462422508	-0.942081808	2.416163825
H	-2.078770527	0.411157557	1.413273764
H	-1.20370385	0.752161243	2.933219314
C	1.277456616	0.091216667	2.074411659
H	1.201901194	0.756597595	2.934738459
H	2.079061665	0.427546152	1.413382178
H	1.473928561	-0.933843025	2.412133791
H	-0.868056817	-0.092218029	-0.441172901
H	0.871308711	-0.086850626	-0.441481358

Table S.33: Optimized coordinates for $[HNNMe_2]^{\bullet}$

Atom	*x* (Å)	*y* (Å)	*z* (Å)
N	0.068782452	-0.289434885	0.032028036
N	-0.006298886	0.18902767	1.294845964
C	-1.246197817	0.093800222	2.061525663
H	-1.433319396	-0.93615032	2.407575967
H	-2.078731832	0.411416876	1.427068612
H	-1.192026334	0.753937479	2.932706126
C	1.234747225	0.072717512	2.049685149
H	1.239508164	0.806420848	2.861514276
H	2.061388675	0.267721864	1.365762434
H	1.355180254	-0.935580547	2.477229908
H	-0.901957291	-0.303642103	-0.312817025

Table S.34: Optimized coordinates for $[NNMe_2]^{\bullet-}$ (equilibrium geometry)

Atom	x (Å)	y (Å)	z (Å)
N	0.002653537	0.563092209	0.072917181
N	0.000902085	-0.138168564	1.207758404
C	-1.217959239	-0.07307122	2.051595921
H	-1.214157112	-0.825703569	2.864950203
H	-2.068880836	-0.24401924	1.387367116
H	-1.344574277	0.934766521	2.515460065
C	1.217729397	-0.07423346	2.054642084
H	1.34413564	0.933484521	2.518817054
H	2.070123188	-0.245977259	1.392510179
H	1.211192449	-0.826868451	2.8679725

Table S.35: Optimized coordinates for $[NNMe_2]^{\bullet-}$ (C_{2v} geometry)

Atom	x (Å)	y (Å)	z (Å)
N	0.081217201	-0.524737396	-0.045950265
N	0.01699979	-0.181008715	1.254269798
C	-1.234497399	-0.062367517	1.990770474
H	-1.301349884	-0.75221979	2.868247591
H	-2.029924566	-0.304376221	1.283294227
H	-1.411757706	0.964826107	2.398404961
C	1.189871946	0.137082484	2.05796805
H	1.169114353	1.173116053	2.480754686
H	2.051039081	0.041156944	1.393852181
H	1.326397185	-0.544781949	2.933718297

References

(1) Gütlich, P.; Bill, E.; Trautwein, A. X., *Mössbauer Spectroscopy and Transition Metal Chemistry: Fundamentals and Applications*; Springer: New York, 2011.

(2) Prisecaru, I. "WMOSS4 Mössbauer Spectral Analysis Software", www.wmoss.org, 2009–2016.

(3) Hyde, J. S.; Pasenkiewicz-Gierula, M.; Jesmanowicz, A.; Antholine, W. E. Pseudo field modulation in EPR spectroscopy. *Appl. Magn. Reson.* **1990**, *1*, 483.

(4) Oyala, P. H.; Stich, T. A.; Britt, R. D. Metal ion oxidation state assignment based on coordinating ligand hyperfine interaction. *Photosynth. Res.* **2015**, *124*, 7–18.

(5) Thompson, N. B.; Green, M. T.; Peters, J. C. Nitrogen Fixation via a Terminal Fe(IV) Nitride. *J. Am. Chem. Soc.* **2017**, *139*, 15312–15315.

(6) Neese, F. The ORCA program system. *WIRES Comput. Mol. Sci.* **2011**, *2*, 73–78.

(7) Matson, B. D.; Peters, J. C. Fe-Mediated HER vs N_2RR: Exploring Factors That Contribute to Selectivity in $P_3{}^{E}Fe(N_2)$ (E = B, Si, C) Catalyst Model Systems. *ACS Catal.* **2018**, *8*, 1448–1455.

(8) Tao, J.; Perdew, J. P.; Staroverov, V. N.; Scuseria, G. E. Climbing the Density Functional Ladder: Nonempirical Meta-Generalized Gradient Approximation Designed for Molecules and Solids. *Phys. Rev. Lett.* **2003**, *91*, 146401.

(9) Staroverov, V. N.; Scuseria, G. E.; Tao, J.; Perdew, J. P. Comparative assessment of a new nonempirical density functional: Molecules and hydrogen-bonded complexes. *J. Chem. Phys.* **2003**, *119*, 12129–12137.

(10) Grimme, S. Accurate Calculation of the Heats of Formation for Large Main Group Compounds with Spin-Component Scaled MP2 Methods. *J. Phys. Chem. A* **2005**, *109*, 3067–3077.

(11) Quintal, M. M.; Karton, A.; Iron, M. A.; Boese, A. D.; Martin, J. M. L. Benchmark Study of DFT Functionals for Late-Transition-Metal Reactions. *J. Phys. Chem. A* **2006**, *110*, 709–716.

(12) Van Wüllen, C. Molecular density functional calculations in the regular relativistic approximation: Method, application to coinage metal diatomics, hydrides, fluorides and chlorides, and comparison with first-order relativistic calculations. *J. Chem. Phys.* **1998**, *109*, 392–399.

(13) Pantazis, D. A.; Chen, X.-Y.; Landis, C. R.; Neese, F. All-Electron Scalar Relativistic Basis Sets for Third-Row Transition Metal Atoms. *J. Chem. Theory Comput.* **2008**, *4*, 908–919.

(14) Weigend, F. Accurate Coulomb-fitting basis sets for H to Rn. *Phys. Chem. Chem. Phys.* **2006**, *8*, 1057–1065.

(15) Neese, F.; Wennmohs, F.; Hansen, A.; Becker, U. Efficient, approximate and parallel Hartree–Fock and hybrid DFT calculations. A 'chain-of-spheres' algorithm for the Hartree–Fock exchange. *Chem. Phys.* **2009**, *356*, 98–109.

(16) Neese, F. Definition of corresponding orbitals and the diradical character in broken symmetry DFT calculations on spin coupled systems. *J. Phys. Chem. Solids.* **2004**, *65*, 781–785.

(17) Ye, S.; Geng, C.-Y.; Shaik, S.; Neese, F. Electronic structure analysis of multistate reactivity in transition metal catalyzed reactions: the case of C-H bond activation by non-heme iron(iv)-oxo cores. *Phys. Chem. Chem. Phys.* **2013**, *15*, 8017–8030.

(18) Weigend, F.; Ahlrichs, R. Balanced basis sets of split valence, triple zeta valence and quadruple zeta valence quality for H to Rn: Design and assessment of accuracy. *Phys. Chem. Chem. Phys.* **2005**, *7*, 3297–3305.

(19) Neese, F. Prediction and interpretation of the ^{57}Fe isomer shift in Mössbauer spectra by density functional theory. *Inorg. Chim. Acta* **2002**, *337*, 181–192.

(20) Huzinaga, S. Gaussian-Type Functions for Polyatomic Systems. I. *J. Chem. Phys.* **1965**, *42*, 1293–1302.

(21) Stoychev, G. L.; Auer, A. A.; Neese, F. Automatic Generation of Auxiliary Basis Sets. *J. Chem. Theory Comput.* **2017**, *13*, 554–562.

(22) Neese, F. Efficient and accurate approximations to the molecular spin-orbit coupling operator and their use in molecular g-tensor calculations. *J. Chem. Phys.* **2005**, *122*, 034107.

(23) Neese, F. Prediction of electron paramagnetic resonance g values using coupled perturbed Hartree–Fock and Kohn–Sham theory. *J. Chem. Phys.* **2001**, *115*, 11080–11096.

(24) Neese, F. Metal and ligand hyperfine couplings in transition metal complexes: The effect of spin–orbit coupling as studied by coupled perturbed Kohn–Sham theory. *J. Chem. Phys.* **2003**, *118*, 3939–3948.

(25) Smith, P.; Stevens, R. D.; Kaba, R. A. Electron paramagnetic resonance spectroscopic study of radical cations from hydrazine, methylhydrazine, and dimethylhydrazines. *J. Phys. Chem.* **1971**, *75*, 2048–2055.

(26) Malatesta, V.; Ingold, K. U. Electron paramagnetic resonance spectra of 1,1-dialkylhydrazyl radicals in solution. *J. Am. Chem. Soc.* **1973**, *95*, 6110–6113.

(27) Hermosilla, L.; Calle, P.; García de la Vega, J. M.; Sieiro, C. Density Functional Theory Study of ^{14}N Isotropic Hyperfine Coupling Constants of Organic Radicals. *J. Phys. Chem. A* **2006**, *110*, 13600–13608.

(28) De Jong, W. A.; Harrison, R. J.; Dixon, D. A. Parallel Douglas–Kroll energy and gradients in NWChem: Estimating scalar relativistic effects using Douglas–Kroll contracted basis sets. *J. Chem. Phys.* **2001**, *114*, 48–53.

(29) Balabanov, N. B.; Peterson, K. A. Systematically convergent basis sets for transition metals. I. All-electron correlation consistent basis sets for the 3d elements Sc–Zn. *J. Chem. Phys.* **2005**, *123*, 064107.

(30) Reiher, M. Relativistic Douglas–Kroll–Hess theory. *WIRES Comput. Mol. Sci.* **2012**, *2*, 139–149.

(31) Furche, F.; Ahlrichs, R.; Hättig, C.; Klopper, W.; Sierka, M.; Weigend, F. Turbomole. *WIRES Comput. Mol. Sci.* **2014**, *4*, 91–100.

(32) Neese, F. Importance of Direct Spin–Spin Coupling and Spin-Flip Excitations for the Zero-Field Splittings of Transition Metal Complexes: A Case Study. *J. Am. Chem. Soc.* **2006**, *128*, 10213–10222.

(33) Becke, A. D. Density-functional exchange-energy approximation with correct asymptotic behavior. *Phys. Rev. A* **1988**, *38*, 3098–3100.

(34) Perdew, J. P. Density-functional approximation for the correlation energy of the inhomogeneous electron gas. *Phys. Rev. B* **1986**, *33*, 8822–8824.

(35) Pierloot, K. The CASPT2 method in inorganic electronic spectroscopy: from ionic transition metal to covalent actinide complexes. *Mol. Phys.* **2003**, *101*, 2083–2094.

(36) Angeli, C.; Cimiraglia, R.; Evangelisti, S.; Leininger, T.; Malrieu, J. P. Introduction of n-electron valence states for multireference perturbation theory. *J. Chem. Phys.* **2001**, *114*, 10252–10264.

(37) Angeli, C.; Cimiraglia, R.; Malrieu, J.-P. N-electron valence state perturbation theory: a fast implementation of the strongly contracted variant. *Chem. Phys. Lett.* **2001**, *350*, 297–305.

(38) Neese, F. Sum-over-states based multireference ab initio calculation of EPR spin Hamiltonian parameters for transition metal complexes. A case study. *Magn. Reson. Chem.* **2004**, *42*, S187–S198.

(39) Foster, J. M.; Boys, S. F. Canonical Configurational Interaction Procedure. *Rev. Mod. Phys.* **1960**, *32*, 300–302.

(40) Frisch, M. J.; Trucks, G. W.; Schlegel, H. B.; Scuseria, G. E.; Robb, M. A.; Cheeseman, J. R.; Scalmani, G.; Barone, V.; Mennucci, B.; Petersson, G. A.; Nakatsuji, H.; Caricato, M.; Li, X.; Hratchian, H. P.; Izmaylov, A. F.; Bloino, J.; Zheng, G.; Sonnenberg, J. L.; Hada, M.; Ehara, M.; Toyota, K.; Fukuda, R.; Hasegawa, J.; Ishida, M.; Nakajima, T.; Honda, Y.; Kitao, O.; Nakai, H.; Vreven, T.; Montgomery, J. A.; Peralta, J. E.; Ogliaro, F.; Bearpark, M.; Heyd, J. J.; Brothers, E.; Kudin, K. N.; Staroverov, V. N.; Kobayashi, R.; Normand, J.; Raghavachari, K.; Rendell, A.; Burant, J. C.; Iyengar, S. S.; Tomasi, J.; Cossi, M.; Rega, N.; Millam, J. M.; Klene, M.; Knox, J. E.; Cross, J. B.; Bakken, V.; Adamo, C.; Jaramillo, J.; Gomperts, R.; Stratmann, R. E.; Yazyev, O.; Austin, A. J.; Cammi, R.; Pomelli, C.; Ochterski, J. W.; Martin, R. L.; Morokuma, K.; Zakrzewski, V. G.; Voth, G. A.; Salvador, P.; Dannenberg, J. J.; Dapprich, S.; Daniels, A. D.; Farkas; Foresman, J. B.; Ortiz, J. V.; Cioslowski, J.; Fox, D. J. Gaussian 09, Revision B.01, Gaussian Inc., Wallingford CT, 2009.

(41) Allouche, A.; Pourcin, J. Ab initio calculation of vibrational force fields: Determination of non-redundant symmetry coordinates by least-square component analysis. *Spectrochim. Acta A* **1993**, *49*, 571–580.

(42) Paulat, F.; Berto, T. C.; DeBeer George, S.; Goodrich, L.; Praneeth, V. K. K.; Sulok, C. D.; Lehnert, N. Vibrational Assignments of Six-Coordinate Ferrous Heme Nitrosyls: New Insight from Nuclear Resonance Vibrational Spectroscopy. *Inorg. Chem.* **2008**, *47*, 11449–11451.

(43) McIntosh, D. F.; Peterson, M. R. QCPE 576 University of Indiana, Bloomington, Indiana.

(44) Spek, A. Structure validation in chemical crystallography. *Acta Crystallogr. D* **2009**, *65*, 148–155.

(45) La Mar, G. N.; Horrocks, W. D.; Holm, R. H., *NMR of Paramagnetic Molecules: Principles and Applications*; Academic Press: New York, 1973.

(46) Kaupp, M.; Bühl, M.; Malkin, V. G., *Calculation of NMR and EPR Parameters: Theory and Applications*; Wiley-VCH: Weinheim, 2004.

(47) Lemon Christopher, M.; Huynh, M.; Maher Andrew, G.; Anderson Bryce, L.; Bloch Eric, D.; Powers David, C.; Nocera Daniel, G. Electronic Structure of Copper Corroles. *Angew. Chem. Int. Ed.* **2016**, *55*, 2176–2180.

(48) Carvajal, C.; Tölle, K. J.; Smid, J.; Szwarc, M. Studies of Solvation Phenomena of Ions and Ion Pairs in Dimethoxyethane and Tetrahydrofuran. *J. Am. Chem. Soc.* **1965**, *87*, 5548–5553.

(49) Gütlich, P.; Gaspar, A. B.; Garcia, Y. Spin state switching in iron coordination compounds. *Beilstein J. Org. Chem.* **2013**, *9*, 342–391.

(50) Harris, D. C.; Bertolucci, M. D., *Symmetry and Spectroscopy: An Introduction to Vibrational and Electronic Spectroscopy*; Dover Publications: New York, 1989.

(51) De Lorenzi, L.; Fermeglia, M.; Torriano, G. Density and Viscosity of 1-Methoxy-2-Propanol, 2-Methyltetrahydrofuran, α,α,α-Trifluorotoluene, and Their Binary Mixtures with 1,1,1-Trichloroethane at Different Temperatures. *J. Chem. Eng. Data* **1996**, *41*, 1121–1125.

(52) Del Castillo, T. J.; Thompson, N. B.; Peters, J. C. A Synthetic Single-Site Fe Nitrogenase: High Turnover, Freeze-Quench ^{57}Fe Mössbauer Data, and a Hydride Resting State. *J. Am. Chem. Soc.* **2016**, *138*, 5341–5350.

(53) Rittle, J.; Peters, J. C. An Fe-N_2 Complex That Generates Hydrazine and Ammonia via Fe=NNH_2: Demonstrating a Hybrid Distal-to-Alternating Pathway for N_2 Reduction. *J. Am. Chem. Soc.* **2016**, *138*, 4243–4248.